TAMPERE UNIVERSITY OF TECHNOLOGY

EVELIINA KOSKI

RADIATION EFFICIENCY MEASUREMENT METHOD OF BALANCED PASSIVE UHF RFID DIPOLE TAG ANTENNAS

Master of Science Thesis

Examiners: Adjunct Professor Leena Ukkonen and Professor Lauri Sydänheimo
Examiners and topic approved by the Faculty Council of the Faculty of Computing and Electrical Engineering on 6 June 2012.

ABSTARCT

TAMPERE UNIVERSITY OF TECHNOLOGY
Master's Degree Programme in Electrical Engineering
KOSKI, EVELIINA: Radiation efficiency measurement method of balanced passive UHF RFID dipole tag antennas
Master of Science Thesis, 89 pages
November 2012
Major: RF Engineering
Examiners: Adjunct Professor Leena Ukkonen and Professor Lauri Sydänheimo
Keywords: Directivity approximation, power transmission coefficient, radiation efficiency, realised gain, sewed antenna, *S*-parameter method, UHF RFID

Radio frequency identification (RFID) is a quickly developing technology for wireless identification of objects. In an RFID system, objects to be identified are equipped with a tag consisting of an antenna and an application specific integrated circuit (ASIC). The electronic product code (EPC) is located in the memory of the ASIC, which is sensed by the RFID reader. The tag plays a key role in determining the quality of the passive UHF RFID system. To assure long range performance, the tag is optimised to operate in a specific application environment. More recently, much attention is paid to application areas within biomedical engineering, in which wearable tags for on-body use could provide real-time remote bio-monitoring of humans. Concurrently with the continuously developing RFID, new type of antenna materials and antenna structures are emerging and studied to fulfil the requirements encountered in the new RFID application areas. Pioneering tag designs where the tag antenna structure is formed using conductive ink or conductive threads have been proposed as competitive materials to conventional etched copper. The conductive ink can directly be printed on various flexible substrates or directly on the object that is to be identified. Conductive thread can be sewed seamlessly on garments worn by humans. The sewed antennas are almost tailor-made for wearable applications.

The new materials used to form the complex antenna conductive patterns or substrates are challenging to model accurately. In this work, a novel radiation efficiency measurement method is developed and verified for measurement of passive ultra high frequency (UHF) RFID dipole tag antenna in order to characterise the tag antenna structure losses in practise. The method is purely based on measurements of three fundamental tag antenna parameters: realised gain, directivity, and power transmission coefficient. Even though the measurement method is prone to errors, and limited, although reasonable, measurement accuracy is achieved, it provides a powerful tool for characterisation of complex antenna material structures losses. The acquired information can be used to optimise tag antenna material structures and to improve tag antenna performance and reliability, which is crucial for widespread use of RFID to become reality.

TIIVISTELMÄ

TAMPEREEN TEKNILLINEN YLIOPISTO
Sähkötekniikan koulutusohjelma
KOSKI, EVELIINA: Säteilyhyötysuhteen mittausmenetelmä balansoiduille passiivisille UHF RFID dipolityyppisille tunnisteantenneille
Diplomityö, 89 sivua
Marraskuu 2012
Pääaine: Suurtaajuustekniikka
Tarkastajat: Apulaisprofessori Leena Ukkonen ja Professori Lauri Sydänheimo
Avainsanat: Ommeltu antenni, realisoitunut vahvistus, *S*-parametri menetelmä, suuntaavuuden arviointi, säteilyhyötysuhde, tehonsiirtokerroin, UHF RFID

Radiotaajuinen tunnistus (engl. Radio Frequency Identification, RFID) on nopeasti kehittyvä tekniikka kohteiden langatonta tunnistusta varten. RFID järjestelmässä tunnistettavat kohteet varustetaan tunnisteilla. Tunnisteet koostuvat antennista sekä sovelluskohtaisesta integroidusta piiristä. Integroidun piirin muisti sisältää tunnistettavan kohteen yksilöllisen elektronisen tunnistekoodin (engl. Electronic Product Code, EPC). RFID lukija aistii tunnistekoodin. Passiivisen UHF (engl. Ultra High Frequency) RFID järjestelmän hyvyys määräytyy pitkälti tunnisteen ominaisuuksista. Tunniste suunnitellaan toimimaan tietyssä sovellusympäristössä mahdollisimman pitkän tunnistusetäisyyden takaamiseksi. Viime aikoina RFID on saanut lääketieteellisissä sovelluskohteissa merkittävästi huomiota. Näissä sovelluksissa puettavat RFID tunnisteet ihmiskehon lähellä voisivat mahdollistaa ihmisen langattoman reaaliaikaisen biomonitoroinnin. RFID:n jatkuvan kehityksen ohella uudenlaiset antennimateriaalit sekä -rakenteet uusiin RFID sovelluskohteisiin ovat herättäneet kiinnostusta. Uudenlaiset tunnisteet, joissa antennirakenteet muodostetaan tulostamalla johtavaa mustetta tai ompelemalla johtavalla langalla, ovat osoittautuneet kilpailukykyisiksi materiaaleiksi perinteisen etsatun kuparin rinnalla. Johtava muste voidaan tulostaa erilaisiin joustaviin substraatteihin tai suoraan tunnistettavaan kohteeseen. Ommellut tunnisteet voidaan vaivattomasti ja saumattomasti integroida vaatekappaleisiin ja ne ovat kuin räätälöity puettavan elektroniikan sovelluksiin.

Uusien materiaalien tarkka mallinnus on haastavaa niiden muodostaessa monimutkaisia antennirakenteita ja substraatteja. Tässä työssä kehitetään ja verifioidaan uudenlainen menetelmä passiivisten UHF RFID dipoli-tyyppisten antennitunnisteiden säteilyhyötysuhteen mittaamiseen. Menetelmän avulla saadaan arvokasta tietoa antennirakenteen todellisista häviöistä. Esitetty menetelmä nojautuu puhtaasti kolmen fundamentaalisen tunnisteparametrin mittaamiseen: realisoituneeseen vahvistukseen, suuntaavuuteen sekä tehonsiirtokertoimeen. Vaikka mittausmenetelmä on altis mittausvirheille ja tarjoaa rajoitetun, mutta tyydyttävän mittaustarkkuuden, se mahdollistaa tehokkaan työkalun monimutkaisten antennirakenteiden häviöiden karakterisoimiseen. Mittauksesta saatu tieto voidaan hyödyntää antennirakenteiden optimoimiseen sekä tunnisteantennin suorituskyvyn ja luotettavuuden parantamiseen. Tämä on tärkeä edellytys RFID:n laajan käyttöönoton toteutumiselle.

PREFACE

This work is conducted at Tampere University of Technology (TUT), at the Department of Electronics. This research work has been funded by the Finnish Funding Agency for Technology and Innovation (TEKES, KÄKI research project) and Centennial Foundation for Technology Industries. The objective was to develop a measurement method for measuring the radiation efficiency of balanced passive radio frequency identification (RFID) dipole tag antennas. The measurement method can be used to characterise new tag materials that are challenging to model. Such materials could be found in sewed tags, which are used for implementation of wearable RFID tag antennas for body-centric wireless communication. The losses within the tag antenna structure for inkjet-printed tags along with metal mountable tags are in addition characterisable with the proposed radiation efficiency measurement method.

Examiners of this thesis are Adjunct Professor Leena Ukkonen and Professor Lauri Sydänheimo. I would like to thank Professor Lauri Sydänheimo and Adjunct Professor Leena Ukkonen for giving me the opportunity to work in the Wireless Identification and Sensing Systems (WISE) Research Group, and also for giving me this interesting topic. I would also like to thank the instructor of this thesis, Research Fellow Toni Björninen, for his valuable support and advice. In addition, I would like to thank the researchers in the WISE Research Group for constructive discussions and guidance. My last words of thank are dedicated to my boyfriend, who bound this thesis with love, encouragement, and patience.

Tampere, 5 October 2012

_____

Eveliina Koski

CONTENTS

ABBREVIATIONS

AIDC	Automatic Identification and Data Collection
AR	Axial Ratio
ASIC	Application Specific Integrated Circuit
ASK	Amplitude Shift Keying
CEPT	European Conference of Postal and Telecommunications
CW	Carrier Wave
DC	Direct Current
DSB-ASK	Double-Sideband Amplitude Shift Keying
EIRP	Equivalent Isotropically Radiated Power
EPC	Electronic Product Code
ERP	Equivalent Radiated Power
ETSI	European Telecommunications Standards Institute
FCC	Federal Communications Commission
FM0	Bi-Phase Space
FNBW	First Null BeamWidth
HF	High Frequency
HFSS	High Frequency Structure Simulator
HPBW	Half-Power BeamWidth
ITU	International Telecommunication Union
LF	Low Frequency
MPT	Ministry of Posts and Telecommunications
PIE	Pulse-Interval Encoding
PR-ASK	Phase-Reversal Amplitude Shift Keying
PSK	Phase Shift Keying
RCS	Radar Cross Section
RFID	Radio Frequency IDentification
RX	Receiver
SMA	SubMiniature version A
TEM	Transverse ElectroMagnetic
TX	Transmitter
UHF	Ultra High Frequency
VNA	Vector Network Analyser
VSWR	Voltage Standing Wave Ratio

SYMBOLS

A_e	Effective aperture [m^2]
λ	Wavelength [m]
α	Attenuation constant [1/m]
B	Magnetic flux density [Wb/m^2]
β	Phase constant [rad/m]
D	Electric flux density [$Coul/m^2$], directivity
$d\Omega$	Element of solid angle [sr]
δ	Skin depth [m]
E	Electric field intensity [V/m]
e	Radiation efficiency
ε	Permittivity [F/m]
f	Frequency [Hz]
G	Gain [dBi]
Γ	Voltage reflection coefficient
γ	Propagation constant [1/m]
H	Magnetic field intensity [A/m]
I	Current [A]
J	Electric current density [A/m^2]
k	Wave number [1/m]
Ω	Beam solid angle [sr]
ω	Angular frequency [rad/s]
μ	Permeability [H/m]
P	Power [W]
R	Resistance [Ω]
r	Distance [m]
ρ	Electric charge density [$Coul/m^3$]
S	Radiation density [W/m^2]
σ	Conductivity [S/m], Radar cross section [m^2]
$\tan\delta_c$	Loss tangent
τ	Power transmission coefficient
U	Radiation intensity [W/sr]
V	Voltage [V]
v_p	Phase velocity [m/s]
W	Effect [Ws]
X	Reactance [Ω]
Z	Impedance [Ω]

1 INTRODUCTION

Automatic Identification and Data Collection (AIDC) refers to different technologies use to directly entry information data into a computer system, programmable logic controller or other microprocessor-controlled device without the involvement of a human. These technologies provide reliable solutions not only for item and human identification, but also for tracking. Comprehensive details about the item or human can easily be collected with minimal enforcement. AIDC include technologies such as bar code, radio frequency identification, magnetic stripe, voice and vision systems, optical character recognition and biometrics [1]. Each of these technologies provides specific advantages and features, making it suitable for a specific application environment. However, they all eliminate two error prone and time consuming activities: manual data collection and data entry into computer systems. Hereby, AIDC provides quick, accurate and cost effective solution for data collection end entry. Further, it is possible to attain in great detail how long a processing step for example in manufacturing line takes and to quickly reallocate resources to remove bottlenecks.

Particularly, passive Radio Frequency Identification (RFID) systems operating at Ultra High Frequency (UHF) are quickly developing and gaining a foothold in application areas such as identification, security, and item tracking. UHF RFID enables industry participants to gain enhanced visibility along the supply chain, resulting in cost and process efficiencies for all trading partners. In a typical passive UHF RFID system the objects to be identified are labelled with tags consisting of an antenna and an Application Specific Integrated Circuit (ASIC). The identification is established by readers located in the surrounding and “sensing” the tags [2]. The passive tags do not comprise any type of power supply, and the communication between the tag and the reader is based on backscattering of electromagnetic waves from the tag antenna. The key performance parameter of the passive UHF RFID system is the read range, which is the maximum distance at which the communication between the tag and the reader still can be established. A proper impedance matching between the tag antenna and the chip is of paramount importance for maximising the read range, as well as optimising the antenna geometry for high radiation efficiency. In addition, low loss tag antenna materials are crucial for long range passive UHF RFID applications. The tag plays a key role in the quality of the overall RFID system performance. Tag modelling and simulation are necessary and it is a critical step in the design and optimisation process to predict the tag performance. This requires accurate electromagnetic modelling of the tag structure, the tag materials, and the tag specific application environment.

If much power is lost within the tag antenna due to poor radiation efficiency, the tag antenna gain is decreased resulting in reduced read range. Radiation efficiency takes only into account the ohmic losses within the tag antenna structure and excludes losses introduced by mismatches between the tag antenna and chip impedances. More recently, research is focused on wearable RFID applications, in which the RFID tag is utilised in close proximity to the human body. As suggested in [3–6], conductive thread sewed directly on non-conductive fabric could form the tag antenna. The modelling becomes challenging when the conductive antenna patterns are non-uniform and covers both sides of the substrate. The measurement of radiation efficiency could be used to characterise the tag material and the geometry losses that are challenging to model. Losses within inkjet-printed tags and metal mountable tags could in addition be characterised by measurement of radiation efficiency. The obtained information could be used to optimise the tag geometry and conductive pattern for certain tag materials.

In this work, a novel radiation efficiency measurement method is proposed for measurement of balanced passive UHF RFID dipole tag antennas. The method is applicable for tag antennas in free space and thus the measured results can be used to characterise tag antenna structure losses. However, the measurement method has the potential to be further developed for radiation efficiency measurement of the tag antenna in its real application environments. For example, the sewed tag antennas may be directly measured for radiation efficiency when attached to the human body.

The rest of this work is structured as follows. The theoretical background presented in Chapter 2 provides the basic electromagnetic theory and the electromagnetic wave propagation. Additionally, the fundamental antenna parameters are presented and a detailed description of the passive UHF RFID system is given. The author’s contribution and the actual topic are presented on theory level in Chapter 3. The theory is further supplemented and verified with practical measurement results in Chapter 4. Finally, the work is concluded in Chapter 5.

2 THEORECTICAL BACKGROUND

This section provides the basic laws of electromagnetism and the fundamental antenna parameters. The passive UHF RFID system is introduced.

2.1 Electromagnetic theory

When the frequency increases, the wavelength decreases. The voltages and currents for a radio frequency system no longer remain spatially constant when compared to the geometric size of the discrete circuit element. The lumped element circuit analysis using Kirchhoff's voltage and current laws fail because it does not account for the spatial variations of current and voltage. Instead, the voltages and currents have to be treated as propagating waves, and lumped circuit elements as distributed circuit elements.

2.1.1 Maxwell's equations

When the physical dimensions and electric properties of the transmission line are known, the distributed circuit parameters are determined using the Maxwell's equations, which are presented in Table 2.1. *S* denotes a surface in space, *V* a volume in space, and *l* a curve in space. The electromagnetic quantities and units are gathered in Table 2.2. Maxwell's equations link the electric and magnetic field quantities. This linkage is responsible for wave propagation and implies that any acceleration of an electric charge or change in the magnetic field produces radiation. The acceleration of charge, or current, creates a changing magnetic field, which in turn creates a changing electric field. Further, the changing electric field creates a changing magnetic field and so on. In free-space, the field intensities and flux densities are related through [7]

$$\boldsymbol{B} = \mu_0 \boldsymbol{H}, \boldsymbol{D} = \varepsilon_0 \boldsymbol{E}, \text{and } \boldsymbol{J} = 0. \tag{2.1}$$

Faraday's law states that the time-varying magnetic flux as a source creates a time-varying electric field that is proportional to the rate of change of the magnetic field. Ampère-Maxwell law states that the time-varying electric flux and the moving of charges, that is, the electric current, as a source create a rotational magnetic field. Gauss's law for electricity relates the distribution of electric charge to the resulting electric field, and Gauss's law for magnetism states that magnetic charges do not exist by formulating that magnetic flux lines are closed or circulating.

The differential and integral forms of Maxwell's equations are valid for arbitrary time dependence. When the fields have a harmonic time dependence the phasor form is

used, in which the fields have a sinusoidal time dependence of angular frequency $\omega = 2\pi f$, where f is the frequency. The relationship between the time-varying real field $\boldsymbol{E}$ as a function of spatial coordinates and phasor field $\overline{E}$ is [7–8]

$$\boldsymbol{E}(x,y,z,t) = \mathrm{Re}\left[\overline{E}(x,y,z)e^{j\omega t}\right], \tag{2.2}$$

and similarly for the magnetic field. The phasor quantities are complex-valued functions of spatial coordinates only. The real physical fields are attained as the real part of the complex vector fields.

TABLE. 2.1 Maxwell's equations in a nutshell [7–8].

Differential form	Phasor form	Integral form	Designation
$\nabla\times\boldsymbol{E} = -\frac{\partial \boldsymbol{B}}{\partial t}$	$\nabla\times\overline{E} = -j\omega\overline{B}$	$\int_{\partial S}\boldsymbol{E}\cdot d\boldsymbol{l} = -\frac{\partial}{\partial t}\int_{S}\boldsymbol{B}\cdot d\boldsymbol{s}\ \forall S$	Faraday's law (2.3)
$\nabla\times\boldsymbol{H} = \boldsymbol{J} + \frac{\partial \boldsymbol{D}}{\partial t}$	$\nabla\times\overline{H} = \overline{J} + j\omega\overline{D}$	$\int_{\partial S}\boldsymbol{H}\cdot d\boldsymbol{l} = \int_{S}\boldsymbol{J}\cdot d\boldsymbol{s} + \frac{\partial}{\partial t}\int_{S}\boldsymbol{D}\cdot d\boldsymbol{s}\ \forall S$	Ampère-Maxwell law (2.4)
$\nabla\cdot\boldsymbol{D} = \rho$	$\nabla\cdot\overline{D} = \rho$	$\int_{\partial V}\boldsymbol{D}\cdot d\boldsymbol{s} = \int_{V}\rho\, dv = Q\ \forall V$	Gauss's law for electricity (2.5)
$\nabla\cdot\boldsymbol{B} = 0$	$\nabla\cdot\overline{B} = 0$	$\int_{\partial V}\boldsymbol{B}\cdot d\boldsymbol{s} = 0\ \forall V$	Gauss's law for magnetism (2.6)

TABLE. 2.2 Electromagnetic quantities and units [7–8].

Quantity	Symbol	Unit
Electric field intensity (phasor form, real form)	$\overline{E}, \boldsymbol{E}$	V/m
Magnetic field intensity (phasor form, real form)	$\overline{H}, \boldsymbol{H}$	A/m
Electric flux density (phasor form, real form)	$\overline{D}, \boldsymbol{D}$	Coul/m^2
Magnetic flux density (phasor form, real form)	$\overline{B}, \boldsymbol{B}$	Wb/m^2
Electric current density (phasor form, real form)	$\overline{J}, \boldsymbol{J}$	A/m^2
Electric charge density	ρ	Coul/m^3
Vacuum permittivity	ε_0	8.854×10^{-12} F/m
Permittivity	ε	F/m
Complex permittivity	ε_c	F/m
Relative permittivity	$\varepsilon_r = \varepsilon/\varepsilon_0$	–
Relative complex permittivity	$\varepsilon_{r,c} = \varepsilon_c/\varepsilon_0$	–
Vacuum permeability	μ_0	$4\pi\times10^{-7}$ H/m
Permeability	μ	H/m
Complex permeability	μ_c	H/m
Relative permeability	$\mu_r = \mu/\mu_0$	–
Relative complex permeability	$\mu_{r,c} = \mu_c/\mu_0$	–
Conductivity	σ	S/m

The continuity equation is obtained from the Ampère-Maxwell's law, and is expressed using the differential and integral forms as [7]

$$\nabla \cdot \boldsymbol{J} = -\frac{\partial \rho}{\partial t} \Leftrightarrow \int_{\partial V} \boldsymbol{J} \cdot ds = -\int_{V} \frac{\partial \rho}{\partial t} dv. \tag{2.7}$$

The continuity equation states that charge is conserved and that current is continues. The term $\nabla \cdot \boldsymbol{J}$ represents the outflow of current at a point, and $\partial\rho/\partial t$ represents the charge build-up with time at the same point. The displacement current $\partial \boldsymbol{D}/\partial t$ is necessary in Ampère-Maxwell's law to ensure the charge conservation law in a time-varying case.

2.1.2 Fields in media and electromagnetic boundary conditions

When the electromagnetic waves are in free space, the field vectors are related through (2.1). In practise, the electromagnetic fields exist in media and are related to each other by the constitutive relations. The absolute permittivity ε and absolute permeability μ represents the properties of the medium. In an electromagnetic field, the total electromagnetic force on a charge q in a medium is given by the Lorentz's force equation [9]:

$$\overline{F} = q\left(\overline{E} + \overline{u} \times \overline{B}\right), \tag{2.8}$$

where $\overline{u}$ is the charge velocity vector. In materials having free charges ($\sigma \neq 0$), part of the power carried by the electromagnetic field is used to accelerate the charges, causing currents in the material. The charged particles in a material medium both respond to the electric and magnetic fields and generate these fields. The constitutive relations for a linear and isotropic media can be gathered as [9]

$$\begin{aligned} \overline{D} &= \varepsilon \overline{E}, \\ \overline{B} &= \mu \overline{H}, \\ \overline{J} &= \sigma \overline{E}, \end{aligned} \tag{2.9}$$

where the μ, ε, and σ are scalars. For a linear and isotropic medium, the polarisation (magnetisation) is directly proportional to the electric (magnetic) field intensity, and the proportionality constant is independent of the direction of the field. If the relative permittivity ε_r (relative permeability μ_r) is independent of space coordinates, the dielectric (magnetic) medium is homogeneous. A linear, isotropic, and homogeneous medium is referred to as a simple medium [9]. Electromagnetic problems involve contiguous regions of materials with different electrical properties or constitutive parameters. Therefore, it is necessary to known the boundary conditions that the field

vectors ***E***, ***D***, ***B*** and ***H*** must satisfy at the interfaces. The integral form of Maxwell's equations hold for regions containing discontinuous material and are applied to a small region at an interface of two materials to derive the boundary conditions. [9] The following boundary conditions hold at an arbitrary interface of material and/or surface currents [7–9]:

$$\begin{aligned} \bar{n}\times\left(\bar{E}_2-\bar{E}_1\right)&=\bar{0},\\ \bar{n}\times\left(\bar{H}_2-\bar{H}_1\right)&=\bar{J}_s,\\ \bar{n}\cdot\left(\bar{D}_2-\bar{D}_1\right)&=\rho_s,\\ \bar{n}\cdot\left(\bar{B}_2-\bar{B}_1\right)&=0, \end{aligned} \tag{2.10}$$

where $\bar{n}$ is the normal vector pointing from medium 1 to medium 2. The fields in medium 1 and its constitutive properties are denoted with index 1, and those of medium 2 are denoted with index 2. Fields parallel to the normal component are denoted with subscript *n*, and fields parallel to the surface or tangential fields are denoted with subscript *t*. The magnitudes of $\bar{E}$, $\bar{H}$, $\bar{D}$, $\bar{B}$, and $\bar{J}$ are *E*, *H*, *D*, *B*, and *J*, respectively. All field quantities in the boundary condition equations are evaluated at the boundary and the equations apply to each point along the boundary. According to the general boundary conditions expressed in (2.10), the tangential component of an electric field is continuous across a medium interface $\left(E_{1t}=E_{2t}\right)$, the tangential component of a magnetic field is discontinuous across a medium interface where a surface current exists, and the amount of discontinuity is determined by the surface current $\left(H_{2t}=H_{1t}+J_s\right)$. Further, the normal component of an electric flux density field is discontinuous across a medium interface where a surface charge exists, and the amount of discontinuity is determined by the surface charge $\left(D_{2n}=D_{1n}+\rho_s\right)$. Finally, the normal component of a magnetic flux density field is continuous across a medium surface $\left(B_{1n}=B_{2n}\right)$.

2.1.3 Electromagnetic plane wave propagation

Helmholtz wave equations

For wireless data transfer applications, the most important outcome of Maxwell's equations is that energy can be transferred as electromagnetic radiation. Electromagnetic radiation may exist in wave form, and these waves can propagate independently of their sources. The electromagnetic wave propagation problems often involve a source free region where ρ and $\bar{J}$ are zero. In a simple (source-free, linear, isotropic and homogeneous) non-conducting (σ = 0) medium characterised by permittivity ε and permeability μ, the wave equations, which are derived from Maxwell's equations, become [9]:

$$\begin{cases} \nabla^2 \boldsymbol{E} - \mu\varepsilon \dfrac{\partial^2 \boldsymbol{E}}{\partial t^2} = 0, \\ \nabla^2 \boldsymbol{H} - \mu\varepsilon \dfrac{\partial^2 \boldsymbol{H}}{\partial t^2} = 0. \end{cases} \tag{2.11}$$

All propagating waves in simple medium, for example vacuum, fulfil Eq. (2.11). For the time-harmonic case, the wave equations are derived from the phasor forms of Maxwell's equations. In a source-free simple medium, the wave equations become [7]:

$$\begin{cases} \nabla^2 \overline{E} + \omega^2 \mu\varepsilon \overline{E} = \nabla^2 \overline{E} + k^2 \overline{E} = 0, \\ \nabla^2 \overline{H} + \omega^2 \mu\varepsilon \overline{H} = \nabla^2 \overline{H} + k^2 \overline{H} = 0. \end{cases} \tag{2.12}$$

These are the Helmholtz's equations. A constant $k = \omega\sqrt{\mu\varepsilon}$ having the unit 1/m is defined and called the wave number of the medium [7].

If the simple medium is conducting ($\sigma \neq 0$), a current $\overline{J} = \sigma \overline{E}$ will flow, and the Maxwell's curl equation for the magnetic field becomes [9]

$$\nabla \times \overline{H} = j\omega \overline{D} + \overline{J} = j\omega \left(\varepsilon + \frac{\sigma}{j\omega} \right) \overline{E} = j\omega \varepsilon_c \overline{E}, \tag{2.13}$$

with

$$\varepsilon_c = \varepsilon' - \varepsilon'' = \varepsilon - j\frac{\sigma}{\omega} \tag{2.14}$$

being the complex permittivity of the medium. In low-loss media, damping losses are very small, and the real part of ε_c is usually written as ε without a prime [9], as seen above. An external time-varying field applied to dielectric material bodies force the bound charges in the medium to slightly move from their equilibrium positions, causing electric dipoles or dielectric polarisation. The electric dipoles interact with the external field, providing the material the ability to store electric energy. Energy is stored in the electric dipoles by the restraining forces on the electric dipoles when they are subjected to external applied electric field. The relative permittivity ε_r is a measure of the relative charge or energy storage capability of a dielectric material. The imaginary part of ε accounts for loss in the medium (heat) due to damping of the vibrating dipole moments. The heat losses are mainly caused by the electrical dipoles, which cannot vary with the same frequency as that of the applied electric field, leading to frictional damping that causes power loss. In practise, materials are always lossy, containing free charge carriers that case ohmic losses. Both the damping effect and the ohmic losses are included in the imaginary part of the complex permittivity. The permittivity is complex

for lossy dielectric materials [9]. An analogous situation occurs for magnetic materials. An applied magnetic field may align magnetic dipole moments in a magnetic material to produce a magnetic polarisation or magnetisation. The permeability is complex for a lossy magnetic medium [9]:

$$\mu_c = \mu' - \mu'' = \mu - \mu''. \tag{2.15}$$

Again, the imaginary part μ'' of the μ_c accounts for loss due to damping forces, but there is no magnetic conductivity since there is no magnetic current [7]. Most non-magnetic materials are not affected by the magnetic field and their scalar permeability μ is close to that of free-space, that is, μ_0.

For a lossy dielectric medium, the real k in the Helmholtz's equations should be changed to a complex wave number k_c:

$$k_c = \omega\sqrt{\mu\varepsilon_c}. \tag{2.16}$$

The ratio of the imaginary part and the real part of the complex permittivity is defined as the loss tangent because it is a measure of the power loss in the medium [9]:

$$\tan\delta_c = \frac{\varepsilon''}{\varepsilon'}. \tag{2.17}$$

The larger the value of the loss tangent, the more the material converts energy from electric field into heat. The loss tangent does not separate the dielectric polarisation losses from the conduction losses, but discloses only the total power loss in the material. Microwave materials are often characterised by specifying the real permittivity $\varepsilon = \varepsilon' = \varepsilon_r \varepsilon_0$, and the loss tangent at a certain frequency [7].

Plane waves in lossless medium

Plane waves are waves that have a one-dimensional spatial dependence. A uniform plane wave propagates along some fixed direction (say z-direction) and its electric and magnetic fields have no dependence on the transverse coordinates x and y, but are only functions of z and time t. A uniform plane wave is characterised by an $\boldsymbol{E}$ having same direction, magnitude, and phase in infinite planes perpendicular to the direction of propagation, and similarly for $\boldsymbol{H}$. Such waves do not exist in practise, since it would need a source infinite in extent to create it. But if the observer is far enough from the source, the wave front becomes almost spherical and a very small portion of the giant sphere is very nearly a plane wave. A uniform plane wave is a transverse electromagnetic (TEM) wave, meaning that the electric and magnetic are perpendicular to the direction of propagation and to each other [9].

For a lossless medium k is real. A plane wave solution to the equation in (2.12) can be found by considering an electric field with only a x-component and uniform (no variation) in the x and y direction. The only variation occurs in the z direction. In this case, the Helmholtz equations reduce to [7]

$$\frac{\partial^2 E_x}{\partial z^2} + k^2 E_x = 0, \tag{2.18}$$

whose time harmonic solution for frequency ω is

$$E_x(z) = E^+ e^{-jkz} + E^- e^{jkz}. \tag{2.19}$$

The E^+ and E^- are arbitrary amplitude constants. If these constants are assumed real, the solution can be written in time domain as [7]

$$\boldsymbol{E}_x(z,t) = E^+ \cos(\omega t - kz) + E^- \cos(\omega t + kz). \tag{2.20}$$

The first term in (2.20) represents a wave travelling in the forward direction. This can be seen by considering that in order to maintain a fixed point on the wave, that is, $\omega t - kz$ = constant, one needs to move in the $+z$ direction as time increases. Similarly, the second term in (2.20) represents a wave travelling in the negative z direction. Hence, the amplitude constants for the forward and reverse travelling waves are denoted with superscripts + and –, respectively. The phase velocity of the wave is the velocity at which a fixed phase point on the wave travels. The phase velocity is given by [7]

$$v_p = \frac{\omega}{k} = \frac{1}{\sqrt{\mu\varepsilon}}. \tag{2.21}$$

In free-space, we have $v_p = 1/\sqrt{\mu_0 \varepsilon_0} = c = 2.998 \times 10^8$ m/s, which is the speed of light. The wave length λ is defined as the distance between two successive maxima on the wave at a fixed instant of time and it is expressed as [7]

$$\lambda = \frac{2\pi}{k} = \frac{2\pi v_p}{\omega} = \frac{v_p}{f}. \tag{2.22}$$

The electric field is given by (2.19), and the magnetic field is soluble from the Maxwell's curl equations. The result is a magnetic field which $H_x = H_z = 0$, and [7]

$$H_y(z) = \frac{1}{\eta}\left(E^+ e^{-jkz} - E^- e^{jkz}\right), \tag{2.23}$$

where $\eta = \omega\mu/k = (\mu/\varepsilon)^{1/2}$ is the wave impedance of the plane wave, and defined as the ratio of the electric and magnetic fields. In free space we have $\eta_0 = (\mu_0/\varepsilon_0)^{1/2} = 377\ \Omega$. The electric and magnetic fields are orthogonal to each other and to the direction of propagation. A plane wave propagating in the +*z* direction is depicted below.

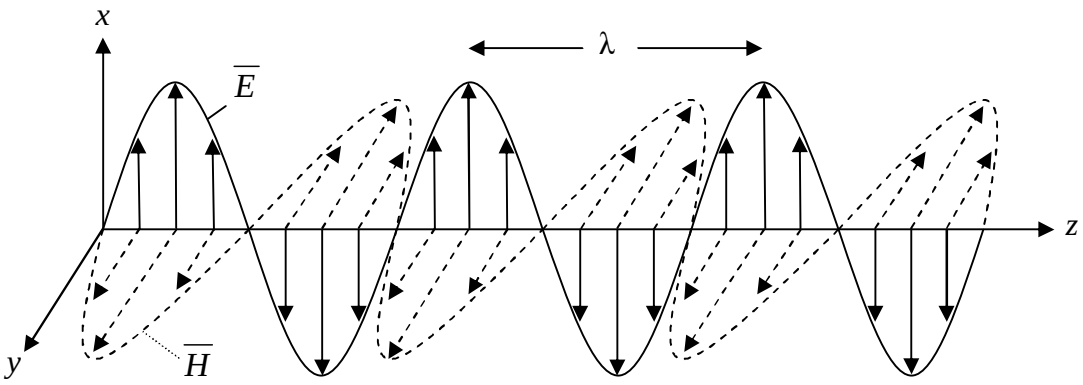

FIG. 2.1 A uniform electromagnetic plane wave propagating in the positive *z* direction at time *t*.

Plane waves in lossy dielectric medium

If the source-free medium is lossy, the resulting wave equation for the electric field becomes [9]

$$\begin{cases} \nabla^2 \overline{E} + k_c^2 \overline{E} = \nabla^2 \overline{E} - \gamma^2 \overline{E} = 0, \\ \nabla^2 \overline{H} + k_c^2 \overline{H} = \nabla^2 \overline{H} - \gamma^2 \overline{H} = 0, \end{cases} \tag{2.24}$$

where the complex propagation constant γ (1/m) is defined as [9]

$$\gamma = jk_c = j\omega\sqrt{\mu\varepsilon_c} = \alpha + j\beta. \tag{2.25}$$

The complex propagation constant can be expressed in two forms [7, 9]:

$$\gamma = \alpha + j\beta = j\omega\sqrt{\mu\varepsilon}\sqrt{1 + \frac{\sigma}{j\omega\varepsilon}}, \tag{2.26}$$

$$\gamma = \alpha + j\beta = j\omega\sqrt{\mu\varepsilon'}\sqrt{1 - j\frac{\varepsilon''}{\varepsilon'}}. \tag{2.27}$$

The positive constants α and β are the real and the imaginary parts of γ, respectively. For a lossless medium, we have that $\sigma = 0$ ($\varepsilon'' = 0$), $\alpha = 0$, and $\beta = k = \omega\sqrt{\mu\varepsilon}$. Again, if

we assume that the electric field only has a *x*-component and uniform in *x* and *y*, the wave equation for the electric field in (2.24) reduces to [7]

$$\frac{\partial E_x}{\partial z^2} - \gamma^2 E_x = 0, \tag{2.28}$$

which has a solution

$$E_x(z) = E^+ e^{-\gamma z} + E^- e^{\gamma z}. \tag{2.29}$$

The positive travelling wave then has a propagation factor of the form

$$e^{-\gamma z} = e^{-\alpha z} e^{-j\beta z}, \tag{2.30}$$

which in time domain is of the form

$$e^{-\alpha z}\cos(\omega t - \beta z). \tag{2.31}$$

This represents a wave travelling in the positive *z* direction with a phase velocity $v_p = \omega/\beta$, a wavelength $\lambda = 2\pi/\beta$, and an exponential damping factor. The rate of decay with distance is given by the attenuation constant α (1/m) and the amount of phase shift that occurs when the wave travels one meter is called the phase constant β (rad/m) [9]. Next, the associated magnetic field can be calculated as [7]

$$H_y(z) = \frac{j}{\omega\mu}\frac{\partial E_x}{\partial z} = \frac{-j\gamma}{\omega\mu}\left(E^+ e^{-\gamma z} - E^- e^{\gamma z}\right). \tag{2.32}$$

As with the lossless case, the wave impedance can be defined to relate the electric and magnetic fields [7]:

$$\eta = \frac{j\omega\mu}{\gamma}. \tag{2.33}$$

Then (2.32) can be written as

$$H_y(z) = \frac{1}{\eta}\left(E^+ e^{-\gamma z} - E^- e^{\gamma z}\right). \tag{2.34}$$

The wave impedance η is in general complex, and it reduces to the lossless case $\eta = \sqrt{\mu/\varepsilon}$ when $\gamma = jk = j\omega\sqrt{\mu\varepsilon}$. The electric and the magnetic fields are

perpendicular to each other and to the propagation direction, as for the lossless case. This time, however, the fields attenuate exponentially as the electromagnetic wave propagates in the lossy dielectric medium.

Plane waves in good conductor and skin depth

Many electromagnetic problems involve loss or attenuation due to good, but not perfect, conductors. A good conductor represents a case where $\sigma/(\omega\varepsilon) >> 1$ [7, 9]. In this case, (2.26) can be simplified by neglecting 1 in comparison with the term $\sigma/(\omega\varepsilon)$:

$$\gamma = \alpha + j\beta \cong j\omega\sqrt{\mu\varepsilon}\sqrt{\frac{\sigma}{j\omega\varepsilon}} = \frac{1+j}{\sqrt{2}}\sqrt{\omega\mu\sigma} = (1+j)\sqrt{\frac{\omega\mu\sigma}{2}}. \tag{2.35}$$

(2.35) indicates that α and β are for a good conductor approximately equal:

$$\alpha = \beta = \sqrt{\frac{\omega\mu\sigma}{2}} = \sqrt{\pi f\mu\sigma}. \tag{2.36}$$

At very high frequencies the attenuation constant α tends to be very large for a good conductor. Since the attenuation constant is $e^{-\alpha z}$, the amplitude of the wave will be attenuated by a factor of $e^{-1} = 0.368$ when it travels a distance of $z = \delta = 1/\alpha$ (m). A high frequency electromagnetic wave is attenuated very rapidly as it propagates in a good conductor. The distance δ is called the skin depth or depth of penetration [7, 9]:

$$\delta = \frac{1}{\alpha} = \frac{1}{\sqrt{\pi f\mu\sigma}}. \tag{2.37}$$

Since $\alpha = \beta$ for a good conductor, the skin depth can also be written as

$$\delta = \frac{1}{\beta} = \frac{\lambda}{2\pi}, \tag{2.38}$$

where λ is the wavelength in the good conductor. At microwave frequencies the skin depth of a good conductor is so small, that fields and currents can be considered as confined in a very thin layer of the conductor surface. Only a thin plating of a good conductor, for example copper, is necessary for low-loss microwave components [7, 9]. A summary of the results for plane wave propagation in various media is presented in Table 2.3.

TABLE. 2.3 Plane wave propagation in various media [7].

Quantity	Type of medium		
	Lossless ($\sigma = \varepsilon'' = 0$)	Lossy dielectric	Good conductor ($\sigma/(\omega\varepsilon) >> 1$)
Propagation constant	$\gamma = j\omega\sqrt{\mu\varepsilon}$	$\gamma = j\omega\sqrt{\mu\varepsilon}$	$\gamma \cong (1+j)\sqrt{\omega\mu/(2\sigma)}$
Phase constant	$\beta = \omega\sqrt{\mu\varepsilon}$	$\beta = \mathrm{Im}(\gamma)$	$\beta = \mathrm{Im}(\gamma) \cong \sqrt{\omega\mu/(2\sigma)}$
Attenuation constant	$\alpha = 0$	$\alpha = \mathrm{Re}(\gamma)$	$\alpha = \mathrm{Re}(\gamma) \cong \sqrt{\omega\mu/(2\sigma)}$
Wave impedance	$\eta = \sqrt{\mu/\varepsilon}$	$\eta = j\omega\mu/\gamma$	$\eta = (1+j)\sqrt{\omega\mu/(2\sigma)}$
Skin depth	$\delta = \infty$	$\delta = 1/\alpha$	$\delta = \sqrt{2/(\omega\mu\sigma)}$
Wave length	$\lambda = 2\pi/\beta$	$\lambda = 2\pi/\beta$	$\lambda = 2\pi/\beta$
Phase velocity	$v_p = \omega/\beta$	$v_p = \omega/\beta$	$v_p = \omega/\beta$

All plane waves discussed above have their electric field pointing in a fixed direction and are so called linearly polarised waves.

Polarisation of plane waves

In general, the polarisation of a plane wave refers to the orientation of the electric field vector, which may be in a fixed direction or may vary with time. For TEM waves, the polarisation is perpendicular to the direction of propagation. The polarisation of a plane wave is the figure the instantaneous electric field traces out with time at a fixed observation point [8, 10]. An example is the vertical, linearly polarised wave in Fig 2.1, which shows the spatial variations of the electric field vector at a fixed instant of time. As time goes on, the electric field at a fixed point oscillates back and forth along a vertical line. In general, the figure traced out is an ellipse. The spatial and temporal variations of the magnetic field are similar to those of the electric field, except that the magnetic field is perpendicular to the electric field [8]. There are some special cases of elliptic polarisation. If the electric field vector moves back and forth along a line, it is linearly polarised. If the electric field vector remains constant in length, but rotates around a circular path, it is said to be circularly polarised. If a wave is travelling towards the observer, and the electric field rotates at an angular frequency of ω clockwise, the electric field is left-hand polarised. Similarly, if the rotation occurs counter clockwise, the electric field is right-hand polarised [8]. Fig. 2.2 gives a space perspective view of a circularly polarised wave. As the vector pattern rotates along the positive *z* axis, the electric field at a fixed point appears to rotate clockwise in the *xy*-plane, yielding a left-hand circularly polarised wave. This is depicted with the time sequence of vectors in the fixed plane.

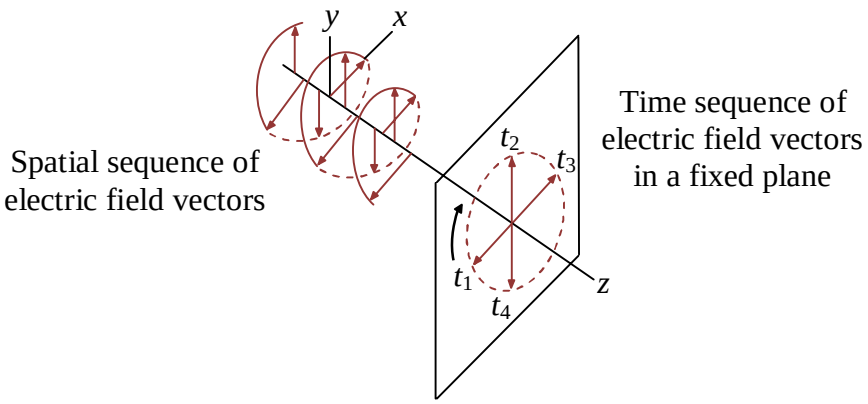

FIG. 2.2 A left-hand circularly polarised wave shown at a fixed instant of time, and the time sequence of electric field vectors as the wave passes through a fixed plane in the positive *z* direction [8].

A general polarisation ellipse is shown in Fig. 2.3, the associated wave is travelling in the positive *z* direction and the sense of rotation can be either right or left. The instantaneous electric field vector $\boldsymbol{E}$ has the components $\boldsymbol{E}_x$ and $\boldsymbol{E}_y$ along the *x*- and *y*-axes. The peak values of these components are E_1 and E_2, respectively.

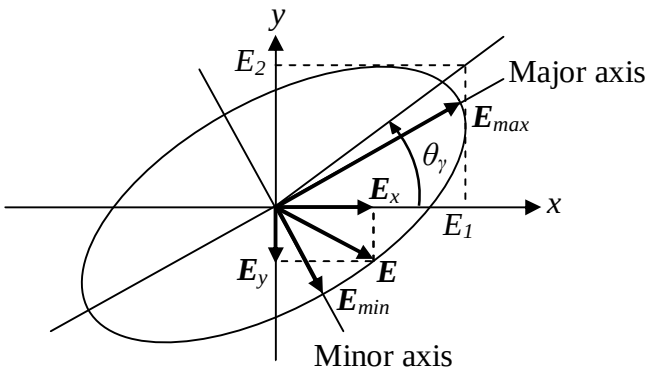

FIG. 2.3 The general polarisation ellipse. The wave propagation direction is approaching. The tip of the instantaneous electric field vector $\boldsymbol{E}$ traces out the ellipse.

The angle θ_γ describes the relative values of E_1 and E_2 [8]:

$$\theta_\gamma = \tan^{-1}\left(\frac{E_2}{E_1}\right), 0° \le \theta_\gamma \le 90°. \tag{2.39}$$

The polarisation ellipse is characterised by the axial ratio (*AR*). The axial ratio is defined as the ratio of the major axis electric field E_{max} component to that of the minor axis E_{min}. The sign of *AR* is positive for right-hand sense of rotation, and negative for left-hand sense of rotation. *AR* is often expressed in decibels as $20\log|AR|$, where $1 \le |AR| \le \infty$. The instantaneous electric field vector $\boldsymbol{E}$ for the wave in Fig. 2.3 can be written for $z = 0$ as [8]

$$\boldsymbol{E} = \boldsymbol{E}_x\bar{x} + \boldsymbol{E}_y\bar{y} = E_1\cos(\omega t)\bar{x} + E_2\cos(\omega t + \phi_\delta)\bar{y}, \tag{2.40}$$

where ϕ_δ is the phase by which the *y*-component leads the *x*-component. This representation describes the ellipse shape as time progresses. If the components are in-phase, meaning that $\phi_\delta = 0$, the net electric vector is linearly polarised. The orientation of the linear polarisation depends on the relative values E_1 and E_2. If $E_1 = 0$, vertical linear polarisation results and if $E_2 = 0$, horizontal linear polarisation results. If E_1 and E_2 are both nonzero a linearly polarised plane wave results at the angle $\tan^{-1}(E_2/E_1)$. Linear polarisation can be thought of as a collapsed ellipse, whose *AR* is infinite. If ϕ_δ is nonzero, the axial ratio is finite. When $\phi_\delta > 0$ the sense of rotation is left-hand, and when $\phi_\delta < 0$, the sense of rotation is right-hand. If $E_1 = E_2$ ($\theta_\gamma = 45°$) and $\phi_\delta = \pm 90°$, the polarisation is circular (left-hand if $\phi_\delta = +90°$ and right-hand if $\phi_\delta = -90°$). For the circular polarisation, the magnitude of the axial ration is unity. The angles θ_γ and ϕ_δ uniquely specify the polarisation state of a wave [8].

2.1.4 Electromagnetic energy and power

In general, a source of electromagnetic energy sets up fields that store electric and magnetic energy and carry power that may be transmitted or dissipated as loss. Poynting's theorem is used to describe the energy conversation for electromagnetic fields and sources. The complex power P_s delivered by the source in a volume *v* bounded by a closed surface *s* equals the sum of the power P_f flowing out of *s*, the time-average power $P_{d,av}$ dissipated in *v*, plus the time-average stored in *v* [8]:

$$P_s = P_f + P_{d,av} + j2\omega\left(W_{m,av} - W_{e,av}\right), \tag{2.41}$$

where the volume *v* has the parameters ε, μ and σ. The complex power flowing out through the closed surface *s* is [8]

$$P_f = \frac{1}{2}\oiint_s \overline{E} \times \overline{H^*} \cdot d\bar{s}, \tag{2.42}$$

where $d\bar{s} = ds\bar{n}$ and $\bar{n}$ is the unit normal to the surface directed out from the surface, and the $\overline{E}$ and $\overline{H}$ are peak phasors. The integrand inside the integral is defined as the Poynting vector, which is a power density with units W/m^2 and it can be expressed with use of the peak phasors of the radiated fields as [8]:

$$\bar{S} = \frac{1}{2}\overline{E} \times \overline{H^*}. \tag{2.43}$$

The time-average dissipated power in volume *v* bounded by closed surface *s* is [8]

$$P_{d,av} = \frac{1}{2}\iiint_v \sigma |E|^2 dv. \tag{2.44}$$

The time-average stored magnetic energy is [8]

$$W_{m,av} = \frac{1}{2}\iiint_v \frac{1}{2}\mu |H|^2 dv, \tag{2.45}$$

and the time-average stored electric energy is [8]

$$W_{e,av} = \frac{1}{2}\iiint_v \frac{1}{2}\varepsilon |E|^2 dv. \tag{2.46}$$

Another way of expressing the source power is [8]

$$P_s = -\frac{1}{2}\iiint_v \overline{E} \cdot \overline{J^*} dv. \tag{2.47}$$

From (2.43) it is seen that the integral of the complex Poynting's vector over a closed surface *s* gives the total complex power flowing out through the surface *s*. The Poynting vector represents the complex power density in watts per square meter at a point. Then the complex power through any surface *s* (not necessarily closed) can be obtained by integrating the complex Poynting vector over that surface. Often, the real power flowing through the surface *s* is of interest, which is obtained as [8]

$$P = \mathrm{Re}\left(\iint_s \overline{S} \cdot d\overline{s}\right) = \frac{1}{2}\mathrm{Re}\left(\iint_s \overline{E} \times \overline{H^*} \cdot d\overline{s}\right). \tag{2.48}$$

The reference power for this average power flow is that of the specified unit normal $\overline{n}$ contained in $d\overline{s} = ds\overline{n}$.

2.2 Antenna theory

An antenna is a transitional structure between free space and a guiding device. The antenna is an electrically conducting device, which can be used to both transmit and receive electromagnetic waves in a specific direction in space. In transmission, an oscillating current on the antenna creates electromagnetic waves. In reception, the free space electromagnetic waves impinging on the antenna structure make the charge

carriers move, resulting in an induced current. By proper antenna design, the transition between free space electromagnetic waves and oscillating current is optimised and the electromagnetic power carried by wave is effectively transferred to the guiding device. With other words, antennas are designed to support charge oscillations. Antennas are reciprocal devices and behave the same on transmit as on receive. Depending on the particular situation, the antenna is treated as a transmitting or a receiving device. All antenna parameters apply hence to both transmitting and receiving antennas.

2.2.1 Radiation principle

Radiation is the creation of electromagnetic fields by the source. These fields are guided within the transmission line and the antenna, and finally detached from the antenna to form free space electromagnetic waves, see Fig. 2.4. As in [10], the generation of electromagnetic waves can be understood by considering a wire as a source, and the creation of free space electromagnetic waves can be explained by an illustration.

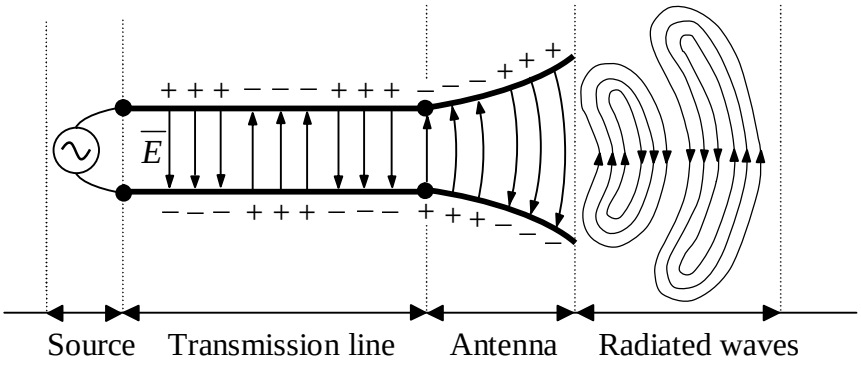

FIG. 2.4 Generation of free-space electromagnetic waves: source, transmission line, antenna, and detachment of electric field lines [10].

Conducting wires are materials that support the motion of electric charges and current flow. An electric charge density ρ_v (Coul/m^3) is distributed uniformly in a circular wire of volume V and a cross-sectional area of A. The total charge Q is moving in the z direction with uniform velocity v_z (m/s), see Fig. 2.5. If the wire is an ideal conductor, with all current residing on the surface of the wire, and if the wire is very thin having ideally zero radius, then the current on the wire I_z can be expressed as [10]

$$I_z = \rho_l v_z, \tag{2.49}$$

where ρ_l (Coul/m) charge density per unit length. For a time-varying current, we have

$$\frac{dI_z}{dt} = \rho_l \frac{dv_z}{dt} = \rho_l \, a_z, \tag{2.50}$$

where a_z is the acceleration. If the wire has a length of l, the (2.50) can be written as

$$l\frac{dI_z}{dt} = l\rho_l \frac{dv_z}{dt} = l\rho_l\, a_z. \tag{2.51}$$

The expression in (2.51) is basic relation of electromagnetic radiation: To create radiation or the electromagnetic fields, there must be an acceleration or deceleration of charge or a time-varying current. According to Maxwell, the acceleration of charge or time-varying current creates a changing magnetic field, which creates a changing electric field. If charge is not moving, current nor radiation is created. If the charge is moving with constant velocity, there is no radiation if the wire is infinitely long but if the wire is curved, bend, discontinuous, terminated or truncated there is radiation. If charge is oscillating in a time-harmonic motion, the wire radiates even if it is straight.

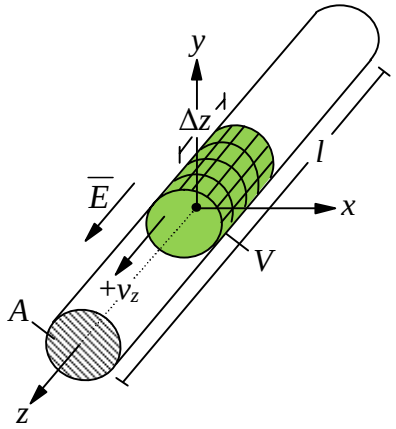

FIG. 2.5 Charge uniformly distributed in a cylinder wire [10].

Next, the creation of free-space electromagnetic waves is visualised. Fig 2.6 shows the lines of force created between the arms of a small centre fed dipole antenna. During the first quarter of the period, during which the charge has reached its maximum value (sinusoidal time variation is assumed), the created three lines have travelled outwardly a radial distance of λ/4. During the following quarter of the period, the original lines have travelled another λ/4, or in total λ/2 from the initial point, and the charge density on the conductors start to decrease. This can be thought of as applying opposite charges which at the end of the first half of a period have neutralised the charges on the conductors. The lines created by the opposite charges are dashed in the figure and they travel a distance λ/4 during the second quarter of the first half of the period. The result is that there are three lines of force pointed upward in the first λ/4 distance, and three lines downwards in the second λ/4 distance. At $t = T/2$ there is no net charge on the antenna, and thus the lines of force are detached from the conductors to unite together to form closed loops. In the second half of the period, the same scenario is followed but in opposite direction. After that, the process is repeated as long as the antenna is excited.

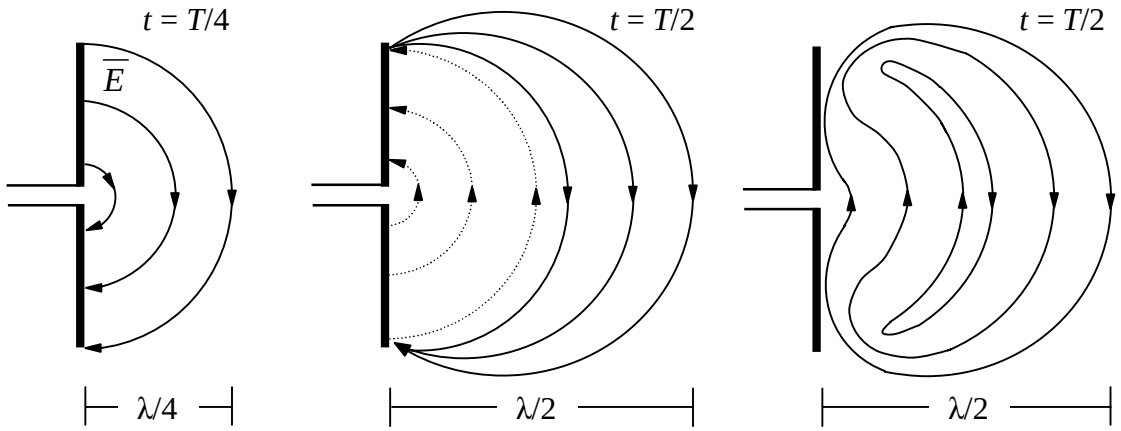

FIG. 2.6 The detachment of electric field lines for a short dipole antenna during half a period T [10].

The electric charges are required to excite the electromagnetic fields, but are not required to sustain them. After the electric field lines have detached from the antenna surface, they do exist even in the absence of the electric charges.

2.2.2 Fundamental antenna parameters

The antenna performance is described with use of various parameters. In this section, the basic antenna parameters relevant for this research work are emphasised.

Field regions

The space surrounding an antenna is divided into three regions, see Fig. 2.7: the reactive near-field, the radiating near-field (Fresnel region), and the far-field (Fraunhofer region). The boundaries separating theses areas are not unique, but several criteria exist to identify the regions.

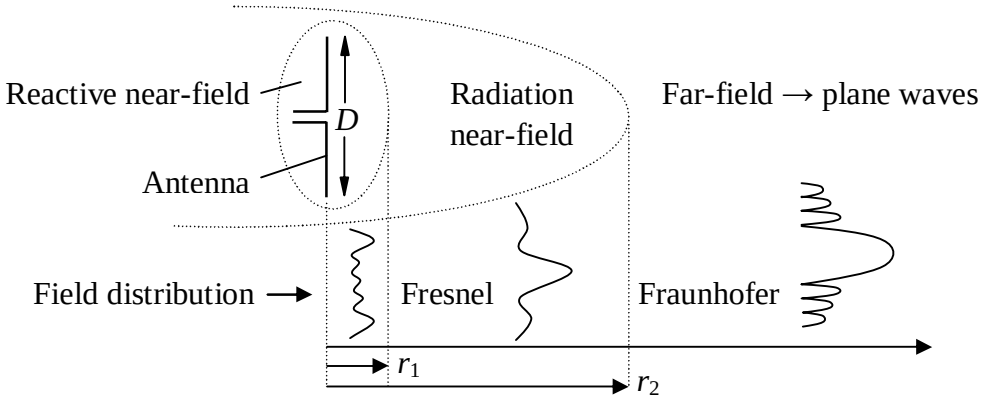

FIG. 2.7 The antenna field regions for $D > \lambda$: $r_1 = 0.62\sqrt{D^3/\lambda}$ and $r_2 = 2D^2/\lambda$ [10].

The reactive near-field is the space immediately surrounding the antenna, wherein the reactive field dominates. The outer boundary of this region is for most antennas set to $0.62\ (D^3/\lambda)^{1/2}$, where λ is the wavelength and D is the largest dimension of the antenna.

For very short dipole antennas the outer boundary is commonly set to $\lambda/(2\pi)$ from the antenna surface [8, 10].

In the radiating near-field, the radiating fields predominate and the angular field distribution is dependent on the distance from the antenna. If the antenna has a maximum overall dimension which is very small compared to the wavelength, this region may not exist [10]. The inner boundary of this region is commonly set to 0.62 $(D^3/\lambda)^{1/2}$, and the outer boundary to $2D^2/\lambda$, assuming that $D > \lambda$. This criterion is based on a maximum phase error of $\pi/8$ [10]. The phase error is the phase difference in the phase front of the spherical waves. If the phase error is zero, the spherical waves have become plane waves. A phase error of $\pi/8$ is obtained at a distance of $2D^2/\lambda$ from the source.

The far-field region is the region of the antenna field where the angular field distribution is independent of the distance from the antenna. For $D > \lambda$, this region is commonly set to start at a distance greater than $2D^2/\lambda$ from the antenna [8, 10]. In the far-field, the field components are essentially transverse. The antenna amplitude pattern shape changes when the observation distances changes because of variations of the fields, both magnitude and phase. A typical shape progresses throughout the regions is depicted in Fig. 2.7.

Polarisation

The polarisation of an antenna is the polarisation of the wave radiated by the antenna when transmitting [8, 10], refer to Section 2.1.3. The polarisation radiated by an antenna will vary with direction. Usually the polarisation characteristics remain constant over the main beam, but radiation from side lobes can differ greatly from that of the main beam. Hence, the polarisation in the beam peak direction is used to describe the antenna polarisation [8]. At each point in space, the polarisation is resolved into a pair of two orthogonal polarisations: the cross-polarisation and the co-polarisation. Co-polarisation represents the polarisation the antenna is intended to radiate (or receive, based on reciprocity), while cross-polarisation represents the polarisation orthogonal to a specified polarisation, which is usually the co-polarisation [10].

Radiation pattern

The antenna radiation pattern is graphical representation of the antenna far-field radiation properties. Usually, the spherical coordinate system centred on the antenna is used, see Fig 2.8. For an amplitude pattern of an antenna, there would in general be three electric or magnetic field components: (E_r, E_θ, E_ϕ) or (H_r, H_θ, H_ϕ) at each observation on the surface of a sphere of constant radius r. The magnitude of the total electric or magnetic field is represented by the radial distance r. In general, the magnitude of the total electric and magnetic field are

$$\left|\overline{E}\right| = \sqrt{\left|E_r\right|^2 + \left|E_\theta\right|^2 + \left|E_\phi\right|^2} \text{ and } \left|\overline{H}\right| = \sqrt{\left|H_r\right|^2 + \left|H_\theta\right|^2 + \left|H_\phi\right|^2}, \tag{2.52}$$

respectively. In the far-field, the radial E_r or H_r component is zero or vanishingly small compared to either one, or both, of the two other components [10], and the relationship between the radiation components for a *z*-directed source is [8]

$$E_\theta = \eta H_\phi, \text{ where } \eta = \sqrt{\mu/\varepsilon} \tag{2.53}$$

is the wave impedance of the medium. Thus the radiation fields are perpendicular to each to each other and to the direction of propagation *r*. The spherical waves appear to an observer in the far-field to be a plane wave, since the radius of the spherical wave is so large that the phase front in nearly planar over a local region.

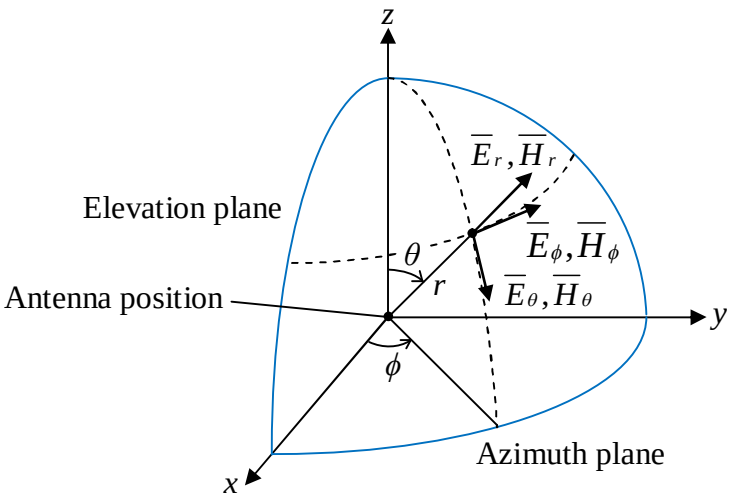

FIG. 2.8 The spherical coordinate system, where $0 < \phi < 2\pi$ and $0 < \theta < \pi$. The sphere of radius *r* is centred on the antenna.

Field pattern represents the magnitude of the electric or magnetic field as a function of angular space, while power pattern represents the square of the electric or magnetic field as a function of angular space [10]. Very often, the field and power patterns are normalised to their maximum values, yielding normalised field, $F(\theta, \phi)$, and normalised power, $P(\theta, \phi)$, patterns:

$$P(\theta,\phi) = \left|F(\theta,\phi)\right|^2. \tag{2.54}$$

Additionally, the normalised patterns are commonly plotted in decibels, yielding normalised field and power patterns in logarithmic scale. The magnitude of the field pattern and the power pattern in decibels are the same, since:

$$\begin{cases} |F(\theta,\phi)|_{\mathrm{dB}} = 20\log_{10}|F(\theta,\phi)| \\ P(\theta,\phi)_{\mathrm{dB}} = 10\log_{10}|F(\theta,\phi)|^2 = 20\log_{10}|F(\theta,\phi)| \\ \Rightarrow P(\theta,\phi)_{\mathrm{dB}} = |F(\theta,\phi)|_{\mathrm{dB}}. \end{cases} \tag{2.55}$$

For the dipole presented in Fig. 2.15, its normalised field pattern can be written as

$$F(\theta,\phi) = E_\theta / E_{\theta,max}, \tag{2.56}$$

since the *z*-directed source has only the θ-component of the electric field.

Some common radiation pattern parameters are presented in Fig. 2.9. A radiation lobe is defined as a portion of the radiation pattern bounded by regions of relatively weak radiation intensity [10]. To find were the pattern achieves its half-power relative to the maximum value of the pattern, the field pattern $|F(\theta,\phi)|$ value is set to 0.707 of its maximum, the power pattern (in linear scale) is set at its 0.5 value of its maximum, and the power pattern (in dB) is set at –3 dB value of its maximum.

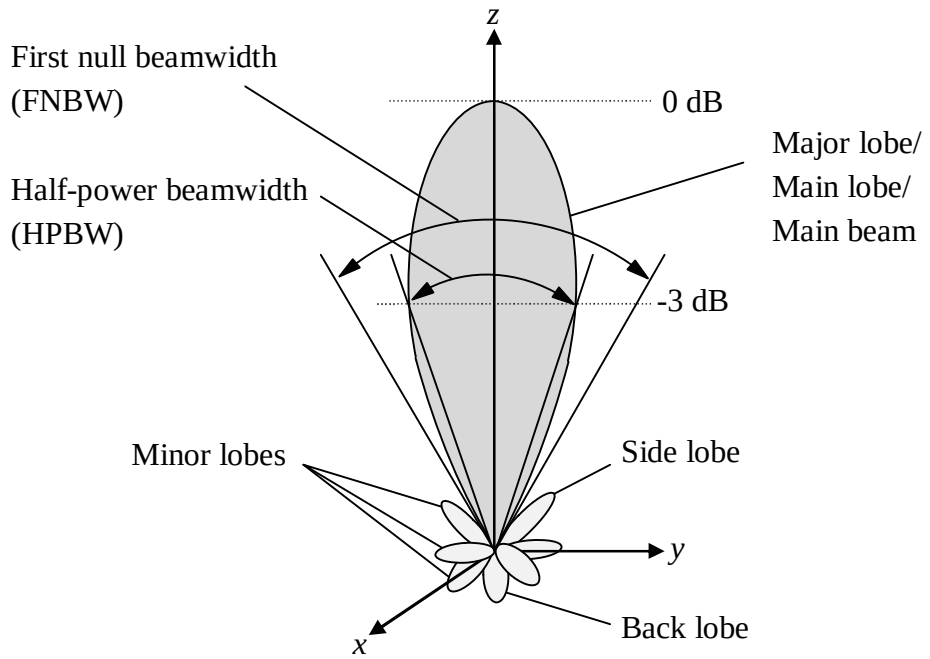

FIG. 2.9 Antenna power pattern. The major lobe contains the direction of maximum radiation; all other lobes are minor lobes. More than one major lobe is possible. [10]

An isotropic radiator is an imaginary lossless antenna that has equal radiation in all direction. It is used as a reference when considering the directional properties of an antenna. A directional antenna transmits or receives more electromagnetic waves in some direction than in others [10]. A special case of a directional pattern is the omnidirectional pattern, which has an essentially non-directional pattern in a given plane and a directional pattern in any orthogonal plane. The dipole antenna presented in section 2.2.3 is an example of an antenna having an omnidirectional radiation pattern.

In practise, the three-dimensional radiation pattern is measured as several two-dimensional patterns. For linearly polarised antennas, radiation properties are usually described in terms of principal *E*- and *H*-plane patterns. The *E*-plane is the plane parallel to the electric vector and comprises the direction of maximum radiation, and the *H*-plane comprises the magnetic vector and comprises the direction of maximum radiation [10]. The two principal planes are orthogonal to each other.

Directivity

Antenna directivity can be understood as the ability of an antenna to concentrate energy in one direction in space relative to radiation in other directions. The derivation of directivity expressions can be found in [8]. The complex power flow out through a surface *s* can be expressed using the Poynting vector $\overline{S}$ (W/m^2):

$$P_{rad} = \iint_{\partial V} \overline{S} \cdot d\bar{s}, \tag{2.57}$$

where $\bar{s} = ds \cdot \bar{n}$ and $\bar{n}$ is the unit normal to the surface directed out from the surface. The real power flowing through the surface is then

$$P_{rad} = \mathrm{Re}\left(\iint_{\partial V} \overline{S} \cdot d\bar{s} \right) = \frac{1}{2} \mathrm{Re}\left(\iint_{\partial V} \left(\overline{E} \times \overline{H^*} \right) \cdot d\bar{s} \right). \tag{2.58}$$

This is the power radiated by an antenna, and when the antenna is located in the spherical coordinate system, (2.58) becomes

$$P_{rad} = \frac{1}{2} \mathrm{Re}\left(\int_0^{2\pi} \int_0^{\pi} \left(E_\theta H_\phi^* - E_\phi H_\theta^* \right) r^2 \sin\theta \, d\theta \, d\phi \right). \tag{2.59}$$

The radiation fields have both θ and ϕ components. In the far-field, the direction of $\overline{E}$ and $\overline{H}$ are perpendicular to each other and to the direction of propagation. Additionally, the magnitudes of $\overline{E}$ and $\overline{H}$ are related through the wave impedance η:

$$\overline{H} = \frac{1}{\eta} \bar{r} \times \overline{E}, \text{ for } z\text{-directed sources}: \begin{cases} H_\phi = \dfrac{E_\theta}{\eta} \\ H_\theta = -\dfrac{E_\phi}{\eta} \end{cases}. \tag{2.60}$$

Using (2.59) and (2.60), we get

$$P_{rad} = \frac{1}{2\eta}\int_0^{2\pi}\int_0^{\pi}\left(\left|E_\theta\right|^2 + \left|E_\phi\right|^2\right) r^2 d\Omega, \text{ where } d\Omega = \sin\theta d\theta d\phi. \tag{2.61}$$

The element of solid angle $d\Omega$ (1 steradian or square radians) is range independent. This integral can be calculated for any surface enclosing the antenna, but usually a spherical surface centred in the origin is used. The element of solid angle is depicted in Fig. 2.10.

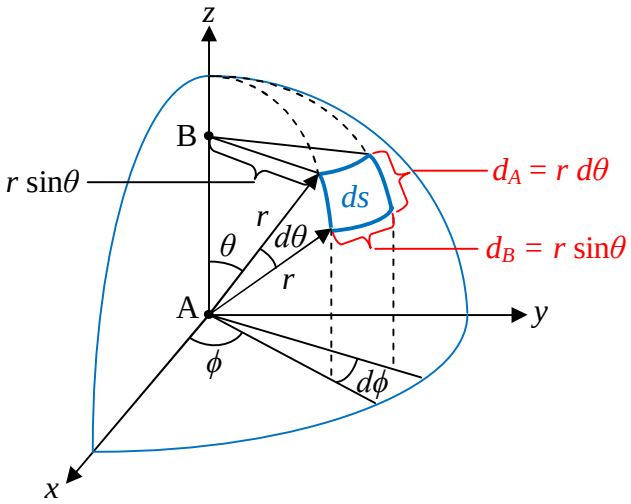

FIG. 2.10 The element of solid angle is $d\Omega = \sin\theta\, d\theta\, d\phi$, and the area $ds = r^2 \sin\theta\, d\theta\, d\phi = r^2\, d\Omega$.

The area *ds* in Fig. 2.10 can be written with use of the element of solid angle as

$$ds = r^2 \sin\theta\, d\theta\, d\phi = r^2 d\Omega. \tag{2.62}$$

Fig. 2.11 illustrates why the area *ds* can be expressed as stated in (2.62). According to the definition of radians, we can write

$$\begin{cases} \dfrac{d_A}{c_A} = \dfrac{d\theta}{2\pi} \Rightarrow d_A = c_A \dfrac{d\theta}{2\pi} = 2\pi r \dfrac{d\theta}{2\pi} = r d\theta, \\ \dfrac{d_B}{c_B} = \dfrac{d\phi}{2\pi} \Rightarrow d_B = c_B \dfrac{d\phi}{2\pi} = 2\pi\left(r\sin\theta\right)\dfrac{d\phi}{2\pi} = r\sin\theta d\phi. \end{cases} \tag{2.63}$$

Now, the area *ds* is equal to $ds = d_A \cdot d_B = r d\theta \cdot r \sin\theta d\phi$, as expressed in (2.62).

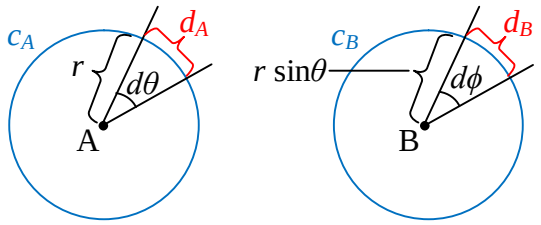

FIG. 2.11 The area ds in Fig. 2.10 is equal to the product of d_A and d_B. The circle c_A is found in the elevation plane, and the circle c_B is found in the azimuth plane.

Next, consider Fig. 2.12. The power flow through per unit solid angle in r -direction defines the radiation intensity, and it can be expressed using the Poynting vector as:

$$U(\theta,\phi)=\mathrm{Re}\,\overline{S}\,r^2\cdot\bar{r}=\left(\mathrm{Re}\,\overline{S}\cdot\bar{r}\right)r^2. \tag{2.64}$$

This expression can further be developed as

$$U(\theta,\phi)=\left(\frac{1}{2}\mathrm{Re}\left(\overline{E}\times\overline{H^*}\right)\cdot\bar{r}\right)r^2=\left(\frac{1}{2\eta}\left(\left|E_\theta\right|^2+\left|E_\phi\right|^2\right)\right)r^2=S(\theta,\phi)r^2. \tag{2.65}$$

In the far-field, the magnitudes of the radiated fields are inversely proportional to the distance, that is, the magnitudes are proportional to $1/r$. Hence, the terms $|E_\theta|^2$ and $|E_\phi|^2$ in (2.65) are proportional to $1/r^2$. As can be seen from (2.65), the radiation intensity is independent of distance r since $S(\theta, \phi)$ is proportional to $1/r^2$.

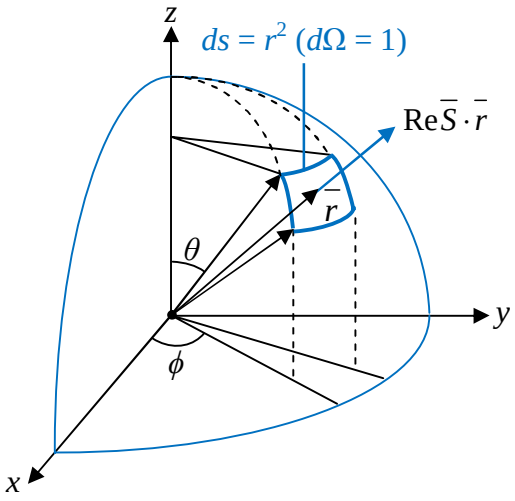

FIG. 2.12 Radiation intensity is the power radiated in a given direction per unit solid angle and it has the unit watts per steradians or square radians: $U(\theta,\phi)=\mathrm{Re}\,\overline{S}\,r^2\cdot\bar{r}$.

An alternative way of expressing radiation intensity is

$$U(\theta,\phi) = U(\theta_{max},\phi_{max})\left|F(\theta,\phi)\right|^2 = U_{max}\left|F(\theta,\phi)\right|^2, \tag{2.66}$$

where U_{max} is the maximum radiation intensity and $|F(\theta, \phi)|^2$ is the linear power pattern normalised to a maximum value of 1 in the direction (θ_{max}, ϕ_{max}). Now, the total radiated power by an antenna is obtained by integrating the radiation intensity over all angles around the antenna:

$$P_{rad} = \int_0^{2\pi}\int_0^{\pi} U(\theta,\phi)d\Omega = U_{max}\int_0^{2\pi}\int_0^{\pi}\left|F(\theta,\phi)\right|^2 d\Omega. \tag{2.67}$$

If we consider an isotropic source, which has a uniform radiation in all directions with constant radiation intensity of U_{ave} over all space, according to (2.67)

$$P_{rad} = \int_0^{2\pi}\int_0^{\pi} U_{ave}d\Omega = U_{ave}\int_0^{2\pi}\int_0^{\pi} d\Omega = U_{ave}\cdot 4\pi \tag{2.68}$$

since there are 4π sr in all space. For non-isotropic antennas, the average power per steradian can be written as

$$U_{ave} = \frac{1}{4\pi}\int_0^{2\pi}\int_0^{\pi} U(\theta,\phi)d\Omega = \frac{P_{rad}}{4\pi}. \tag{2.69}$$

This average power per steradian equals the radiation intensity $U(\theta, \phi)$ that an isotropic source would radiate with the same input power P_{rad}. Now, the directivity is the ratio of the radiation intensity in one direction to the average radiation intensity:

$$D(\theta,\phi) = \frac{U(\theta,\phi)}{U_{ave}}. \tag{2.70}$$

By dividing the numerator and denominator with r^2, the directivity is expressed using power densities:

$$D(\theta,\phi) = \frac{U(\theta,\phi)/r^2}{U_{ave}/r^2} = \frac{\frac{1}{2}\mathrm{Re}\left(\overline{E}\times\overline{H^*}\right)\cdot\overline{r}}{P_{rad}/\left(4\pi r^2\right)}. \tag{2.71}$$

If we write (2.70) with use of (2.69) we get

$$D(\theta,\phi)=\frac{U(\theta,\phi)}{\frac{1}{4\pi}\int_0^{2\pi}\int_0^{\pi}U(\theta,\phi)d\Omega}=\frac{|F(\theta,\phi)|^2}{\frac{1}{4\pi}\int_0^{2\pi}\int_0^{\pi}|F(\theta,\phi)|^2 d\Omega}=\frac{4\pi}{\Omega}|F(\theta,\phi)|^2, \tag{2.72}$$

where Ω is the beam solid angle defined as

$$\Omega=\int_0^{2\pi}\int_0^{\pi}|F(\theta,\phi)|^2 d\Omega. \tag{2.73}$$

From (2.72) we see that the directivity is solely determined by the pattern shape. Now, the total power radiated by an antenna in (2.67) can be written as

$$P_{rad}=U_{\max}\Omega. \tag{2.74}$$

The beam solid angle is the solid angle through which all the power would radiate if the power per unit solid angle (or radiation intensity) equalled the maximum value over the beam area. The figures below visualises the concept of beam solid angle.

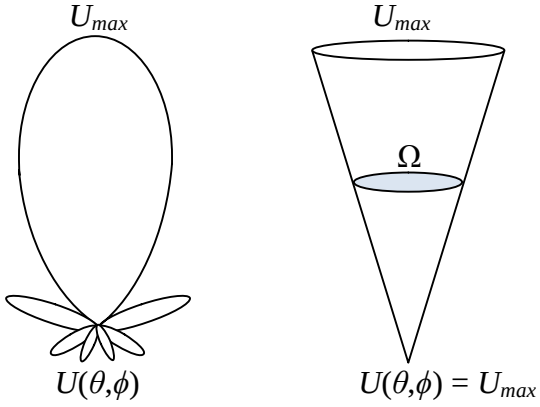

FIG. 2.13 Beam solid angle Ω. The left figure shows the radiation intensity of an actual antenna. The right figure shows the actual antenna radiation intensity, for which all radiation is concentrated into a cone of solid angle Ω. The radiation intensity is constant and equals the maximum of the actual pattern.

The maximum directivity is obtained from (2.70) as

$$D_{max}=D=\frac{U_{max}}{U_{ave}}=\frac{U_{max}}{P_{rad}/(4\pi)}=\frac{4\pi U_{max}}{P_{rad}}=\frac{4\pi U_{max}}{U_{max}\Omega}=\frac{4\pi}{\Omega}. \tag{2.75}$$

Additionally, from (2.66) and (2.70) we get

$$D(\theta,\phi)=\frac{U_{max}|F(\theta,\phi)|^2}{U_{ave}}=D|F(\theta,\phi)|^2. \tag{2.76}$$

The directivity is illustrated in Fig. 2.14.

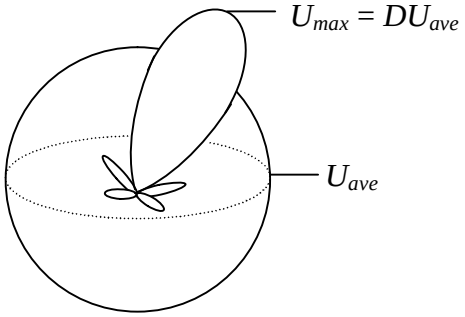

FIG. 2.14 If the radiated power was distributed isotropically over space, we would have $U_{max} = U_{ave}$ or $\Omega = 4\pi$ and $D = 1$. The radiation intensity distribution of an actual antenna has $U_{max} = DU_{ave}$ and $U_{ave} = P_{rad} / (4\pi)$.

If the radiated power P_{rad} is directed in a certain direction, the radiation intensity is increased in that direction by a factor of D compared to the radiation intensity that is obtained when the same power P_{rad} is isotropically radiated.

Gain

Power gain or simply gain is used to describe how efficient the (transmitting) antenna transforms available power at its input terminals to radiated power together with its directive properties. The gain is defined as [8]

$$G(\theta,\phi) = \frac{4\pi U(\theta,\phi)}{P_{in}}, \tag{2.77}$$

where $G(\theta, \phi)$ is the antenna gain, $U(\theta, \phi)$ is the radiation intensity of the antenna including the effect of any losses on the antenna, and P_{in} is the input power accepted by the antenna. The maximum gain is expressed as [8]

$$G = G_{\max} = \frac{4\pi U_m}{P_{in}}. \tag{2.78}$$

Antenna gain does not include the losses due to mismatches or polarisation.

Input impedance and matching

The antenna input impedance is the impedance seen into the antenna terminals with no load attached. In general form, the input impedance can be expressed as

$$Z_A = R_A + jX_A = (R_r + R_{ohmic}) + jX_A. \tag{2.79}$$

The input resistance R_A represents dissipation, which occurs is terms of radiation (R_r) and ohmic losses (R_{ohmic}). The input reactance X_A represents the power stored in the near-field of the antenna. It can be shown that maximum power transfer between the antenna and a load Z_L attached at the antenna terminals occurs when the antenna impedance and the load impedance are conjugate matched [10]:

$$Z_A = Z_L^* = \left(R_L + jX_L\right)^*, \tag{2.80}$$

where R_L is the load resistance and X_L is the load reactance. When considering the antenna transmitting mode, the generator's internal impedance constitutes the antenna load. Under conjugate match conditions, it can be shown [10] that half of the power provided by the generator is dissipated as heat in the generator internal resistance, and half of the power is delivered to the antenna. Of the power that is delivered to the antenna, part is radiated through the mechanism provided by the radiation resistance R_r and the other part is dissipated as heat by R_{ohmic}. When considering the antenna receiving mode, the incident waves impinging upon the antenna induce a voltage which is analogous to the generator voltage of the transmitting mode. Under conjugate matching, the power delivered to the antenna load is half of the captured power by the antenna, and the other half of the antenna captured power is re-radiated through R_r and dissipated as heat through R_{ohmic} [10].

The input impedance of an antenna is generally a function of frequency. Thus the antenna will be matched only within a bandwidth. In addition, the input impedance of the antenna depends on many factors including its geometry, its method of excitation, and its proximity to surrounding objects.

Radiation efficiency

From (2.75) we get that the directivity can be written as $D = 4\pi U_{max}/P_{rad}$. When comparing this to (2.78), the only difference between maximum gain and directivity is the power value used. Directivity can be understood as the gain the antenna would have if all accepted input power appeared as radiated power: $P_{in} = P_{rad}$. The antenna gain reflects the fact that some of the accepted input power is absorbed on the antenna as ohmic losses (conduction and dielectric losses), and does not appear as radiated power. The accepted input power is dissipated as radiation power P_{rad} and as ohmic losses P_{ohmic}. The ratio of P_{rad} and P_{in} is defined as the radiation efficiency e_{cd} [8]:

$$e_{cd} = \frac{P_{rad}}{P_{in}} = \frac{P_{rad}}{P_{rad} + P_{ohmic}}, 0 \le e_{cd} \le 1. \tag{2.81}$$

Using (2.74), (2.77), and (2.81) we get

$$G(\theta,\phi) = e_{cd}\,\frac{4\pi U(\theta,\phi)}{P_{rad}} = e_{cd}\,\frac{U(\theta,\phi)}{U_{ave}} = e_{cd}\;D(\theta,\phi). \tag{2.82}$$

Similarly, for maximum gain and maximum directivity we have

$$G = e_{cd}\;D. \tag{2.83}$$

This relationship is utilised when evaluating the radiation efficiency of tag antennas through measurements. Radiation efficiency in (2.81) can also be expressed with use of the antenna input resistance R_A as [8, 10]

$$e_{cd} = \frac{R_r}{R_A} = \frac{R_r}{R_r + R_{ohmic}}. \tag{2.84}$$

The total antenna efficiency e_0 takes into account losses at the antenna input terminals and within the structure of the antenna. Such losses may be due to reflections because of the mismatch between the transmission line and the antenna, and conduction and dielectric losses. In general, the overall efficiency can be written as [10]

$$e_0 = e_{cd}e_r, \text{ where } e_r = \left(1 - |\Gamma|^2\right), \tag{2.85}$$

and e_0 is the total antenna efficiency, e_{cd} is the antenna conduction and dielectric efficiency, and e_r is the reflection or mismatch efficiency. The voltage reflection coefficient at the antenna input terminals is Γ, which is expressed as

$$\Gamma = \frac{Z_A - Z_0}{Z_A + Z_0}, \tag{2.86}$$

where Z_A is the antenna input impedance and Z_0 is the characteristic impedance of the transmission line feeding the antenna.

2.2.3 The dipole antenna

The simplest dipole antenna consists of two metal conductors oriented in line with each other and with a small space between the conductors where the dipole is fed. The dipole antenna is linearly polarised and it has an omnidirectional radiation pattern, see Fig. 2.15.

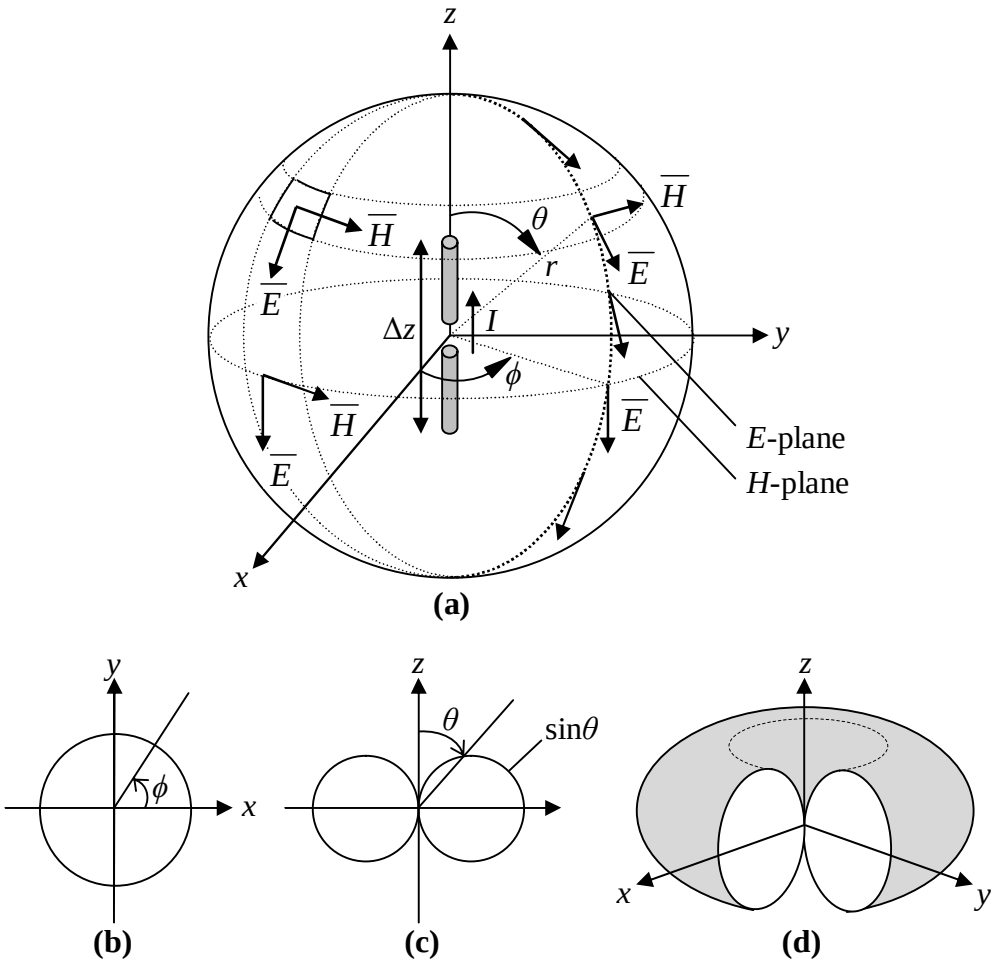

FIG. 2.15 (a) The radiated field components of an ideal dipole antenna, **(b)** *H*-plane radiation pattern of $|E_\theta|$ or $|H_\phi|$, **(c)** *E*-plane radiation pattern of $|E_\theta|$ or $|H_\phi|$, and **(d)** three-dimensional radiation pattern. [8]

The pattern has infinite number of principal *E*-planes (elevation planes, ϕ is arbitrary) and one principal *H*-plane (azimuth plane, $\theta = 90°$). The patterns are shown for an ideal dipole, which is electrically small having $\Delta z << \lambda$ and with uniform current *I* in both amplitude and phase over the radiating element extent [8]. The plotted fields are in the far-field, and hence the pattern shape is independent of the distance from the antenna. The far-field fields of the ideal dipole antenna can be written as [8]

$$\begin{cases} \overline{E} = \dfrac{I\Delta z}{4\pi}\, j\omega\mu \dfrac{e^{-j\beta\bar{r}}}{r}\sin\theta\overline{\theta} \\ \overline{H} = \dfrac{I\Delta z}{4\pi}\, j\beta \dfrac{e^{-j\beta\bar{r}}}{r}\sin\theta\overline{\phi} \end{cases}, \tag{2.87}$$

where $\omega = 2\pi f$ is and $\beta = 2\pi/\lambda$. In practise, the measurement of radiation patterns involves measurement of the electric field vector. For the dipole presented in Fig. 2.15, the co-polarisation direction in both the *E*-plane and the *H*-plane is θ, and the cross-polarisation direction in both the *E*-plane and the *H*-plane is ϕ. Hence, the principal plane patterns are measured as depicted in Fig. 2.16.

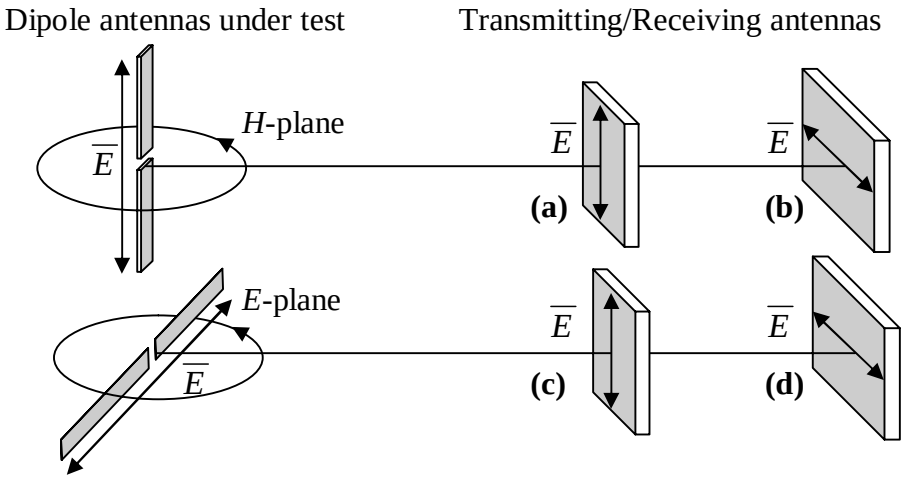

FIG. 2.16 Measurement of dipole antenna electric field pattern: **(a)** *H*-plane co-polarisation, **(b)** *H*-plane cross-polarisation, **(c)** *E*-plane cross-polarisation, and **(d)** *E*-plane co-polarisation. Ideally, the field strength is zero in the cross-polarisation planes. All antennas are linearly polarised, the direction of polarisation is indicated with electric field arrows.

Next, symmetric straight dipole antennas of arbitrary length L are discussed. The dipole antenna is surrounded by free space and oriented along the z-axis as in Fig. 2.15. The antenna is fed at the centre from a balanced two-wire transmission line, so the current on each wire are equal in magnitude and opposite in direction. Additionally, the current on the antenna is assumed to be sinusoidal. In this case, the far-field normalised electric field pattern can be written as [8]

$$E_{norm}(\theta) = \frac{\left(\cos\left(\pi k \cos(\theta)\right) - \cos(\pi k)\right)/\sin(\theta)}{\left[\left(\cos\left(\pi k \cos(\theta)\right) - \cos(\pi k)\right)/\sin(\theta)\right]_{\max}}, \tag{2.88}$$

where k is the dipole length in wavelengths. This expression will be studied in more detail in Section 3.3.1 together with the dipole antenna directivity.

The input impedance of an antenna depends on the antenna type, structure, antenna materials, and frequency. The antenna impedance is important for the transfer of power from a transmitter to the antenna or from an antenna to the receiver. As will be seen in Section 2.3, the antenna impedance is important to efficiently transfer power from the tag antenna to the integrated circuit (IC), which serves as the antenna load. For maximised power transfer, the antenna should be conjugate matched to its load. A straight dipole antenna of short length possesses capacitive reactance [8, 10], and so does the IC. Most of the antennas for UHF omnidirectional tags are commonly fabricated as modified dipoles. The design goal is to achieve the inductive input reactance required for the microchip conjugate matching. There are many types of matching techniques, among which the T-matching is utilised in Section 3.2.2.

2.2.4 Antennas in wireless communication systems

Antennas are primary used in communication links to wirelessly transfer information. A communication link showing the transmitting and receiving antennas as well as the antenna equivalent circuit model are depicted in Fig. 2.17.

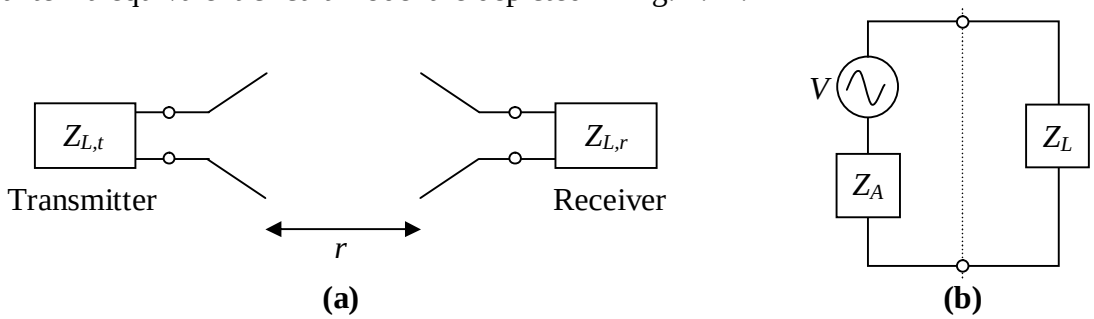

FIG. 2.17 (a) A communication link, where the transmitting and receiving antennas are connected to the loads $Z_{L,t}$ and $Z_{L,r}$, respectively, and **(b)** the equivalent circuit model of the receiving antenna of impedance Z_A connected to load impedance Z_L. The incoming electromagnetic waves induce an open circuit voltage V at the receive antenna terminals. [8]

According to the Friis free space equation, the available power received by an antenna, P_r, at a distance of r from the transmitting antenna is [8]

$$P_r = P_t G_t G_r \left(\frac{\lambda}{4\pi r} \right)^2, \tag{2.89}$$

where λ is the transmitted wavelength, P_t is power sent by the transmit antenna, G_t and G_r are the power gains of the transmit and the receive antenna, respectively. This power transmission formula assumes that the transmit antenna is conjugate matched to the source and that the receive antenna is conjugate matched to the load, that the antennas have identical polarisations, are aligned for polarisation match, and that the antennas are pointed toward each other for maximum gain. If any of the above-mentioned assumptions are not fulfilled, the power transfer between the transmitting and receiving antenna will be less than that predicted by Friis formula.

An electromagnetic wave created by the transmitting antenna propagates into space spherically from the point its creation and transports energy in the surrounding space. As the distance from the radiation source increases, this energy is divided over an increasing sphere surface area and thus the radiation power per unit area, also called the radiation density S, is decreased. In case of an isotropic transmitting antenna, the energy is radiated uniformly in all directions, and at a distance r the radiation density S can be calculated as the quotient of the transmitted power P_{EIRP} and the surface area of the sphere [11]:

$$S = \frac{P_t G_t}{4\pi r^2} = \frac{P_{EIRP}}{4\pi r^2}. \tag{2.90}$$

The power captured by the receiving antenna, or the power available for the antenna load (that is, this power would be transferred to the load under conjugate match condition), can be given with use of the maximum effective aperture [8]:

$$P_r = SA_{e,r,max}. \tag{2.91}$$

This equation indicates that a receiving antenna acts to convert incident power (flux) density in W/m^2 to power delivered to the load in watts. Losses in the antenna structure are included in $A_{e,r,max}$, while losses associated with a mismatch between polarisation of the incident wave and receiving antenna as well as impedance mismatch between the antenna and load are not included in $A_{e,r,max}$. These losses are not inherent for the antenna, but depend on how the antenna is used in the communication system. The maximum aperture can be expressed using the receiving antenna gain G_r as [8, 12]:

$$A_{e,r,max} = \frac{\lambda^2}{4\pi} G_r. \tag{2.92}$$

The effect of the impedance mismatch between the antenna and load on the effective aperture can be given as [12]

$$A_{e,r} = A_{e,r,max}\left(1 - \left|\Gamma^*\right|^2\right), \tag{2.93}$$

where Γ^* is the Kurokawa power reflection coefficient

$$\Gamma^* = \frac{Z_L - Z_A^*}{Z_L + Z_A}. \tag{2.94}$$

In the antenna receiving case, not only the power delivered to the load is of interest, but also the antenna scattering. The power scattered back from a loaded antenna can be divided into two parts. The first part is called the “structural mode” (or load independent scattering) and is due to currents induced on the antenna even if the antenna is terminated with the conjugate impedance. The structural mode scattering is similar to the scattering of general objects, and is related to the antenna structure, shape, and material. The second part is called the “antenna mode” (or load dependent scattering), which is related to the energy absorbed in the load of a lossless antenna as well as the energy re-radiated by the antenna due to the mismatch between the antenna impedance and the load impedance. Antenna mode is completely determined by the radiation characteristics of the antenna, and it vanishes when the antenna is conjugate-matched. The pattern of the energy scattered in the antenna mode is exactly that of the antenna radiation pattern. [8, 10] For most RFID tag antennas, the structural mode is small

compared to the antenna mode [13]. This work is considering RFID tag antennas, and hence the backscattered power is assumed to be only a result of the antenna mode backscattering. With other words, the backscattered power is assumed to be the power that is re-radiated ($P_{re\text{-}rad}$) through the antenna radiation resistance R_r. Now, the backscattered power $P_{re\text{-}rad}$ from the receiving antenna towards the transmitting antenna can be give as [13]:

$$P_{re-rad} = KP_rG_r, \tag{2.95}$$

where the factor K is

$$K = \frac{4R_A^2}{\left|Z_A + Z_L\right|^2}. \tag{2.96}$$

Equation (2.96) defines the effect of impedance mismatch between the antenna and load on the amount of re-radiated power. The radar cross section (RCS) σ_r of the receiving antenna is the ratio of the power backscattered by the antenna to the power density incident on it [2], and it can be given as [12, 13]

$$\sigma_r = \frac{P_{re-rad}}{S} = A_{e,r,\max}G_rK = A_{e,r,\max}G_r\left|1-\Gamma^*\right|^2. \tag{2.97}$$

In conclusion, the effective aperture and radar cross section are given in (2.93) and (2.97), respectively. The maximum value of the affective aperture is obtained when conjugate match is obtained, that is, when Γ^* is zero. If a power density of S is observed at the tag antenna, the captured and the backscattered power by the tag antenna are simply $SA_{e,r}$ and $S\sigma_r$, respectively.

For antennas in communication systems, the power values are usually referred to as equivalent isotropically radiated power (P_{EIRP}) or equivalent radiated power (P_{ERP}). P_{EIRP} is the amount of power that a theoretical isotropic antenna, which evenly distributes power in all directions, must be supplied with in order to produce the peak radiation power observed in the direction of maximum antenna gain G_t at a distance r:

$$P_{EIRP} = G_t(\text{dBi}) + P_t(\text{dBm}). \tag{2.98}$$

P_{ERP} is the amount of power that a half-wavelength dipole antenna must be supplied with in order to produce the peak radiation power observed in the direction of maximum antenna gain G_r at a distance r:

$$P_{ERP} = G_t(\text{dBd}) + P_t(\text{dBm}). \tag{2.99}$$

These power quantities can be expressed using linear values, from which the relationship between P_{EIRP} and P_{ERP} is found:

$$\begin{cases} P_{EIRP} = P_t \dfrac{G_t}{G_{iso}} = P_t \dfrac{G_t}{1} \\ P_{ERP} = P_t \dfrac{G_t}{G_{\lambda/2\text{-dipole}}} = P_t \dfrac{G_t}{1.64} \end{cases} \tag{2.100}$$

$$\Rightarrow P_{EIRP} = 1.64 P_{ERP} \Leftrightarrow P_{EIRP}(\text{dBm}) = 2.15\,\text{dB} + P_{ERP}(\text{dBm}).$$

The power limitations encountered in passive UHF RFID systems are given as equivalent isotropically radiated power or equivalent radiated power.

2.3 The passive UHF RFID system

2.3.1 Overview

UHF RFID is a rapidly developing wireless technology for identifying objects. Today, RFID is mainly found in application areas such as inventory management, asset control, and toll collection. For widespread use to become reality, much research is required to improve the performance and reliability of RFID systems. In an RFID system, objects to be identified are equipped with tags consisting of an antenna and an application specific integrated circuit. The electronic product code (EPC) is located in the memory of the ASIC, which is read by the RFID reader. In UHF RFID applications, tags primarily use electromagnetic coupling in the far field, and communication and data transfer between a tag and a reader is typically established by modulation of backscattered radiation from the tag antenna using load modulation. In an active UHF RFID system, the tag is equipped with an internal energy source, for example a battery, whereas a passive UHF RFID tag is totally dependent on the power-carrying incident wave from the reader to supply power to its chip. The read range of a passive RFID system is therefore much more limited compared to an active RFID system. [14]

RFID provides similar functions as bar code system, but has advantages in several applications: RFID tags can be read through some obstacles and are more resistant in challenging environments to dirt, etcetera. RFID systems allow multiple tags to be read in a shorter time, and tags convey more information than a typical bar code. Even though passive UFH RFID is expected to be one of the leading information technologies in the future, RFID tag performance is affected by many factors. One important field is the influence of electromagnetic properties of objects near, or in contact with, the RFID tag [14]. The tag application area determines the required tag performance and tag materials. A tag is therefore optimised to operate in a specific application environment.

The most commonly encountered RFID frequency bands are 125/134 kHz, 13.56 MHz, 860–960 MHz, and 2.4–2.45 GHz. The 125/134 kHz systems operate

within the low frequency (LF) band, 13.56 MHz systems operate in the high frequency (HF) band, and the systems at 900-MHz region and at 2.4 GHz are both within the UHF band. Often, the 2.4 GHz systems are referred to as microwave systems. In contrast to the UHF RFID systems, LF and HF RFID systems utilise inductive coupling in the near-field using the magnetic field for data transfer and communication. In these cases the read range is only up to approximately one metre, whereas the read range is longer than one metre for UHF RFID systems. The used RFID frequencies and power limits are regulated by international authorities and for each country by regional authorities. International Telecommunication Union (ITU) is the United Nations specialised agency for information and communication technologies, which globally standardises and regulates the frequency bands and power limits. In Europe, the radio communication is regulated by European Conference of Postal and Telecommunications (CEPT), and European Telecommunications Standards Institute (ETSI). In United States, the Federal Communications Commission (FCC) regulates the radio communication. In Asia and Australia, the radio communication is regulated by the Ministry of Posts and Telecommunications (MPT). For UHF RFID systems, the used frequencies bands in Europe, United States, and Japan are 865–868 MHz, 902–928 MHz, and 952–954 MHz, respectively. The EIRP limit in the European region is 3.28 W, whereas the EIRP limit in United States and Japan is 4 W. [2]

2.3.2 Components

The typical passive UHF RFID system consists of an interrogator or a reader, a transponder or a tag, and antennas to mediate between voltages and waves in air, see Fig. 2.18. The communication channel carrying information from the reader to the tag is called the forward link, and the reverse link carries information from the tag to the reader. The tags have an integrated circuit, which contains the EPC and the logic to control the protocol that guides the communication between the reader and the tag.

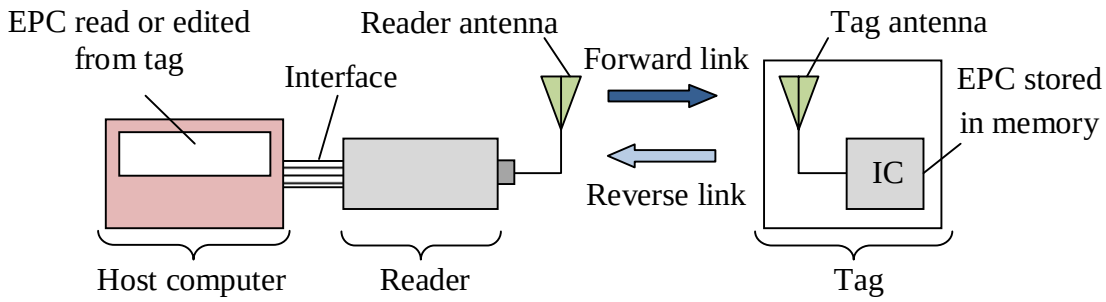

FIG. 2.18 Overview of a passive UHF RFID system.

An RFID reader is a radio transmitter and receiver that work together to communicate with the tag, and the reader is usually connected to a computer to provide an interface to the user. Additionally, the host computer stores and displays data. A circulator can be used to isolate reader receive and transmit ports when a single antenna is used for both reception and transmission. The main task of the reader is to read and to

edit the data located in the tag IC, and to provide the power to the tag. For this task the reader needs to impose the desired low frequency baseband modulation on the reader's high-frequency transmitted signal (up-conversion), and to extract it from the received signal (down-conversion) [2]. There are two basic architectures for this frequency-conversion: homodyne and heterodyne conversion. Homodyne scheme involves a direct conversion from the baseband signal to the radio frequency signal, whereas heterodyne methods use an intermediate frequency in between the carrier and the baseband frequencies [2]. Additionally, the reader must be able to correctly receive and interpret very small signals; the received backscattered signal from the tag is significantly lower than the transmitted signal. The ultimate limit on the reader sensitivity is thermal noise. In many cases the tags are forward-link limited and thus the sensitivity of the reader is less important. However, the continuous improvement in the tag IC will improve the IC sensitivity, making the reverse link more important [2]. Today, the sensitivity of the IC is in the scale of -18 dBm, and the reader sensitivity is around -80 dBm.

The passive UHF RFID tag consists of the antenna and the ASIC, see Fig. 2.19. The tag may comprise a strap, which works as a mounting for the IC. The chip is a non-linear load, and the complex impedance varies with frequency and power. The chip circuitry needs a certain minimum voltage or power to turn on. The threshold and the impedance dependence on the input power are determined by the details of the chip's radio frequency front end, and by the power consumption of the chip. The impedance dependence on the frequency is mostly determined by the chip's parasitic and packaging effects [13]. The antenna impedance is matched to the chip impedance at the minimum power level required for the chip to work, in order to maximise the tag's range [13].

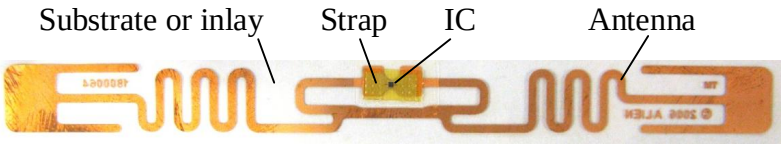

FIG. 2.19 A commercial passive UHF RFID tag (ALN-9640 Squiggle) by Alien Technology. An RFID inlay is a RFID tag inside a smart label. The antenna may also be implemented on a substrate material.

The IC memory comprises the EPC, which is used to obtain the object (that is to be identified) data from an external database. The IC comprises a demodulator, which extracts the data from the reader's modulated carrier wave. A rectifier network is also needed to generate a direct current from the alternating voltage induced on the tag antenna terminals by the carrier wave. The rectifier circuit can in its simplicity consist of a diode, which output is filtered with use of a capacitor. The direct voltage is then boosted to the IC operating voltage level with use of a charge pump [2].

2.3.3 Operating principle

This study concentrates on passive UHF RFID systems, in which the data transfer and communication between the reader and the tag is established by backscattering of electromagnetic waves [15]. The operating principle is depicted in Fig. 2.20.

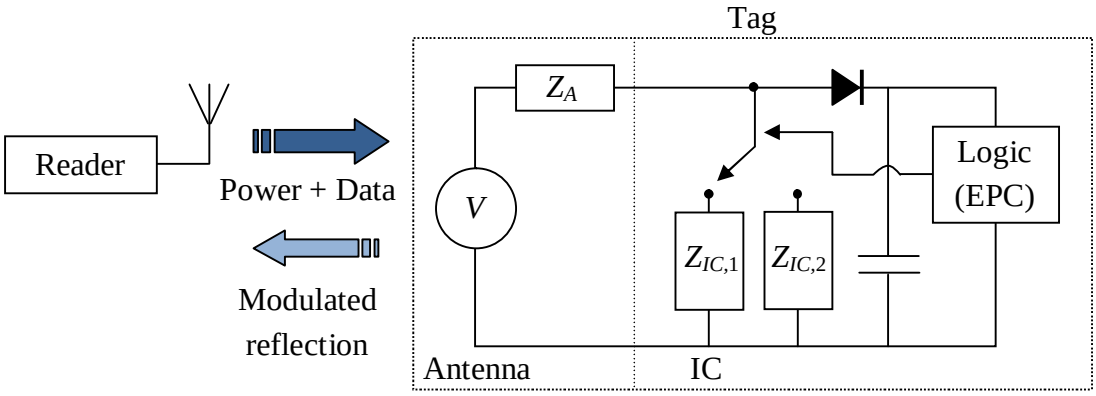

FIG. 2.20 Passive backscatter UHF RFID system. Through tag load modulation the CW is modulated according to the EPC.

Both the antenna impedance $Z_A = R_A + jX_A$ and the IC impedance $Z_{IC} = R_{IC} + jX_{IC}$ are complex. The tag antenna and IC resistances are denoted as R_A and R_{IC}, respectively, and the tag antenna and the IC reactances are denoted as X_A and X_{IC}, respectively. The forward link is established by modulating either the amplitude (Amplitude Shift Keying, ASK), or both the amplitude and phase (Phase-Reversal Amplitude Shift Keying, PR-ASK), of the reader's transmitted energy carrying carrier wave (CW). A detector on the tag is used to recover forward link data. After the tag has obtained enough energy to power up the tag IC, that is, the induced voltage V at the antenna terminals is high enough, the tag changes its input impedance between two states ($Z_{IC,1}$ and $Z_{IC,2}$) according to the EPC, and data is backscattered through the reverse link during reader's carrier wave transmission. In Fig. 2.20, the diode and capacitor produce the direct current (DC) voltage from the CW. The data exchange between the tag and the reader is depicted in Fig. 2.21.

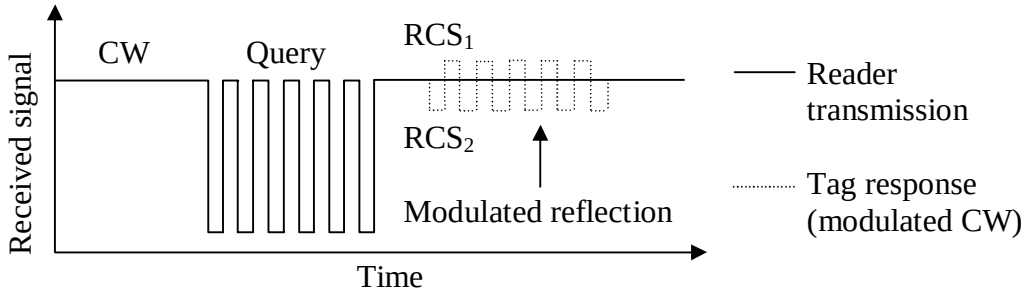

FIG. 2.21 Data exchanged between the RFID reader and tag in the time domain.

The communication between the reader and the tag is based on the tag load modulation: one of the IC impedance states is matched, that is, conjugate matched to the antenna impedance, and much of the power is delivered to the IC and the backscattered power is weak. The other impedance state is mismatched, ideally a short or open circuit, which results in that almost all power is backscattered back to the reader and little amount of power is delivered to the IC. The impedance state change is represented by the switch in Fig. 2.20, which in practise is a switched resistor or capacitor modulator [12]. The EPC determines the position of the switch. When the IC activates, it changes its input impedance according to the EPC, and the reader decodes the resulting

amplitude and phase differences in the backscattered power as binary data, that is, as the EPC. The power backscattered from the tag antenna is determined by the effect of the load modulation on the tag antenna RCS [2]. At each IC impedance state, the RFID tag presents a certain reflection coefficient Γ^* and hence, according to (2.97) a specific RCS. Usually, the two impedance states are chosen to provide a significant difference in the backscattered signal. The backscattered signal includes both amplitude and phase modulation, requiring quadrature downmixers in readers along with complex algorithms. Phase modulation occurs when the reflection coefficients Γ_1^* and Γ_2^*, associated with the load impedances $Z_{IC,1}$ and $Z_{IC,2}$, respectively, are not in phase [12]. Amplitude modulation occurs when the reflection coefficients Γ_1^* and Γ_2^* are unequal in magnitude [12]. The constant backscattered field component due to the structural mode does not depend on antenna load and has no effect on the power of the differential modulated signal received by the reader [13].

In order to convey information in the reader's transmitted signal or in the tag's backscattered signal, various modulation and encoding schemes are used. The reader in this work complies with the telecommunication protocol ISO 18000-6C (ePC Class1 Gen2 UHF RFID) [15], and uses double-sideband amplitude shift keying (DSB-ASK) modulation technique and pulse-interval encoding (PIE) format. The used tag use both phase shift keying (PSK) and ASK modulation techniques together with bi-phase phase (FM0) encoding format. A reader sends information to the tag by modulating a radio frequency carrier wave (CW) using DSB-ASK and PIE format. The tag receives its operating energy from this same modulated CW. The reader receives information from a tag by transmitting an unmodulated carrier wave and listening for a backscattered reply. The tag communicates information by backscatter modulating the amplitude and phase of the carrier using FM0 encoding format. Modulation and encoding means that the periodic CW is modulated with a low frequency encoded baseband signal. In ASK, the amplitude of the carrier oscillation is switched between two states according to the encoded baseband signal, and in PSK the binary states '0' and '1' of a code signal are converted into corresponding phase states of the carrier oscillation, in relation to a reference phase [11]. In every modulation procedure symmetric modulation products, or sidebands are generated around the carrier [11].

The PIE symbols are presented in Fig. 2.22. The high signal levels represent the transmitted CW, while the lower signal levels indicate attenuated CW. Tari is time reference interval for interrogator-to-tag signalling, and it is also the time duration of a data '0'. A data '1' is coded as a long ON pulse, which is followed by a short OFF pulse. The binary '0' is coded with a shorter ON pulse, followed by an equally long OFF pulse. The protocol ISO 18000-6c has strictly defined the values and tolerances for modulation depth, rise time, fall time, pulse width, Tari, x, and data lengths of data '1' and '0'.

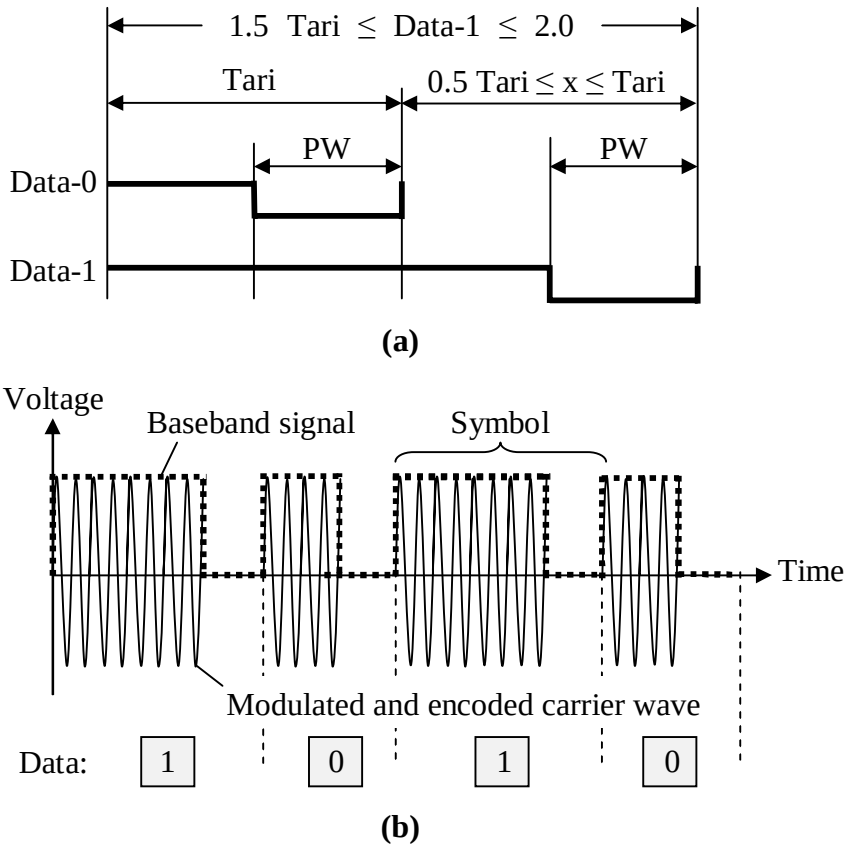

FIG. 2.22 (a) The PIE symbols, and **(b)** the ASK modulated and PIE encoded CW. [2, 16]

The FM0 symbols and sequences are presented in Fig. 2.23. A binary '1' corresponds to one signal level change, and a binary '0' corresponds to two signal level changes. At each symbol edge, the phase of the baseband is inverted. The binary '0' has an additional phase change in the middle of its duration.

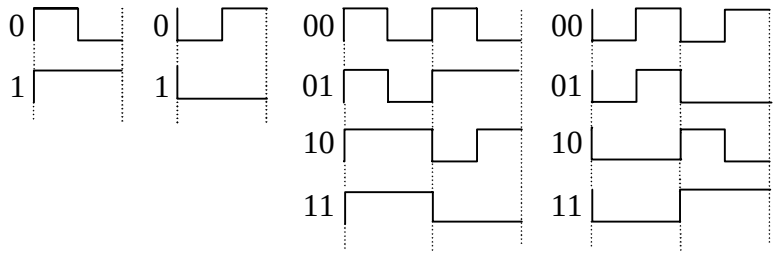

FIG. 2.23 FM0 symbols and sequences [16].

For passive tags, the encoding prior to modulation is crucial. If the CW is only digitally modulated and the data has long strands of binary '0', the tag will not get any power. Encoding ensures that the tag gets energy regardless of the transmitted data. The encoding schemes are all optimised for maximum power transfer to the tag [2].

2.3.4 Tag performance parameters

The power sent by the reader antenna is limited by local regulations. ETSI allows at maximum 3.28 W EIRP, which equals to 2 W ERP. Thus the limited available power together with the minimum power required by the IC to be in the activate mode emphasises the demand for a proper impedance matching between the tag antenna and the IC in order to maximise the power transfer. According to the Friis free space equation in (2.89), the tag antenna received power P_r is only delivered to the tag IC when maximum power transfer occurs. This happens when the tag antenna impedance Z_A is conjugate matched to its load impedance or to the IC impedance Z_{IC}:

$$Z_A = Z_{IC}^*. \tag{2.101}$$

When perfect matching is not achieved, the power delivered to the IC is less than in the conjugate matched case. The ratio of the power delivered to the IC relative to the chip available power is referred to as the power transfer coefficient τ. It can be expressed using the tag antenna and IC impedances as [2]

$$\tau = \frac{4R_A R_{IC}}{\left(\left|Z_A + Z_{IC}\right|\right)^2} = \frac{4R_A R_{IC}}{\left(R_A + R_{IC}\right)^2 + \left(X_A + X_{IC}\right)^2}, 0 \le \tau \le 1. \tag{2.102}$$

The IC sensitivity ($P_{IC,th}$) is the minimum power required for the IC to reply to the EPC Gen2 protocol's query command, during which the IC response consists of the IC identification number. This is the least power consuming task for the IC. The minimum received tag antenna power required to activate the tag, $P_{r,th}$, can be expressed using the IC sensitivity as:

$$P_{r,th} = \frac{P_{IC,th}}{\tau}. \tag{2.103}$$

By solving r from (2.89), one can see that the read range r is maximised at each frequency when the P_t, G_t, and G_r are maximised, and when P_r is minimised. The product P_tG_t = EIRP is restricted to 3.28 W by ETSI, and the minimum P_r is the tag antenna received power, which barely can activate the IC, that is, the tag antenna received power $P_{r,th}$:

$$r = \frac{\lambda}{4\pi r}\sqrt{\frac{P_t G_t G_r}{P_r}} \Rightarrow r_{\max} = \frac{\lambda}{4\pi}\sqrt{\frac{\mathrm{EIRP}\cdot G_r}{P_{r,th}}} = \frac{c}{4\pi f}\sqrt{\frac{\mathrm{EIRP}\cdot G_r \tau}{P_{IC,th}}}. \tag{2.104}$$

This maximum read range assumes that the reader and tag antennas are oriented for polarisation match and that the antennas are pointed toward each other for maximum

gain. In passive UHF RFID systems, the read range is limited by the forward link, and therefore the tag read range is the same as the forward read range [17]. The maximum read range r_{max} is one of the most important tag characteristics. Tag antenna impedance and tag antenna gain are two design parameters that can be used to enhance the read range for a certain EIRP and for a certain IC with a specific sensitivity and impedance. By tuning the tag antenna impedance equal to the conjugate of the used IC impedance, the τ is maximised. The antenna gain G_r is maximised by choosing low loss tag antenna materials and by optimising the tag antenna geometry. The term $G_r\tau$ encountered in (2.104 above) is referred to as the realised gain $G_{r,real}$, and it takes into account the achieved impedance matching:

$$G_{r,real} = \tau G_r . \tag{2.105}$$

The tag antenna normalised power pattern $P(\theta, \phi)$ is obtained by normalising $G_{r,real}$ to its maximum over the spatial angles of interest.

The radiation efficiency is one important tag antenna performance parameter, which solely describes the antenna structure losses. The tag radiation efficiency excludes losses due to impedance mismatches (reflection losses) and polarisation mismatches, and hence the radiation efficiency is independent of the achieved transmission coefficient. In general, the radiation efficiency of an antenna is expressed as $e_{cd} = P_{rad}/P_{in}$, where P_{rad} is the power radiated by the antenna and P_{in} is the accepted input power. The tag antenna is reciprocal and thus it can be considered as a transmitting antenna. The power delivered to the IC is

$$P_{IC} = P_{av,IC}\ \tau, \tag{2.106}$$

where $P_{av,IC}$ is the power available for the IC. Hence, the power available for radiation is

$$P_{av,rad} = P_{av,IC}(1-\tau) = P_{in} \tag{2.107}$$

The power radiated by the tag antenna is P_{rad}. An alternative way of expressing the radiation efficiency is found in (2.83): the tag antenna radiation efficiency is obtained as the ratio of the maximum tag antenna gain and directivity:

$$e_{cd} = \frac{G_r}{D_r}. \tag{2.108}$$

The radiation efficiency measurement method explained in Section 3 is based on (2.108).

3 RESEARCH METHOD AND MATERIAL

This section presents a novel approach to the radiation efficiency measurement of passive UHF RFID dipole tag antennas. The measurement method requires a UHF RFID measurement equipment along with a vector network analyser (VNA). A fixture is in addition needed during the VNA measurements.

3.1 Motivation and previous research work

Radiation efficiency is one of the most important tag antenna performance parameters. A high efficiency antenna has most of the accepted input power radiated away, while a low efficiency antenna has most of the power absorbed as losses within the antenna. The passive tag antenna operating principle in its application environment put great demand on high performance tag antennas: If much power is lost within the tag antenna, or due to the objects in contact or in close proximity to the tag, the tag antenna gain is decreased resulting in reduced read range.

Low loss substrates and highly conductive optimised antenna patterns inherently results in tags having excellent radiation efficiency in free space. More recently, much research work is focused on wearable RFID tag antennas for body-centric wireless communication and the design of tags for on-body use. The passive UHF RFID sewed tags included in this work are developed for wearable tag applications. Wireless monitoring of people by means of low-power and low-cost technology is nowadays considered as one of the most promising features of RFID techniques [18]. When the tag antenna comprises sensing and signal processing ability, the RFID system could provide real time bio-monitoring of temperature, blood pressure, heartbeat, glucose content and human movement in hospitals [19]. In the near future, the integration will concentrate on separate labels sewn onto a ready garment. Eventually the integration of electronics will take place already during the sewing process [20]. This new technology will provide multifunctional daily garments seamlessly integrated with wearable antennas, sensors and power harvesting devices to enable on-body wireless communication [21]. The wearable antennas should possess several features: they should be durable, lightweight, flexible, and low-profile. In addition, they should easily be integrated into clothing seamlessly and conform effectively to body surfaces [3]. This has lead to the development of new tag materials, including embroidered tags [3–6], E-textile conductors and polymer composite substrates [22]. The new tag materials used for forming the conductive antenna patterns have in many cases low conductivity. Additionally, the vicinity of the lossy human body increases the tag losses and affects the overall tag performance.

The sewed tags presented in [5–6] consist of three elements: the substrate, the antenna element, and the IC. These tags are foremost designed for wearable tag applications. Cotton fabric constitutes the substrate element, and conductive thread is used to create the conductive antenna pattern. In [5–6], the sewed tag antenna pattern is modelled as a uniform conductor layer characterised by its effective conductivity and thickness. The effective conductivity is affect by the conductivity of the thread, the sewing pattern, the sewing density, and the tag antenna design. The conductor thickness is set, and the effective conductivity is evaluated by comparison of realised gain or read range simulation results and corresponding measurement results. Even though the simulation model is a rough simplification of the complex sewed stitch pattern, it predicts the tag performance with good accuracy. Realised gain is used to describe both the losses within the tag structure and the losses introduced by mismatch between the tag antenna and the chip. Read range is affected by both these factors and in addition by the chip sensitivity. The measurement of radiation efficiency provides additional information about the losses introduced purely by the tag structure and it could hence be used to characterise tag materials which are challenging to model. Since the radiation efficiency is affected by the conductor losses, the stitch pattern, the stitch density, the antenna geometry, and the thread conductivity, these are the key factors affecting the tag antenna losses. The measurement of radiation efficiency can further be one more parameter to consider when evaluating the simulation model of complex tag structures.

Much research work has been carried out where the antenna conductive pattern is printed using conductive ink [23–24]. The measurement of radiation efficiency could give information about the printed structure losses. It is extensively studied how the amount of printed layers and the printed structure affect the read range. In addition, tag designs have been optimised for inkjet-printing, but the radiation efficiency performance in practise is less studied. Moreover, the ink tends to immerse in the substrate, which affects the tag structure losses and radiation efficiency. Other factors affecting the inkjet printed tag antenna losses are the printed structure and geometry, drop size, substrate material electrical properties, and sintering temperature and time.

As antennas become smaller in size, antenna radiation efficiency typically decreases due to reductions in the antenna radiation resistance. By intuition, the antenna tends to radiate effectively when the antenna electrical size is in the same range as the wavelength. If the radiation resistance is severally degraded due to antenna size reduction, even a small loss resistance becomes in the same order of magnitude as the radiation resistance, which is enough to ruin the radiation efficiency, refer to (2.84). In recent years, there has however been a strong interest for antenna miniaturisation. Small antennas are effectively used in passive RFID systems and body sensor applications [25]. As the user community drives for the proliferation of smaller antennas, antenna efficiency becomes even a more important parameter within the design and implementation processes. The miniaturised antennas are both geometrically and electrically small, and they can be used with or without ground plane, that is being balanced or unbalanced. In addition, the small antennas can be symmetric or

asymmetric. This applies also to passive UHD RFID tag antennas, from which most are symmetric balanced designs. Radiation efficiency becomes of great importance in the calculation of the communication link budget when the tag antenna becomes very small or when lossy materials are used to implement the tag. In particular, import parameters that characterise the tag antenna in these cases are the tag antenna input impedance, radiation efficiency, and radiation pattern [25]. Metal mountable tags tend in addition to suffer from radiation efficiency performance degradation, and the radiation efficiency measurement method could be applied in this case to characterise the encountered losses in practise when the tag operates in its real application environment.

In general, the radiation efficiency of passive UHF RFID tags is not a trivial task and it is prone to measurement errors. Even though the antenna miniaturisation in particular has brought implementations of radiation efficiency radiation measurement methods for antennas in general, less research work has been carried out for implementation of a radiation efficiency measurement method for passive UHF RFID tag antennas. To the author's best knowledge, this work proposes a novel radiation efficiency measurement method of passive UHF RFID dipole tag antennas. The measurement method is described in detail in Section 3.3.

As presented in [26], four methods have been used to measure the radiation efficiency of antennas. The first method is the pattern integration method, which is based on the direct measurement of the quantities P_{rad} and P_{in} in (2.81). The power radiated is determined by integrating the normal component of the time average Poynting vector over a closed surface surrounding the antenna, refer to (2.57). Performing a measurement for capturing and integrating all the radiated waves become very complicated and tedious. In addition, the input power, or power available for radiation, from tag antenna point of view is not straight forward to measure. Practically, the pattern integration method is not suitable for passive RFID tag antennas.
The second radiation efficiency measurement method is the Q factor method [26–27]. The Q factor is defined as [27]

$$Q = \frac{\omega \times \text{peak energy stored}}{\text{average power radiated} + \text{average power dissipated}}. \tag{3.1}$$

In this method two identical antennas are considered which are identical except that one has loss (unprimed) and the other is lossless (primed). The quality factors of the two antennas are, respectively,

$$Q = \frac{2\omega W}{R_r + R_{ohmic}} \text{ and } Q' = \frac{2\omega W'}{R_r}, \tag{3.2}$$

where W is the time average energy stored by the antenna, R_r is radiation resistance, and R_{ohmic} is the loss resistance of the antenna. If the addition of loss to the antenna is assumed to be small, then

$$\frac{P'_{rad}}{W'} = \frac{P_{rad}}{W}, \tag{3.3}$$

where P_{rad} is power radiated. The radiation efficiency is then simply

$$e_{cd} = \frac{QP_{rad}}{2\omega W} = \frac{Q}{Q'}. \tag{3.4}$$

The radiation efficiency is obtained by a measurement value for Q, and a theoretical value for Q'. The theoretical value is difficult to obtain, let alone the technique for measuring the tag antenna Q. In [10], the fractional bandwidth is linked to the Q as

$$\frac{\Delta f}{f_0} = \frac{\text{VSWR} - 1}{Q\sqrt{\text{VSWR}}}, \text{ where VSWR} = \frac{1+|\Gamma|}{1-|\Gamma|}. \tag{3.5}$$

The voltage standing wave ratio VSWR at the input terminals of the antenna is less than or equal to a desired maximum value, assuming that the VSWR is unity at the design frequency f_0. The bandwidth Δf is measured at between the frequency points at which the VSWR is equal to the desired value. Measuring the Q factor with use (3.5) put demand on one antenna resonant frequency at which the antenna is perfectly matched. In this sense, additional matching circuits may be required. In addition, the VSWR is obtained from the antenna input impedance, which is a balanced impedance in many RFID tag antenna applications. The Q factor method assumes that the losses in the antenna are small, which may not always be the case for all tag antenna materials.

The third measurement method is called the resistance comparison method [26], in which two antennas are constructed that are identical except that they are made of two different metals σ_1 and μ_1, and σ_2 and μ_2, respectively. The difference in conductivity is assumed to be small, so that $R_{r1} = R_{r2}$ and in addition it is assumed that the ohmic resistances R_{ohmic1} and R_{ohmic2} differ by a multiplicative γ. If the frequency and conductivity are high, the concept of surface resistance R_S can be used, and the γ is

$$\gamma = \frac{R_{ohmic2}}{R_{ohmic1}} = \frac{R_{S2}}{R_{S1}} = \sqrt{\frac{\mu_2\sigma_1}{\mu_1\sigma_2}}. \tag{3.6}$$

The radiation efficiency of either antenna can be determined from γ and the measured values of the input resistance $R_A = R_r + R_{ohmic}$ of the antenna. For antenna 1, the radiation efficiency is obtained as

$$e_{cd1} = \frac{R_{A2}/R_{A1} - \gamma}{1-\gamma}. \tag{3.7}$$

In this case, for each antenna under test, a second antenna needs to be fabricated. In addition, the electrical properties of each antenna materials have to be known.

The fourth method is the widely used Wheeler cap method [25–26]. The procedure for this method is to make two measurements of the input resistance of the antenna: one with the antenna isolated, $R_A = R_r + R_{ohmic}$, and a second measurement with the antenna enclosed in a highly conducting shield or cap, R_A'. The shield eliminates the radiation, and hence the resistance R_A' is the result of the losses in the antenna R_{ohmic}' and the losses in the shield R_{cap}: $R_A' = R_{ohmic}' + R_{cap}$. The antenna radiation efficiency can be calculated using [26]

$$e_{cd} = \frac{R_A - R_A'}{R_A} = \frac{R_r + \left(R_{ohmic} - R_{ohmic}' - R_{cap}\right)}{R_r + R_{ohmic}}. \tag{3.8}$$

Assuming that the losses in the shield are negligible and that $R_{ohmic}' = R_{ohmic}$, the radiation efficiency is extractable from the measured resistances R_A and R_A' as

$$e_{cd} = \frac{R_A - R_A'}{R_A} = \frac{R_r}{R_r + R_{ohmic}}. \tag{3.9}$$

This approximation assumes that $R_{ohmic} - R_{ohmic}' - R_{cap} << R_r$.

All methods except the pattern integration method assumes that the form of the current distribution on the antenna does not change when the electrical properties of the antenna or its surrounding is changed. The current distribution is assumed the same when the conducting shield is placed around the antenna. The Wheeler cap method is widely adopted due its implementation ease in practise. The method requires only two direct measurements of the antenna input resistance. As presented above, the other methods are often much more involved. The original Wheeler cap method [28] has been developed further in [29–30], in which the antenna is assumed to operate in single mode. This method is applicable for antennas on a ground plane, while for balanced antennas the feed cable represents a severe problem [25]. Hence, [25] presented a radiation efficiency measurement method based on the Wheeler cap method for measurement of balanced antenna radiation efficiency, which can be used when considering the balanced RFID tag antennas. The method is suggested to be applicable in most antenna type measurements, and in a broad frequency bandwidth. The unwanted effect of the cavity resonances on the measured scattering parameters (*S*-parameters) are eluded by proper curve fitting for the measured *S*-parameters or reflection coefficients in the Smith chart. The antennas are in addition not limited to be electrically small, and the antennas can be balanced or unbalanced, symmetric or asymmetric. In [25], the antenna input impedance is measured using the *S*-parameter method combined with the Wheeler cap method. A detailed description of the *S*-parameter method is given in Section 3.3.3, as it is applied also in this work. The reader may refer to [25] for a

detailed description of the measurement method theory. In order to determine the antenna radiation efficiency two impedance measurements are necessary: one full two-port *S*-parameter measurement of the antenna in free-space and a second of the antenna in the Wheeler cap. A fixture feeds the balanced antenna during both measurements. The measurement set-up is shown in Fig 3.1.

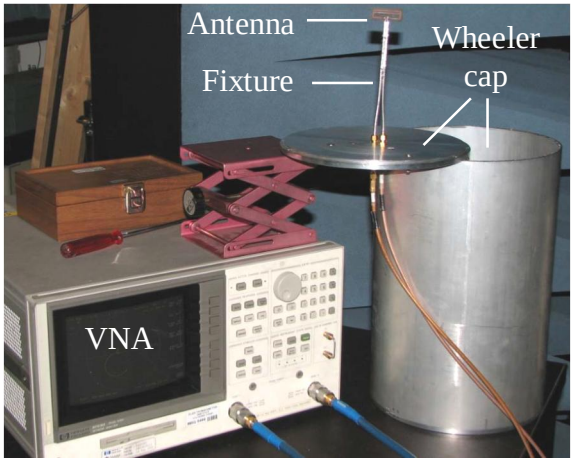

FIG. 3.1 The modified Wheeler cap method proposed by [25]. The antenna radiation efficiency is extracted from *S*-parameters recorded at two different scenarios: when the antenna is fed by the fixture in free space, and when the antenna is fed by the fixture and enclosed in the aluminium cylindrical cavity constituting the Wheeler cap.

The differential input impedance in free space and in the Wheeler cap, $Z_{d,fs}$ and $Z_{d,wc}$, respectively, are obtained as [25]

$$Z_{d,fs} = \frac{2Z_0\left(1 - S_{11}^{fs}S_{22}^{fs} + S_{12}^{fs}S_{21}^{fs} - S_{12}^{fs} - S_{21}^{fs}\right)}{\left(1 - S_{11}^{fs}\right)\left(1 - S_{22}^{fs}\right) - S_{12}^{fs}S_{21}^{fs}}, \tag{3.10}$$

$$Z_{d,wc} = \frac{2Z_0\left(1 - S_{11}^{wc}S_{22}^{wc} + S_{12}^{wc}S_{21}^{wc} - S_{12}^{wc} - S_{21}^{wc}\right)}{\left(1 - S_{11}^{wc}\right)\left(1 - S_{22}^{wc}\right) - S_{12}^{wc}S_{21}^{wc}}. \tag{3.11}$$

After this, the antenna reflection coefficients in free space Γ_{fs} and in the Wheeler cap Γ_{wc} can be extracted, and the radiation efficiency is obtained as [25]

$$e_{cd} = \left(\frac{1}{1 - \left|\Gamma_{d,fs}\right|^2}\right)\left(\frac{2}{(\Delta S_{\max})^{-1} - (\Delta S_{\min})^{-1}}\right), \tag{3.12}$$

where ΔS_{max} and ΔS_{min} are the maximum and minimum of $\Delta S = |\Gamma_{d,fs} - \Gamma_{d,wc}|$. The results presented in [25] suggest that the method works very well. However, when the radiation efficiency is to be measured in the antenna real application environment, impractically large Wheeler caps may have to be fabricated.

3.2 Tag designs

3.2.1 General considerations

The dipole tag antenna radiation efficiency measurement method is first verified by comparing measurement results and simulation results of two tag designs. One of these tag designs is optimised for good radiation efficiency performance, while the other tag design is optimised for moderate radiation efficiency. In the verification process, the simulated values are assumed to be the correct values, and measurement results deviating from the simulated results are considered as measurement errors solely. Ideally, the fabricated and assembled tags should perfectly imitate the simulated tag model, so that differences between measured and simulated values are purely due to measurement error and not due to finite fabrication accuracy or unknown tag material parameters. This also means that the simulation model for the used chip is assumed to perfectly imitate the behaviour of the real chip. These assumptions give rise to two main issues: How to find tag materials whose electrical properties are stable and accurately known, and how to find a tag antenna fabrication process possessing high accuracy. In practise, all fabrication processes and material parameters have finite accuracy, and all simulation models are simplifications of a more complex, real behaviour. By carefully choosing the tag materials, the chip simulation model, and the fabrication process, the fabricated and assembled tags are able to imitate the simulation model with good accuracy. In addition, the tag designs are kept very simple.

Rogers RT/Duroid material is chosen as substrate material since its electrical properties are stable and known with high accuracy. The antenna conductive patterns are made of etched copper. Etching process is chosen since it has good accuracy for simple tag designs that do not have narrow line widths. The antenna copper traces are in addition very thin, which favour fabrication through etching. The used chip model is presented and verified in [31]. In order to confirm that successful tag fabrication and assembling, two identical samples of the same tag design are made and measured. The tag design which has high radiation efficiency is denoted etched tag 1, and the tag design having moderate radiation efficiency is denoted etched tag 2.

After the radiation efficiency measurement method of UHF RFID dipole tag antennas is verified, it is utilised to directly measure the radiation efficiency of sewed tag antennas presented in [5–6]. Two different sewed tag designs are fabricated and assembled, denoted as sewed tag 1 and sewed tag 2. Two identical samples of the each tag design are fabricated and measured to confirm that proper fabrication and assembling is achieved.

3.2.2 Simulation and fabrication

The simulation results are presented in Section 4. Matlab is used for post-processing. This section presents the simulation set-up along with the simulation models. A short description of the tag fabrication and assembling process is given.

Simulation set-up

Ansys High Frequency Structure Simulator (HFSS) is used to design the dipole tag antennas. Etched tag 1 and 2 samples are implemented on Rogers RT/Duroid 5880 substrate using copper conductors to create the antenna conductive patterns. Sewed tag 1 and 2 samples have conductors made of a sewed pattern of conductive thread on cotton fabric. The material properties used in the simulations are gathered in Table 3.1. The simulation settings are as follows. The discrete frequency sweep is selected to 800–1000 MHz with a linear step size of 1 MHz. The number of adaptive passes is set to 15, except for sewed tag 1 design which requires 16 adaptive passes.

The conductive sewing threads typically consist of a cotton or polyester core metallised with an alloy of various metals, including silver, copper, tin and nickel. The used thread is created from two strands of conductive fibres, each having a weight of 110 dtex (1 dtex = 1 g/ 10000 m). The strand consists of 34 filaments, each having a polyamide core plated with 99% silver. The weight of silver in the thread is 55 dtex. The metallised thread has a weight of 275 dtex and it is reported to have a DC resistivity of 500 Ω/m ± 100 Ω/m. The thickness of the sewed structure on the upper face of the tag is measured and defined as the thickness of the conductive part of the antenna. The sewed antenna conductive pattern is modelled as a uniform conductor characterised with an effective conductivity determined in [5], in which the electrical properties of the cotton fabric are in addition determined.

TABLE. 3.1 Physical and electrical properties of used tag materials.

Etched tag 1 and 2	Typ.	Unit
Substrate: Rogers RT/Duroid 5880		
Relative permittivity	2.2	F/m
Loss tangent	0.0009	–
Thickness	3.175	mm
Conductor: Etched copper		
Conductivity	58	MS/m
Thickness	35	μm
Sewed tag 1 and 2	**Typ.**	**Unit**
Substrate: Cotton fabric		
Relative permittivity	1.8	F/m
Loss tangent	0.018	–
Thickness	0.25	mm
Conductor: Shieldex 110f34 dtex 2-ply HC thread		
Conductivity	4000	S/m
Thickness	0.2	mm

All tag antennas are tuned for NXP chips. The equivalent circuit model of the NXP IC on strap attached to the antenna using conductive epoxy over a 2 mm feed gap is determined and verified in [31]. The differential input impedance of the circuit model consists of a parallel connection of resistance and capacitance, see Fig. 3.2.

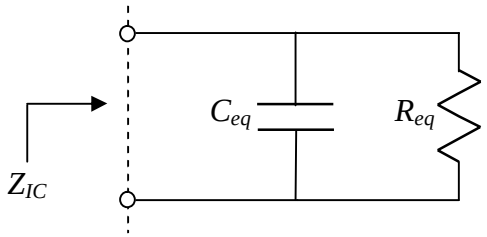

FIG. 3.2 The equivalent circuit model of the used NXP IC on the strap attached to the antenna using conductive epoxy over a 2 mm feed gap. The circuit model values are C_{eq} = 0.91 pF and R_{eq} = 2.85 kΩ.

The NXP equivalent circuit is developed at the IC wake-up power, which is assumed to be -18 dBm within the IC operating frequency range of 840–960 MHz [31–32]. The differential input impedance of the circuit model is

$$Z_{IC}(f) = \frac{Z_{Ceq} Z_{Req}}{Z_{Ceq} + Z_{Req}} = \frac{\left(\frac{1}{j2\pi f C_{eq}} R_{eq} \right)}{\left(\frac{1}{j2\pi f C_{eq}} + R_{eq} \right)} = \left(\frac{R_{eq} + j\left(-2\pi f C_{eq} R_{eq}^2\right)}{1 + \left(2\pi f C_{eq} R_{eq}\right)^2} \right). \quad (3.13)$$

In reality, the chips input impedance is dependent on both frequency and power [33].

Etched tag 1 and 2

The symmetrical etched tag 1 design is presented in Fig. 3.3. The very low loss Rogers substrate together with highly conductive conductors and a favourably geometrised tag antenna inherently results in high radiation efficiency. Hence, the etched tag 1 design required no optimisation from radiation efficiency performance point of view. The simple dipole design consists of two straight radiating arms and the feed in between. As the length of the straight dipole decreases, it becomes more capacitive [8, 10]. Hence, the straight dipole antenna length is increased until its input impedance is inductive and moderately matched to the capacitive chip impedance at the chip weak-up power within the global UHF RFID frequency band. The matching is not a crucial parameter to optimise since the radiation efficiency is independent of achieved matching between the tag antenna and the chip. However, poor matching results in reduced read range and the tag may not be readable in the used measurement set-up. To ensure that the tag will respond during the measurements, the simulated read range should be roughly above one meter.

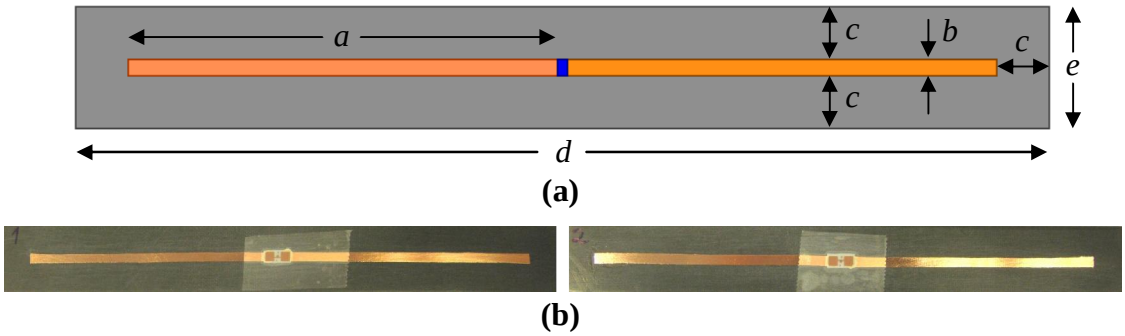

FIG. 3.3 (a) The etched tag 1 design parameters in millimetres: a = 82, b = 3, c = 10, d = 186, and e = 23. The horizontal and vertical dimensions of the blue marked feed port are 2 mm and 3 mm, respectively. **(b)** The fabricated and assembled etched tag 1 sample 1 (left) and sample 2 (right).

The symmetrical etched tag 2 design is shown in Fig. 3.4. Since the low loss Rogers substrate and highly conductive copper traces tend to result in high radiation efficiency, it is difficult to design a tag with moderate radiation efficiency. The samples with moderate radiation efficiency utilises the concept that metals close to the dipole antenna degrades the tag antenna radiation efficiency dramatically. On the other hand, other tag performance parameters are affected such as matching and radiation pattern [14]. As the radiation pattern will be used to approximate the directivity, the etched tag 2 is tuned to achieve moderate radiation efficiency, but at the same time to maintain the typical dipole radiation pattern. This tag comprises the T-matching network presented in [34], which increases the inductance of the tag antenna in order to match the capacitive chip impedance. A larger T-matching loop results in higher antenna inductance.

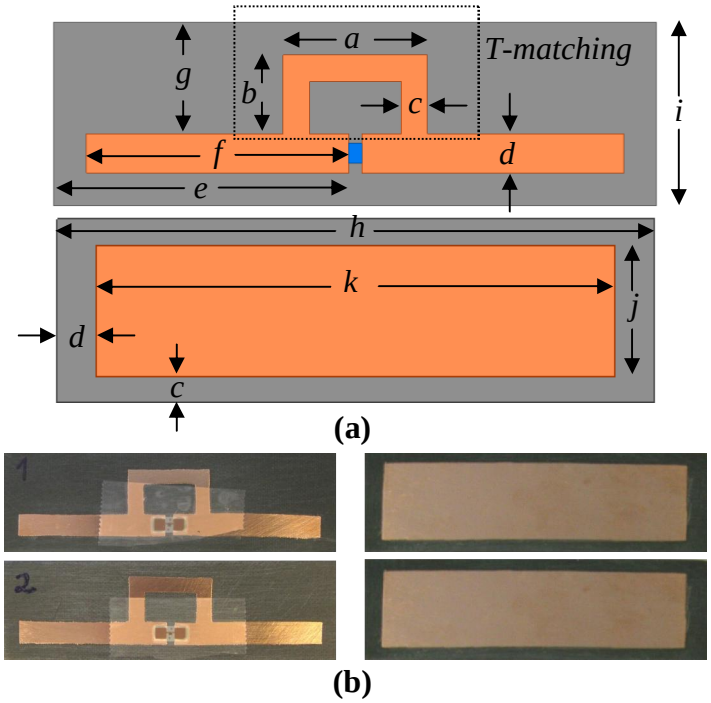

FIG. 3.4 (a) The etched tag 2 design front side (top) and back side (bottom) parameters in millimetres: a = 22, b = 12, c = 4, d = 6, e = 45, f = 40, g = 17, h = 92, i = 28, j = 20, and k = 80. The blue marked feed port is assigned in the middle of the feed gap, and its horizontal and vertical dimensions are 2 mm and 3 mm, respectively. **(b)** The fabricated and assembled etched tag 2 sample 1 (top) and sample 2 (bottom).

The available Rogers substrate has copper plating on both sides, but no photoresist. It is difficult to manually apply the photoresist on the substrate since it tends to dry non-uniformly. Hence, the conventional photolithography process is not utilised. The antenna photomask is printed out on paper and glued on top of self-adhesive book covering film. The photomask is cut out of the film, and attached on top of the Rogers substrate to protect the copper beneath from the etching liquid consisting of 80 ml tap water, 30 ml hydrochloric acid, and 30 ml hydrogen peroxides. The film is removed from the etched substrate, uncovering the copper traces forming the conductive antenna pattern. The chip on strap is glued with conductive epoxy over the antenna feed gap. The hand-made photomask result in fabrication inaccuracy, but through etching only the copper is etched away, leaving a uniform substrate. Moreover, the etched tag 1 footprint is geometrically simple and easily cut out from the film. Etched tag 2 design is more complex, and the one of the most critical factors affecting its performance is the size and alignment of the back copper plate on the substrate backside.

Sewed tag 1 and 2

The symmetrical sewed tag designs are shown in Figs. 3.5 and 3.6. The sewed tags are extensively studied in [3–6]. Both tag designs have a conductive antenna pattern with the same effective conductivity, even though sewed tag 1 design comprises a vertical stitch direction and sewed tag 2 a horizontal stitch direction. Moreover, sewed tag 1 comprises the additional T-matching network and the stitch density is not as high as for sewed tag 2. The sewed antennas are modelled as a single layer of a uniform conductive medium characterised by a height and an effective conductivity. The conductive thread is however in practise penetrating the cotton substrate to form a two layer conductive pattern with the holey substrate in between. Additionally, the sewed pattern outline dimensions can deviate up to 1 mm from the dimensions given in the simulation model.

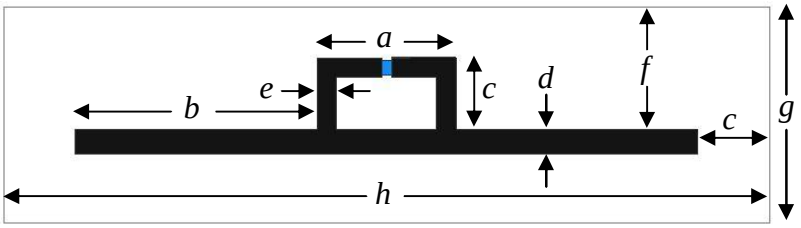

(a)

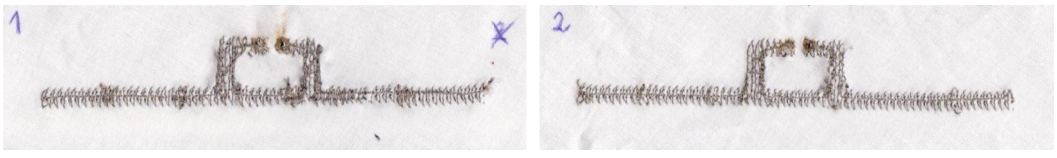

(b)

FIG. 3.5 (a) The sewed tag 1 design parameters in millimetres: a = 29, b = 50.5, c = 15, d = 5, e = 4, f = 25.5, g = 45, and h = 160. The blue marked feed port is assigned in the middle of the feed gap, and its horisontal and vertical dimensions are 2 mm and 3 mm, respectively. **(b)** The fabricated sewed tag 1 antenna sample 1 (left) and sample 2 (right).

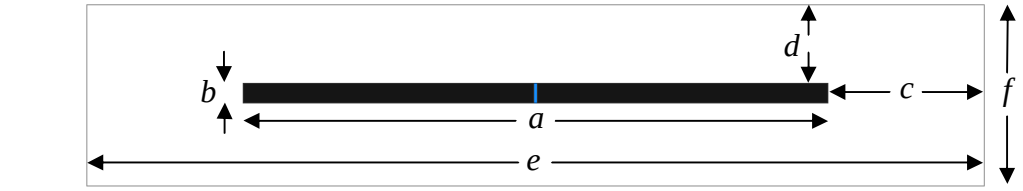

(a)

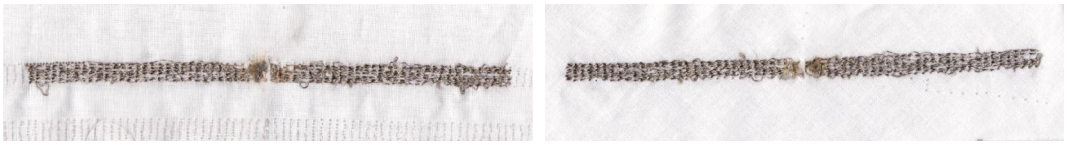

(b)

FIG. 3.6 (a) The sewed tag 2 design parameters in millimetres: a = 150, b = 5, c = 40, d = 20, e = 230, and f = 46. The blue marked feed port is assigned in the middle of the feed gap, and its horizontal and vertical dimensions are 1 mm and 5 mm, respectively. **(b)** The fabricated sewed tag 2 antenna sample 1 (left) and sample 2 (right).

The sewed tags are manufactured using the fabrication method verified in [3]. The conductive tag antenna pattern is created using conductive sewing thread. Cotton fabric layer is used as the tag antenna substrate. The tag antenna is first designed using any conventional electromagnetic structure simulator and saved as a .tiff-file. The .tiff-file is imported to the 5D™ Embroidery System software to create the desired stitch pattern and stitch density before the file is converted into an embroidery file compatible the computer aided embroidery machine. Finally, the embroidery machine automatically sews the selected embroidery pattern. The sewed tag antenna has conductive pattern on both side of the substrate. Tag IC is attached over the sewed tag antenna feed gap on the antenna top side using conductive epoxy. The sewed tag stitch pattern and density are crucial factors affecting the overall tag performance [5–6].

3.3 Antenna radiation efficiency measurement method

The radiation efficiency is obtained using (2.108). It is difficult to solely measure the antenna gain G_r since the effect of the transmission coefficient is inevitably seen on the measured tag antenna gain. In practise, the realised gain is measured. The tag antenna radiation efficiency can be extracted from (2.108) and (2.105) as

$$e_{cd} = \frac{G_{r,real}}{\tau D_r}. \tag{3.14}$$

According to (2.75), the directivity can be written with use of the beam solid angle. In this case, the directivity cannot be analytically evaluated using (2.73), since there is lack of information about the antenna pattern distribution $F(\theta, \phi)$. Hence, the directivity has to be approximated. It will be seen that the dipole tag antenna directivity can be approximated with use of the tag antenna radiation patterns. The tag antenna radiation patterns and realised gain are measurable with a UHF RFID measurement equipment.

Once the antenna input impedance is measured with use of a VNA and a fixture, the transmission coefficient is obtained from (2.102).

It should be noted that fundamentally the radiation efficiency is independent of matching or the transmission coefficient. A poor matching is gives a low realised gain and a good matching gives a high realised gain. In this way, the fraction of $G_{r,real}$ and τ remains constant and is equal to the antenna gain at each observation frequency for a specific antenna structure.

3.3.1 Approximation of directivity

Beamwidth and directivity are both measures of the antenna focusing ability. An antenna with a narrow main beam will have a high directivity, while a pattern with a wide beam will result in lower directivity. Hence, one would expect that there is a relationship between directivity and beamwidth, but in fact there is no exact relation between these two quantities. This is because beamwidth is solely dependent on the size and shape of the main beam, whereas directivity involves integration of entire radiation pattern [7]. It is possible for many different antenna patterns to have the same beamwidth, but different directivities due to differences in sidelobes or the presence of more than one main beam. However, it is possible to develop approximate relations between beamwidth and directivity that apply with reasonable accuracy to antenna type of interest. The directivity is given in (2.75). For antennas with one narrow major lobe and negligible minor lobes, the beam solid angle can be approximated as the product of the half-power beamwidths in the two principal planes [10, 35]. This approximation works well low-directivity antennas, such as for half-wavelength dipole antennas [35]. Hence, the directivity of dipole antennas can be approximated as

$$D_{r,approx,1} = \frac{4\pi}{HP_E HP_H} = \frac{4\pi}{HP_E 2\pi} = \frac{2}{HP_E}, \tag{3.15}$$

where HP_E and HP_H are the half-power beamwidths in radians in the two principal planes. To investigate the applicability of (3.15), the approximated and theoretical directivities of thin dipole antennas with sinusoidal current distribution are compared. The dipole antennas are surrounded by free space, and thus the phase velocity is that of free space. The theoretical directivities are shown in the Fig 3.7. The theoretical directivity increases with increasing dipole electrical length up to a length of approximately $5/4\lambda$, after which the directivity starts to decrease due to emerging lobes.

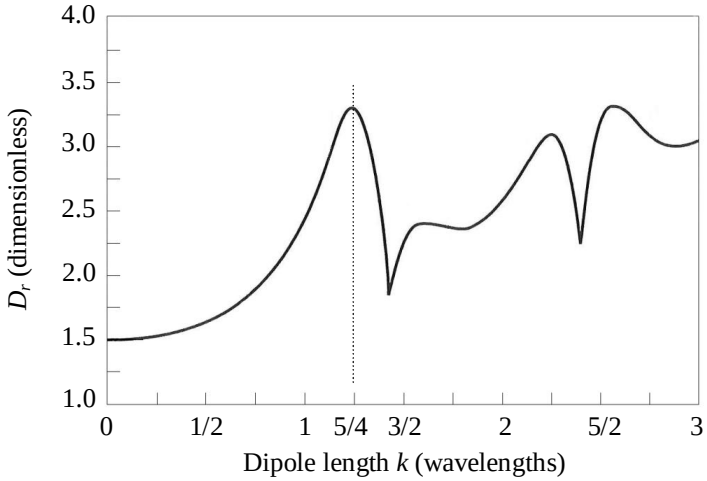

FIG. 3.7 Theoretical directivity as a function of dipole electrical length of a thin (radius of 1 μm) dipole in free space with sinusoidal current distribution. [10]

In Fig. 3.8, the far-field normalised field pattern is plotted using (2.88) for different electrical dipole lengths k.

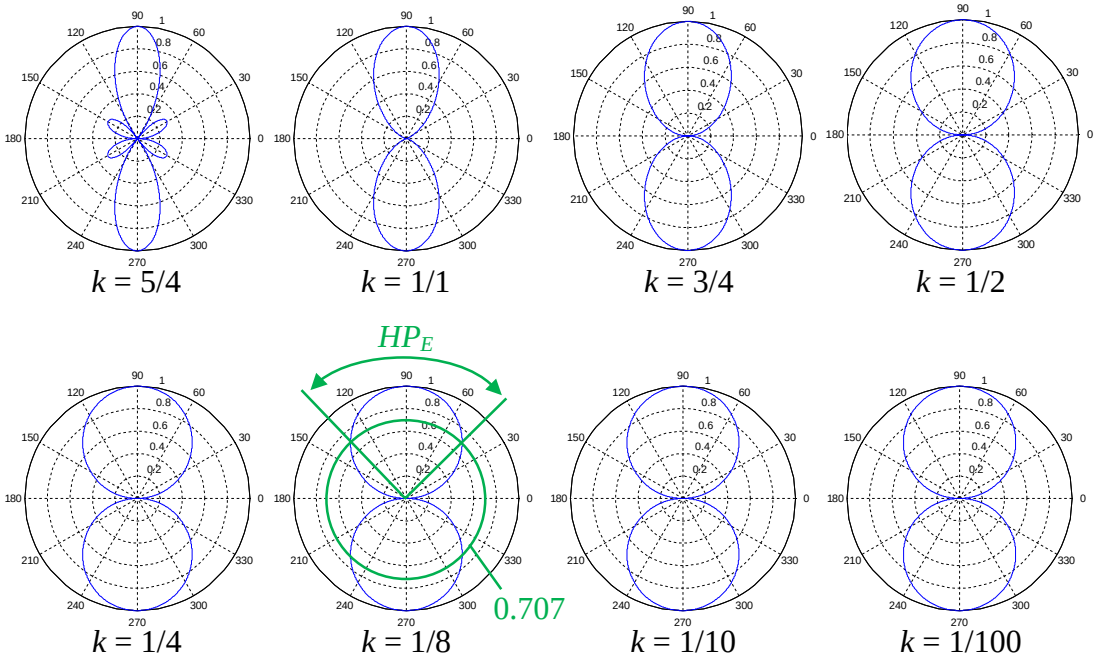

FIG. 3.8 Normalised field patterns of thin dipole antennas with sinusoidal current distribution. The antennas of electrical length $l = k\,\lambda$ are surrounded by free space. The E-plane beamwidths are read from the points were the normalised field strength has decreased from 1 to 0.707.

When the dipole electrical length increases, the dipole becomes more directive. However, when the length is greater than one wavelength, the number of lobes increases and the dipole loses its directive property. When the electrical length decreases, the dipole becomes less directive and the half-power beamwidth increases. This is in accordance with the approximation. The E-plane half-power beamwidths, HP_E, are read from the plots, and the dipole antenna directivity is approximated using (3.15).

The error percentage in the radiation efficiency due to the directivity approximation suggested in (3.15) is obtained as

$$\text{Error}(\%) = 100 \times \frac{\left| e_{cd,theo} - e_{cd,approx} \right|}{e_{cd,theo}} = 100 \times \left(\left| \frac{1}{D_{r,theo}} - \frac{1}{D_{r,approx}} \right| \right) \Big/ \left(\frac{1}{D_{r,theo}} \right), \quad (3.16)$$

where $e_{cd,theo} = G_{r,real}/(\tau \cdot D_{r,theo})$ and $e_{cd,approx} = G_{r,real}/(\tau \cdot D_{r,approx})$ are the theoretical and approximated radiation efficiencies, respectively. Table 3.2 summarises how well (3.15) approximates the dipole antenna directivity of length $l = k\,\lambda$. Theoretically, the dipole directivity approaches 1.5 when the electrical length is decreased. According to Fig. 3.8, when the dipole electrical length decreases, the beamwidth remains rather constant and as a result the approximated directivity in (3.15) only slightly decreases. Hence, the error in radiation efficiency, Error_1, is stabilised to 17–18% for short dipole antennas.

TABLE. 3.2 Directivity approximations for dipole antennas and the effect on radiation efficiency.

Dipole length k	HP_E (rad)	$D_{r,theo}$	$D_{r,approx,1}$	$D_{r,approx,2}$	Error_1 (%)	Error_2 (%)
5/4	0.56900	3.2825	3.5149	2.4923	6.6	31.7
1/1	0.83500	2.4110	2.3952	2.0574	0.66	17.2
3/4	1.1180	1.8821	1.7889	1.7780	5.2	5.85
1/2	1.3627	1.6409	1.4677	1.6105	11.8	1.89
1/4	1.5188	1.5318	1.3168	1.5255	16.3	0.413
1/8	1.5583	1.5078	1.2834	1.5061	17.5	0.113
1/10	1.5626	1.5050	1.2799	1.5040	17.6	0.0665
1/100	1.5707	1.5000	1.2733	1.5000	17.8	0.00

The directivity approximation proposed in (3.15) results in poor radiation efficiency accuracy. RFID tag antennas have in general a size of 3/4–1/8λ, and hence a new directivity approximation is iterated that gives a smaller error in the radiation efficiency especially for these dipole lengths. The new approximation assumes that $HP_H = 2\pi$ rad:

$$D_{r,approx,2} = \frac{1.88}{\sqrt{HP_E}}. \quad (3.17)$$

The effect of approximation (3.17) on the radiation efficiency is also included in Table 3.2. The error Error_2 in radiation efficiency due to the new directivity approximation is very small for short dipole antennas. For dipole antennas shorter or equal to 3λ/4, the error in the radiation efficiency is at maximum 6%. For evaluating the radiation efficiency of unknown dipole antennas, (3.17) will be used to approximate the antenna directivity. Although the theoretical model of the dipole in provides means of approximating the directivity, the practical dipole antennas are implemented on a substrate material and with finite conductor conductivity. Additionally, the dipole antenna designs can differ from the straight dipole antenna design. These factors will affect the accuracy of the approximation.

3.3.2 Measurement of realised gain and directivity

The measurements for tag realised gain and tag antenna directivity are conducted in an RFID measurement cabinet, which is a shielded and anechoic cabinet for measuring RFID tags in the far-field. The linearly polarised reader antenna is connected through a cable to the externally located circulator, which in turn is connected to the receive (RX) and transmit (TX) ports of the Tagformance lite [36] reader. A 6 dB attenuator is connected to the reader RX port to keep its receiver in the linear dynamic range [37]. The reader is the connected to a computer.

Antenna field regions are approximate and depend on the wavelength and dimension of the antenna as well as on the application. For the conducted Tagformance measurements, the distance between the reader and the tag is 45 cm. This distance is sufficient to guarantee that the tag is operating in the far-field during the measurements. The maximum dimension of the reader patch antenna housing is $D = 28$ cm, and the minimum wavelength of $\lambda = 30$ cm within the measured frequency range is obtained at the maximum measured frequency of 1 GHz. Using the far-field approximation that states that the far-field starts at a distance of $2D^2/\lambda$ from the antenna, the far-field would start at approximately 52 cm. The dimension D is in real smaller than 28 cm since the actual patch reader antenna is enclosed inside the housing. Further, the wavelength of 30 cm is the minimum wavelength, and since the tags used in this work operate below 1 GHz, the wavelength is in real longer. These observations give a shorter distance for r than 52 cm. In addition, the agreement between simulation and measurement results presented in Fig. 4.2 verify that distance of 45 cm is sufficient to guarantee that the tag is operating in the far-field during the measurements. The measurement system is shown on Fig. 3.9.

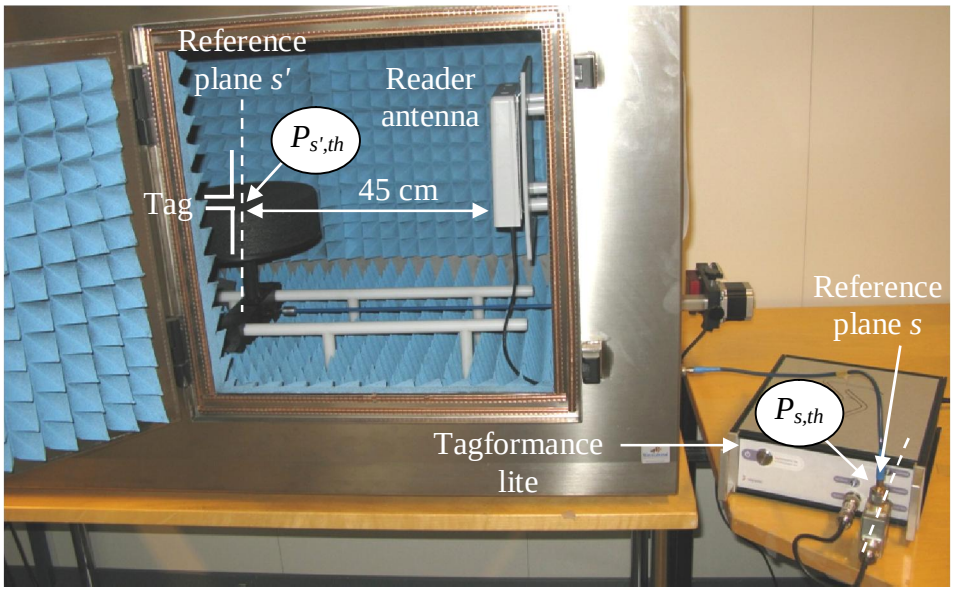

FIG. 3.9 Tagformance measurement system for measuring the tag antenna realised gain and directivity. During path loss measurement, the reference plane is shifted from s to s' with the reference antenna placed at s'. Threshold measurement measures threshold transmit power $P_{s,th}$ required to active an unknown tag under test placed at s'.

Two different types of measurements are conducted: Path loss and threshold measurement. First, the measurement system is calibrated using path loss measurement, during which the forward link transmission coefficient T_{fwd} is measured as a function of frequency between the reference planes *s* and *s′*. A known reference tag is oriented in the co-polarisation direction at the location of the reference plane *s′*, and Tagformance lite TX port is located at the location of reference plane *s*. Hence, the transmission coefficient comprises information about port matching, cable losses, reader antenna gain G_t, and free space attenuation between the reader antenna and the reference plane *s′*. The power at the reference plane *s′* required to active the reference tag IC is known and it can be obtained as

$$P_{s',th}^{ref} = T_{fwd} P_{s,th}^{ref} \Rightarrow T_{fwd} = \frac{P_{s',th}^{ref}}{P_{s,th}^{ref}}, \tag{3.18}$$

where $P_{s,th}^{ref}$ is the power at reference plane *s* required to be transmitted in order to active the reference tag IC as a function of frequency. This power is measured with the reference tag located at reference plane *s′*, and the transmission coefficient is then obtained using (3.18).

During threshold measurement, the power $P_{s,th}$ required to be transmitted at reference plane *s* as a function of frequency in order to active an unknown tag IC located at reference plane *s′* is measured. During path loss and threshold measurement, the IC is operating at its wake-up power regardless of the achieved matching conditions. From the measured T_{fwd} and $P_{s,th}$, the unknown tag performance parameters are calculable, such as theoretical read range, realised gain, and normalised power patterns. By scaling the threshold transmit power with the transmission coefficient, the threshold power at the tag can theoretically be calculated as

$$P_{s',th} = T_{fwd} P_{s,th}. \tag{3.19}$$

According to (2.103), the IC sensitivity can be expressed as

$$P_{IC,th} = \tau P_{r,th} = \tau G_r P_{s',th} = \tau G_r T_{fwd} P_{s,th}. \tag{3.20}$$

Substituting (3.20) into (2.104), the forward link theoretical read range is obtained as

$$r_{\max} = \frac{c}{4\pi f} \sqrt{\frac{\mathrm{EIRP}}{T_{fwd} P_{s,th}}}, \mathrm{EIRP} = 3.28\mathrm{W}. \tag{3.21}$$

From (3.21) it is seen that the read range is maximised when the threshold transmit power is minimised. According to (2.105) and (3.20), the tag realised gain is obtained as

$$G_{r,real} = \frac{P_{IC,th}}{T_{fwd} P_{s,th}} = \frac{P_{IC,th}}{P_{s',th}}. \tag{3.22}$$

The power patterns are calculated at a specific frequency as a function of angle. For every angle, threshold measurement is conducted. By rotating the antenna by 360°, all angles are covered for a specific polarisation and plane. In (3.22), only $G_{r,real}$ and $P_{s,th}$ depend on the measurement angle, and thus all other factors are gathered in constant k:

$$G_{r,real} = k \frac{1}{P_{s,th}}. \tag{3.23}$$

The normalised power patterns are obtained by normalising the realised gain to the minimum transmit threshold power:

$$\begin{cases} G_{r,real,norm} = \dfrac{G_{r,real}}{G_{r,real,max}} = \dfrac{k / P_{s,th}}{k / P_{s,th}^{min}} = \dfrac{P_{s,th}^{min}}{P_{s,th}} \\ G_{r,real,norm}(\text{dB}) = P_{s,th}^{min}(\text{dBm}) - P_{s,th}(\text{dBm}) \end{cases}. \tag{3.24}$$

In (3.24), the threshold transmit power $P_{s,th}$ depends on the angle. The minimum threshold transmit power $P_{s,th}^{min}$ is measured at the angle at which the realised gain has its maximum value of 0 dB. Power pattern measurement requires no system calibration.

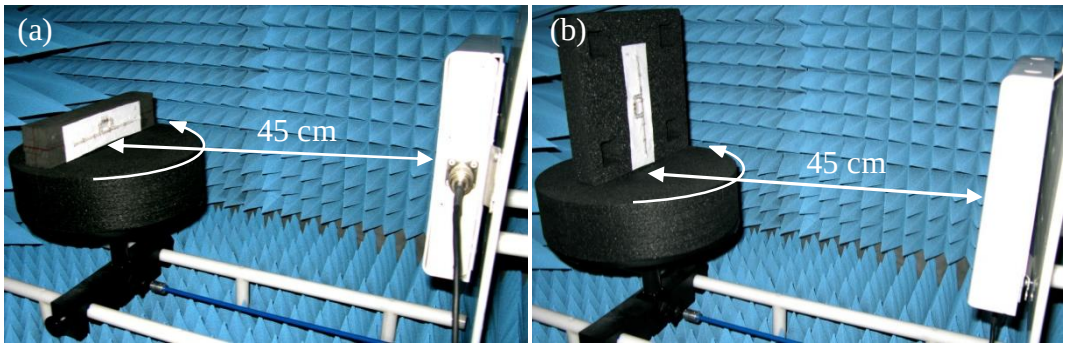

FIG. 3.10 (a) *E*-plane measurement set-up, and **(b)** *H*-plane measurement set-up. Path loss measurement is conducted for both measurement set-ups. The linearly polarised reader antenna and the linearly polarised tag antenna are aligned for polarisation match.

The tag antenna and the reader antenna alignment is shown in Fig. 3.10. For realised gain measurement the frequency range is selected to 800–1000 MHz using a step size of 0.5 MHz and a power step of 0.1 dB. The power patterns are measured at discrete frequency points with an angle step of 5° and with a power step of 0.1 dB. In conclusion, the realised gain will be calculated using (3.22), the read range will be calculated using (3.21), and the power patterns are calculated using (3.24). (3.17) is used to estimate the directivity using the measured power pattern beamwidths.

3.3.3 Measurement of transmission coefficient

When the antenna and the IC input impedances are known, the transmission coefficient is obtained from (2.102). The majority of RFID tag antennas are balanced, and their input impedances are not directly measureable with a measurement equipment that is terminated with unbalanced ports. An example of an instrument having unbalanced coaxial ports is the VNA, which is commonly used for measuring the *S*-parameters of radiofrequency circuits. Balanced circuits require a ground halfway between the terminals, and the ground usually carries no signal current, whereas unbalanced circuits use ground as return path for signal current [38]. If a balanced antenna is fed by an unbalanced port, the currents to the antenna two radiators are unequal, giving incorrect input impedance of the antenna. Commonly used methods for measuring the balanced antenna impedance include the use of a balun [39–40], the forming of a large ground plane and using the image theory [19, 40–41], and as suggested in [39–40, 42–47], the antenna input impedance can be measured with the *S*-parameter method. This technique can be utilised for both symmetrical and asymmetrical antennas, whereas the image theory is applicable only for symmetrical balanced antennas. In this work, the *S*-parameter method is utilised using the Agilent E8358A PNA Series Network Analyser.

The differential antenna input impedance is calculated from the measured scattering parameters. In Fig. 3.11, the asymmetrical dipole antenna with two arms of different length is excited differentially.

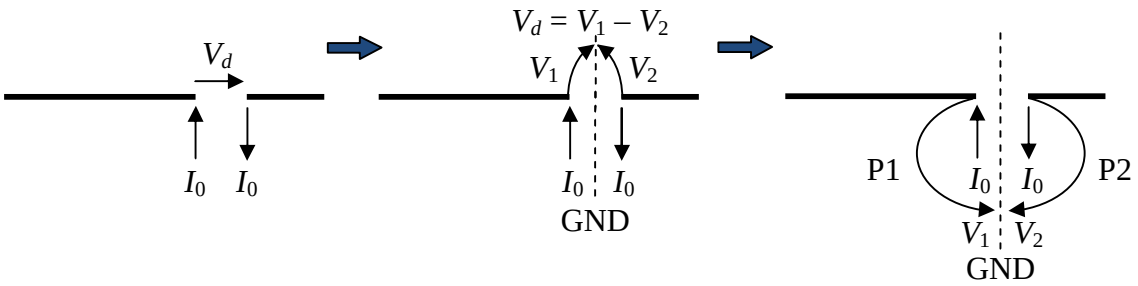

FIG. 3.11 The asymmetrical balanced dipole antenna is excited differentially with voltage V_d. The excitation voltage can be split into voltages V_1 and V_2 with a virtual ground, and thus the antenna can be considered as a two-port network whose differential impedance is related to the network parameters [42–43].

The positive and negative ports of the source with voltage V_d are connected to the antenna input terminals. The source voltage can be split into voltages V_1 and V_2 with a virtual ground, without disturbing the current distribution on the antenna. Hence, each terminal on the antenna and the virtual ground plane can be considered as a port, and the antenna itself can be considered as a two-port network, see Fig. 3.12. The differential input impedance of the antenna is related to the network parameters of the equivalent two-port network. The *S*-parameters are measurable with the VNA.

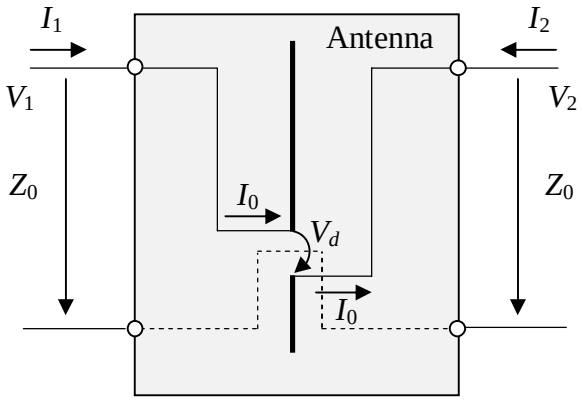

FIG. 3.12 The asymmetrical balanced dipole antenna can be considered as a two-port network, whose differential input impedance is extracted from the network parameters [42–43].

Using the antenna equivalent two-port network in Fig. 3.12, the differential impedance of the antenna can be written as

$$Z_d = \frac{V_d}{I_0} = \frac{V_1 - V_2}{I_0}. \tag{3.25}$$

The *Z*-parameters relate port current and voltage as

$$\begin{cases} V_1 = Z_{11} I_1 + Z_{12} I_2 \\ V_2 = Z_{21} I_1 + Z_{22} I_2 \end{cases}. \tag{3.26}$$

Now we have that $I_1 = I_0$ and $I_2 = -I_0$, and hence the differential voltage is

$$V_d = V_1 - V_2 = \left(Z_{11} - Z_{12} - Z_{21} + Z_{22}\right) I_0, \tag{3.27}$$

and the differential impedance is

$$Z_d = Z_{11} - Z_{12} - Z_{21} + Z_{22}. \tag{3.28}$$

Next, the *Z*-parameters in (3.28) are converted to the corresponding *S*-parameters for port characteristic impedance of $Z_0 = 50\ \Omega$ using

$$\begin{cases} Z_{11} = \left(\left(1 + S_{11}\right)\left(1 - S_{22}\right) + S_{12} S_{21}\right) / \Delta S \\ Z_{12} = 2 S_{12} / \Delta S \\ Z_{21} = 2 S_{21} / \Delta S \\ Z_{22} = \left(\left(1 - S_{11}\right)\left(1 + S_{22}\right) + S_{12} S_{21}\right) / \Delta S \end{cases}, \tag{3.29}$$

where $\Delta S = ((1 - S_{11})(1 - S_{22}) - S_{12}S_{21})/Z_0$. We get

$$Z_d = \frac{2Z_0\left(1 - S_{11}S_{22} + S_{12}S_{21} - S_{12} - S_{21}\right)}{\left(1 - S_{11}\right)\left(1 - S_{22}\right) - S_{12}S_{21}}. \tag{3.30}$$

The VNA cables are connected to the antenna using a fixture, and the *S*-parameters are recorded. The antenna impedance is obtained using (3.30), and the chip impedance is obtained from (3.13). The transmission coefficient is finally calculated using (2.102).

Two fixtures are fabricated using semi-rigid 50-Ω coaxial cable with an outer and an inner diameter of 3.5 mm and 1.0 mm, respectively. The coaxial cables are soldered together at their outer conductors to provide a common ground. One end of the fixture has two male SubMiniature version A (SMA) connectors [48] that are connected to female-female SMA connectors in order to fit to the VNA male connectors. The other end of the fixture is open with short extensions of the inner conductors. The measurement configuration is depicted in Fig. 3.13. The following VNA settings are used: frequency range 800–1000 MHz, RF power 10 dBm, averaging factor 16, and 201 measurement points. A full two-port calibration using an electronic calibration module is conducted, which locates the reference plane at the end of the VNA connectors. The fixture is connected to the VNA connectors, and in order to eliminate the introduced phase and loss by the fixture and the female-female SMA connectors, the port-extension technique of the VNA is utilised to mathematically move the calibration plane to the fixture tips.

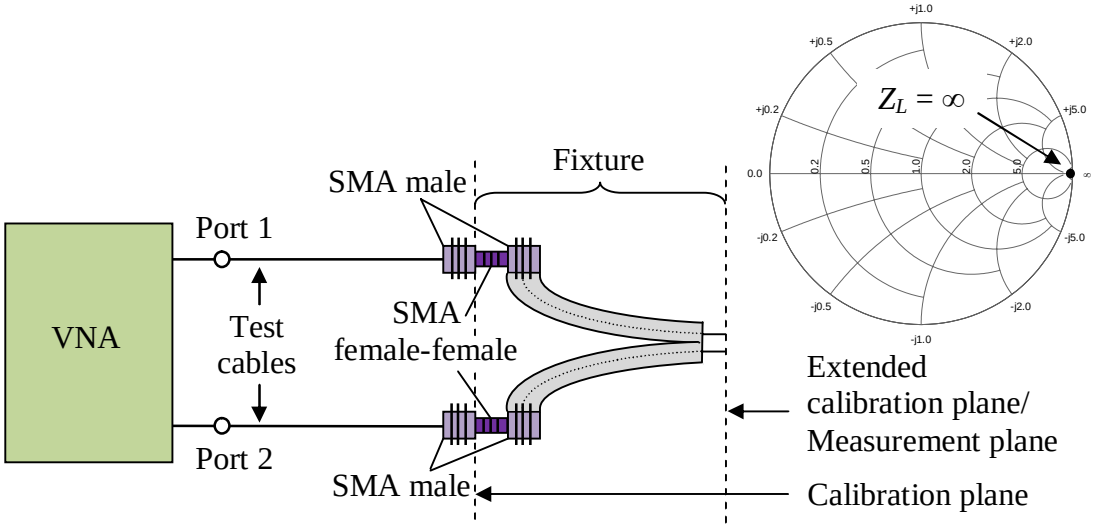

FIG. 3.13 The balanced dipole antenna impedance is measured with a VNA and a fixture. The port extension technique of the VNA is utilised to extend the calibration plane to the fixture tips. The measured impedance of an open-end fixture after calibrations is an open circuit or an infinite load.

Automatic port extensions can be performed with a shorted or an open-ended fixture. In this work, open-end fixture is selected for simplicity. Prior to port extensions, the measured S_{11} or S_{22} shows multiple turns on the Smith chart. The response is dependent on the fixture length and selected frequency range. After port extensions are conducted, the response trace is concentred on the most right side of the Smith chart

where $Z_L = \infty$, indicating that the open-end fixture is calibrated properly at the end of the fixture tips and that the frequency dependent phase delay and loss introduced by the fixture is successfully eliminated from the measurement set-up. After the calibration procedure, the antenna is soldered to the fixture tips and the *S*-parameters are recorded.

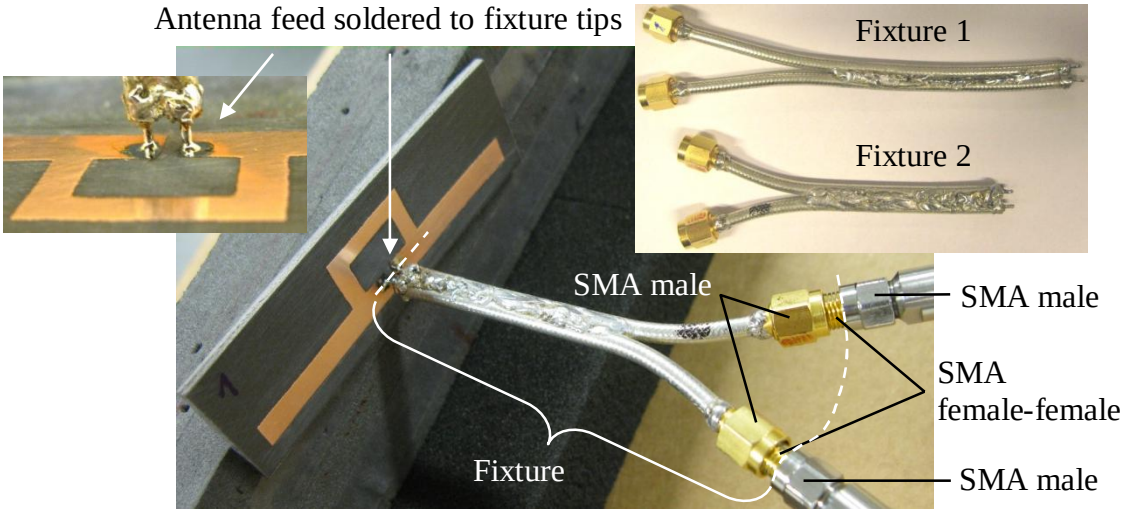

FIG. 3.14 Once the VNA measurement set-up is calibrated, the antenna under test is soldered to the fixture tips and the *S*-parameters are recorded, from which the antenna input impedance is calculated.

The fixtures and the measurement set-up are shown in Fig. 3.14. The full two-port calibration is conducted once each time a new set of measurements are started. The antennas measured at the same measurement occasion are measured with one fixture at a time, for which the port extensions are conducted prior to actual measurements. Table 3.3 summarises the port extension results.

TABLE. 3.3 Automatic port extension results.

	Port 1		Port 2	
Antennas under test	Phase delay (mm/ps)	Loss @ 850/950 MHz (mdB)	Phase delay (mm/ps)	Loss @ 850/950MHz (mdB)
Fixture 1				
Etched tag 1 samples	170.034/567.174	26.584/25.372	170.872/569.96	33.874/26.050
Sewed tag samples 1	170.052/567.232	79.481/77.529	171.007/570.417	57.754/56.035
Sewed tag samples 2 Etched tag 2 samples	169.918/566.786	84.754/79.785	171.093/570.704	83.351/83.535
Fixture 2				
Etched tag 1 samples	130.115/434.016	28.144/23.657	130.747/436.124	27.214/24.269
Sewed tag sample 1	130.101/433.970	80.585/71.540	130.831/436.404	52.965/56.482
Sewed tag samples 2 Etched tag 2 samples	130.053/433.811	59.221/54.472	130.776/436.222	41.013/42.547

4 RESULTS AND DISCUSSION

4.1 Verification of measurement method

In this section the radiation efficiency measurement method of passive UHF RFID dipole tag antennas is verified through measurements of the etched tag samples. The measurement results are compared against the corresponding simulated results. The radiation efficiency will be evaluated at discrete frequency points since the approximated directivity is available only at the discrete frequency points at which the power patterns are measured. The chip sensitivity is reported to be valid within the frequency range 840–960 MHz. Hence, the radiation efficiency is evaluated and verified at the outer frequency points of this frequency band. The third frequency point chosen is the simulated optimum performance frequency with respect to range characteristics. At this frequency, the read range reaches its maximum value.

4.1.1 Etched tag 1 design

The results for the etched tag 1 design are presented in this section. The simulated results for radiation efficiency and directivity are presented in Fig. 4.1. The tag design has ideal radiation performance characteristics. The radiation efficiency is simulated to 99.9%. The directivity is approximately 1.68 throughout the considered frequency band of 840–960 MHz. This suggests that the radiation pattern remains almost constant throughout the considered frequency band, since the directivity is solely dependent on the radiation pattern shape.

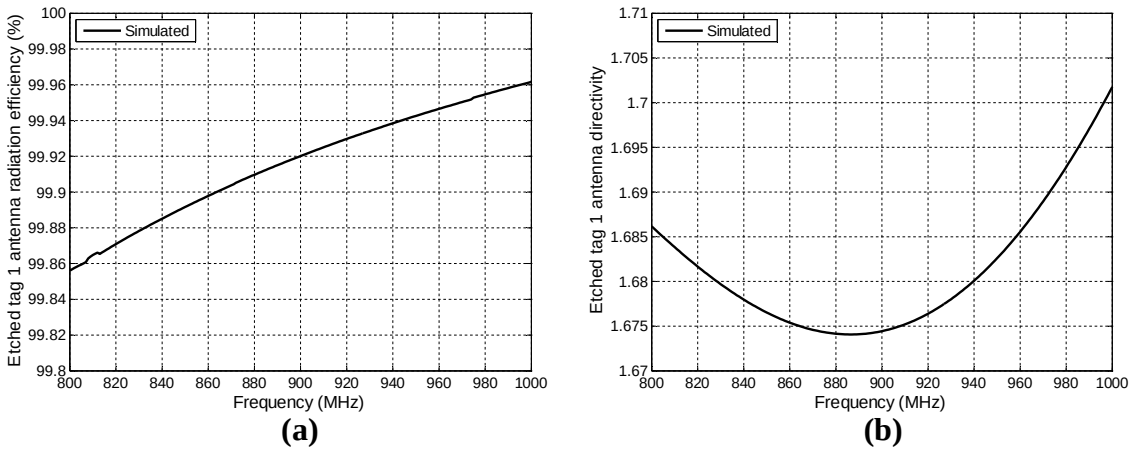

FIG. 4.1 Simulated **(a)** radiation efficiency and **(b)** directivity of etched tag 1 antenna. The antenna possesses optimised for high radiation efficiency.

The measured and simulated results for realised gain and range are shown in Fig. 4.2. The tags have good read range performance, achieving almost a peak read of 9 m. The two tag samples operate in similar manner, and the simulation model predicts very well the fabricated and the assembled tag measured realised gain and read range. The optimum performance frequency with respect to read range is at 890 MHz. Based on these results, the etched tag 1 samples are applicable for verifying the radiation measurement method.

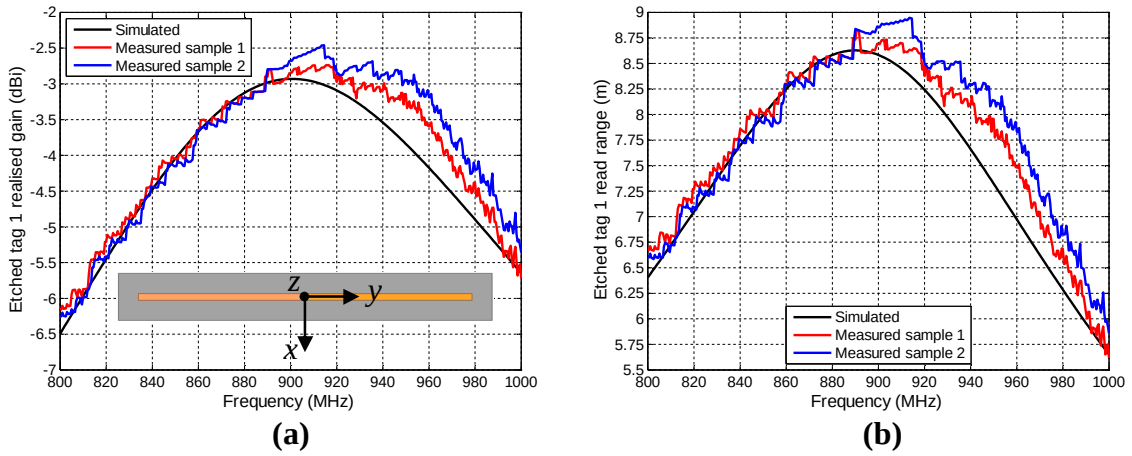

FIG. 4.2 Simulated and measured **(a)** realised gain and **(b)** read range of etched tag 1 samples. The results are recorded from *z* direction. Very good agreement is observed between measurement and simulation results. The performance of the two tag samples is similar.

The power patterns shown in Figs. 4.3 and 4.4 are plotted in decibel scale and each pattern is normalised to its own maximum realised gain value. The selected format enables direct comparison of measured and simulated pattern shape, which is of highest interest since the directivity is only based on the pattern shape. In addition, beamwidth readings from the plots become very easy. For etched tag 1 design, the frequency points selected for radiation efficiency evaluation are 840 MHz, 890 MHz, and 960 MHz. From the measured and simulated power patterns is observed that the pattern shape is barely changed at the considered frequency points, which is supported by the simulated directivity as explained above. In addition, the simulated and measured pattern shapes are in good agreement. The simulated and measured half-power beamwidths are almost equal, resulting in almost equal approximated directivities. However, as can be seen from Figs. 4.3 and 4.4, minor pattern differences are encountered between the measured and simulated results, which in practise result in directivity differences.

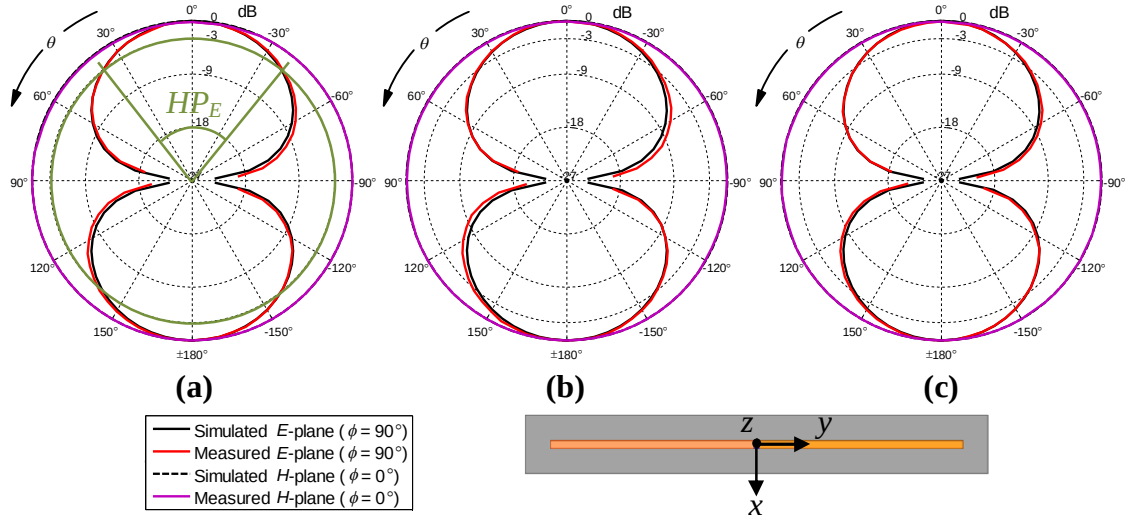

FIG. 4.3 Simulated and measured normalised realised gain for etched tag 1 sample 1 at **(a)** 840 MHz, **(b)** 890 MHz, and **(c)** 960 MHz. The simulated and measured results agree very well. The -3 dB *E*-plane beamwidths are used to approximate the tag antenna directivity, as shown in (a).

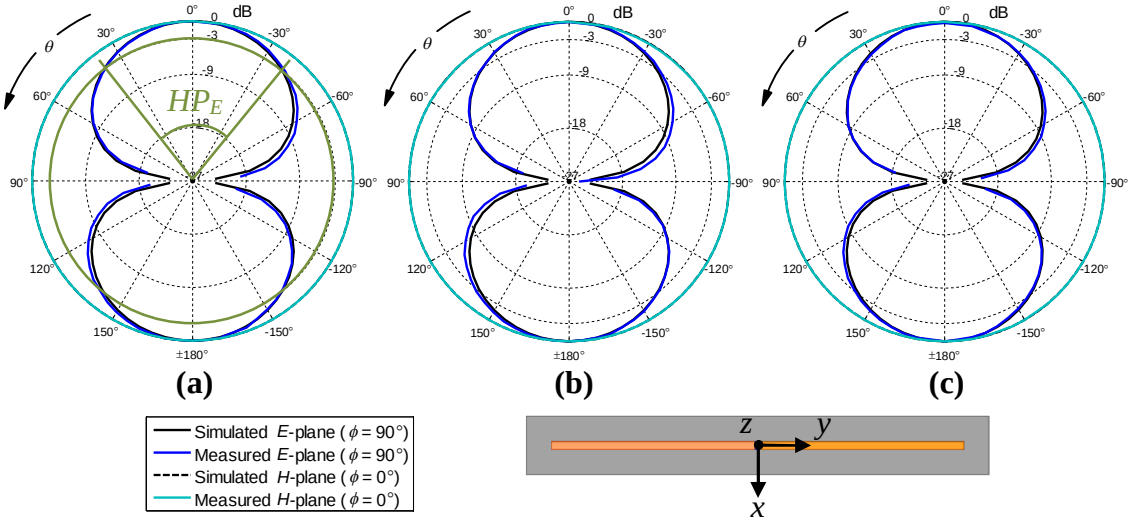

FIG. 4.4 Simulated and measured normalised realised gain for etched tag 1 sample 2 at **(a)** 840 MHz, **(b)** 890 MHz, and **(c)** 960 MHz. The simulated and measured results agree very well. The -3 dB *E*-plane beamwidths are used to approximate the tag antenna directivity, as shown in (a).

The impedance measurement and simulation results are presented in Fig. 4.5. The IC model impedance is verified through measurements in [31], and its frequency behaviour is plotted in Fig. 4.5 (a). The chip differential input impedance is capacitive. The measured antenna resistance and reactance are in good agreement with the simulated results, and the measured results suggest correctly inductive antenna impedance. The small fluctuations encountered in the measured curves are most probably due to reflections from non-perfect calibration. These fluctuations however affect the calculated transmission coefficient, which explains the differences between the measured and the simulated transmission coefficient at single frequency points. It should be kept in mind that both the simulated and measured transmission coefficients are calculated based on the very same chip model, and that the differences between measured and simulated results are hence purely due to the accuracy of the impedance

measurement method. Ideally, all antenna measured curves in the graphs should be the same, indicating that the antenna impedance is independent of the fabrication process and of the fabricated fixture. The differences could be due to the soldering of the fixture tips to the antenna feed and due to that the port extensions are not that accurate since non-standard calibration standards are used. For example, the port extensions are conducted for an open calibration standard by leaving the fixture tips open. At radio frequencies, the open-end fixture practically never behaves as an ideal open load, but shows slightly capacitive behaviour. This might reduce the accuracy of the port extension calibration. Moreover, the fixture itself is directly attached to the antenna under test, and its presence most likely affect the measured impedance. The proximity of a human has a large impact on the measured response; by moving the hand close to the antenna during the measurements, the VNA response can be altered. To summarise, the measured antenna impedance is in general in very good agreement with the simulated antenna impedance. For comparison, the antenna impedance and tag transmission coefficient are measured with corresponding measurement accuracy in [19, 49] as in this work.

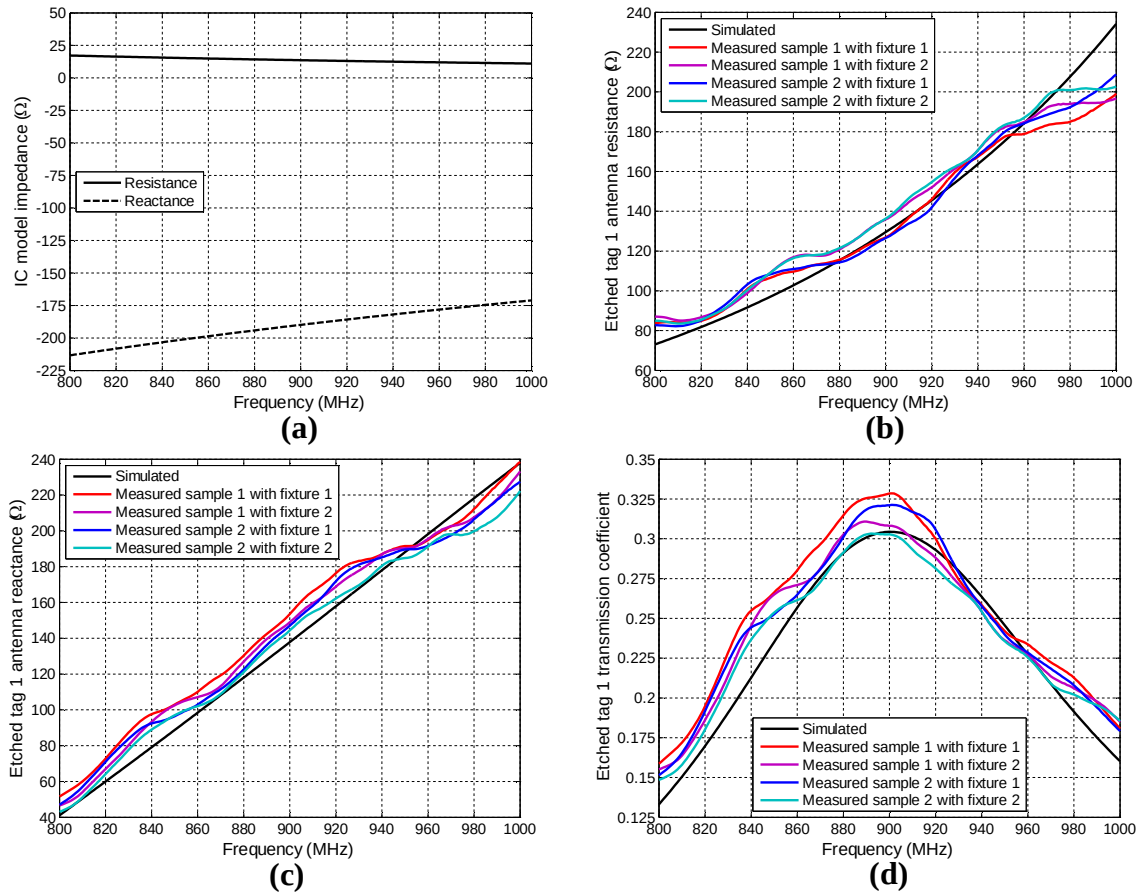

FIG. 4.5 (a) Simulated impedance of the IC model, **(b)** simulated and measured etched tag 1 antenna resistance, and **(c)** reactance. **(d)** Calculated etched tag 1 transmission coefficient from the results presented in (a)–(c). The simulated and measured results agree well. The transmission coefficient results are use to determine the radiation efficiency of the tag antenna.

The results for etched tag 1 samples are shown in Table 4.1. To evaluate the applicably of the directivity approximation, the directivity is approximated from the simulated power patterns. The estimated radiation efficiency is obtained using the approximated directivity in (3.17). All radiation efficiencies are calculated using (3.14).

TABLE. 4.1 Simulation and measurement results for etched tag 1.

	Etched tag 1 sample 1			Etched tag 1 sample 2			Unit
Quantity	840	890	960	840	890	960	MHz
Simulated							
Realised gain	-4.4785	-2.9823	-4.1729	-4.4785	-2.9823	-4.1729	dBi
Directivity	1.6780	1.6741	1.6856	1.6780	1.6741	1.6856	–
H-plane half power beamwidth	2π	2π	2π	2π	2π	2π	rad
E-plane half power beamwidth	1.3538	1.3254	1.2842	1.3538	1.3254	1.2842	rad
Directivity, approximated	1.6158	1.6330	1.6590	1.6158	1.6330	1.6590	–
Transmission coefficient	0.2127	0.3009	0.2271	0.2127	0.3009	0.2271	–
Radiation efficiency	99.89	99.92	99.95	99.89	99.92	99.95	%
Radiation efficiency, estimated	103.75	102.41	101.54	103.75	102.41	101.54	%
Measured							
Realised gain	-4.3200	-2.9010	-3.5860	-4.4390	-2.7960	-3.1870	dBi
H-plane half power beamwidth	2π	2π	2π	2π	2π	2π	rad
E-plane half power beamwidth	1.3685	1.3792	1.3033	1.3805	1.3828	1.2872	rad
Directivity, approximated	1.6071	1.6008	1.6468	1.6000	1.5987	1.6571	–
Transmission coefficient							
Fixture 1	0.2548	0.3255	0.2336	0.2443	0.3184	0.2284	–
Fixture 2	0.2453	0.3108	0.2270	0.2366	0.3027	0.2255	–
Radiation efficiency, estimated							
Fixture 1	90.31	98.40	113.84	92.06	103.20	126.84	%
Fixture 2	93.81	103.06	117.15	95.05	108.55	128.47	%

The radiation efficiency is calculated using (3.14), which assumes that the maximum realised gain and directivity measured over all angles in space are applied. The absolute accuracy of the Tagformance Lite output power is ± 1 dB [37], indicating that the Tagformance measurements are very accurate. In practise, the alignment errors of the tag and the reader in the Tagformance cabinet contribute to measurement uncertainty of the maximum realised gain. In addition, the alignment errors result in that the measured principal planes differ from the simulated ones. The good agreement between the directly simulated directivity and the approximated directivity from simulation results suggests that the directivity approximation is applicable. The approximated directivities based on the measurement results show in addition good agreement the directly simulated directivity.

The measurement of transmission coefficient is most prone to errors due to the limited accuracy of the measured antenna impedance. As mentioned earlier, the non-perfect VNA measurement system calibration result in uncertainties in the measured antenna impedance. However, the radiation efficiency measurement results for the two different fixtures are almost the same, leading to the conclusion that the fixture can successfully be eliminated from the VNA measurement set-up and that the measurement method is independent of the fixture.

The radiation efficiency is directly simulated for the tag antenna, while the radiation efficiency measurement method is dependent on the chip model. The measured read range results comprise information about the chip sensitivity and impedance. The simulated and measured results for read range and realised gain are in very good agreement, indicating that the chip model is accurate and does not contribute to major uncertainties.

In general, the measured etched dipole tag antenna radiation efficiencies show acceptable agreement with the radiation efficiency simulation results. In summary, the measurement results gathered in Table 4.1 support the high radiation efficiency performance of the etched tags, and herewith verify that the radiation efficiency measurement method is applicable for balanced passive UHF RFID dipole tag antennas.

4.1.2 Etched tag 2 design

The results for the etched tag 2 design are presented in this section. The simulated results for radiation efficiency and directivity are presented in Fig. 4.6. The radiation efficiency is simulated to 56–68% within the considered frequency band of 840–960 MHz. The directivity is simulated to approximately 1.5–1.4.

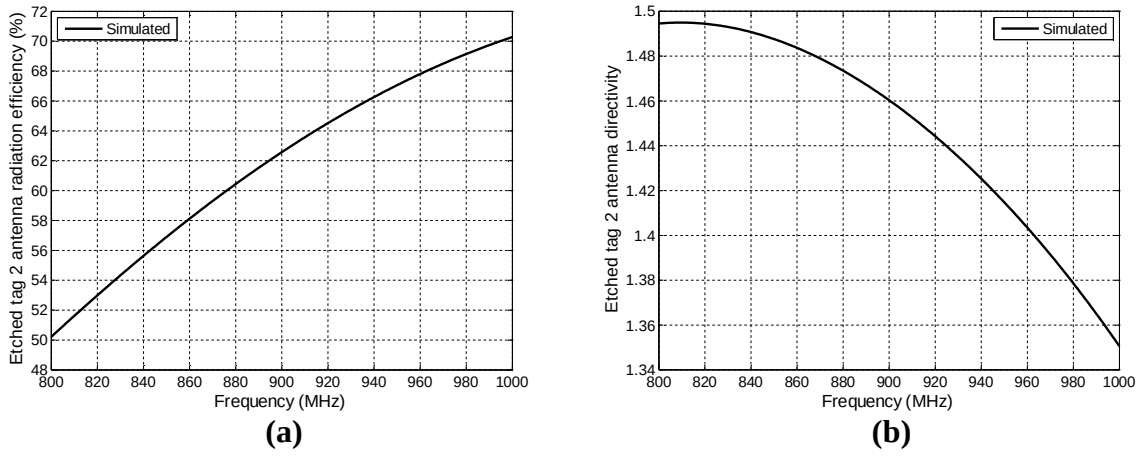

FIG. 4.6 Simulated **(a)** radiation efficiency and **(b)** directivity of etched tag 2 antenna. The antenna is optimised for moderate radiation efficiency.

The measured and simulated results for realised gain and range are shown in Fig. 4.7. The tag samples have poor read range performance due to the influence of the metal plate. A frequency shift of 10 MHz is encountered between the sample performances.

The shift is due to the fabrication and assembling of the tag samples. Etched tag design 2 is significantly more complex that etched tag 1 design and small differences in etched tag 2 geometry or in chip attachment easily shift the tag operations on the frequency scale. Except from the frequency shift, the two tag samples operate similarly with respect to realised gain and read range performance. The optimum performance frequency with respect to read range is at 850 MHz and at 860 MHz for sample 1 and 2, respectively, and at 865 MHz for the simulated tag. However, the simulations predict a much better realised gain and read range performance than what is achieved in practise. These differences are mainly caused by uncertainties in the chip model [31], the hand-made complex antenna fabrication, and the Tagformance measurement system accuracy including alignment errors of the tag and the reader antenna. The results in Fig 4.7 indicate that etched tag 2 is not applicable for verifying the radiation efficiency measurement method and further that the simulated results cannot considered as the real values. However, the method is verified in section 4.1.1, and it is applied to etched tag 2 in order to extract additional information about the applicability of the radiation efficiency measurement method.

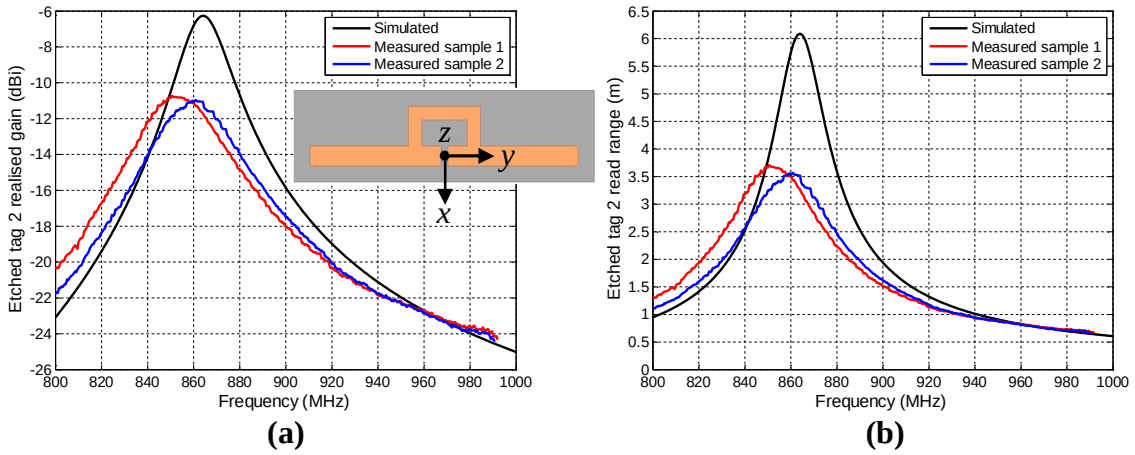

FIG. 4.7 Simulated and measured **(a)** realised gain and **(b)** read range of etched tag 2 samples. The results are recorded from *z* direction. The simulations predict an optimistic tag performance. In addition, the performance of the two tag samples deviate.

The power patterns in Figs. 4.8 and 4.9 are plotted in decibel scale and each pattern is normalised to its own maximum realised gain value. From the simulated patterns is observed that the pattern shape is barely changed at the considered frequency points, which is supported by the almost constant simulated directivity. The simulated patterns are however deviating from the ideal dipole patterns, which is explained by the metal plate. The measured sample 1 and 2 pattern shapes are in good agreement, but the patterns are severely distorted at higher frequencies due to the influence of the metal plate. The simulated and measured -3 dB beam widths are almost the same, resulting in almost equal approximated directivities. The simulated and measured pattern shapes are however deviating significantly from each other, indicating that the directivities cannot be the same in practise even though it is suggested by the directivity approximation. To

judge from the results in Figs. 4.8 and 4.9, one would expect that the realised directivity is greater than the directivity predicted by the simulations.

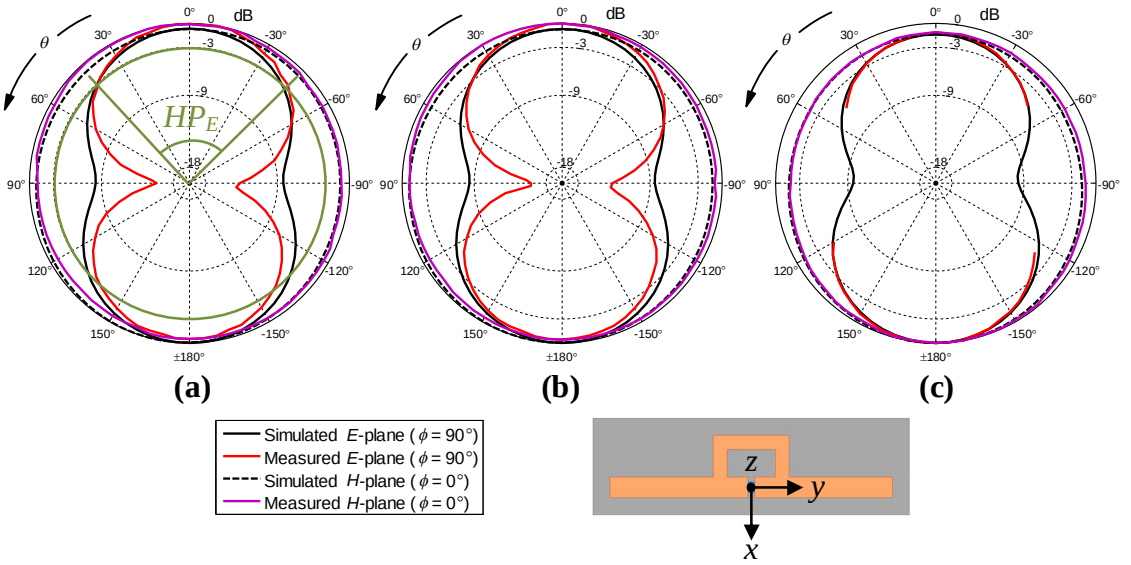

FIG. 4.8 Simulated and measured normalised realised gain for etched tag 2 sample 1 at **(a)** 840 MHz, **(b)** 850 MHz, and **(c)** 960 MHz. The simulated and measured results agree to some extent. The -3 dB *E*-plane beamwidths are used to approximate the tag antenna directivity, as shown in (a).

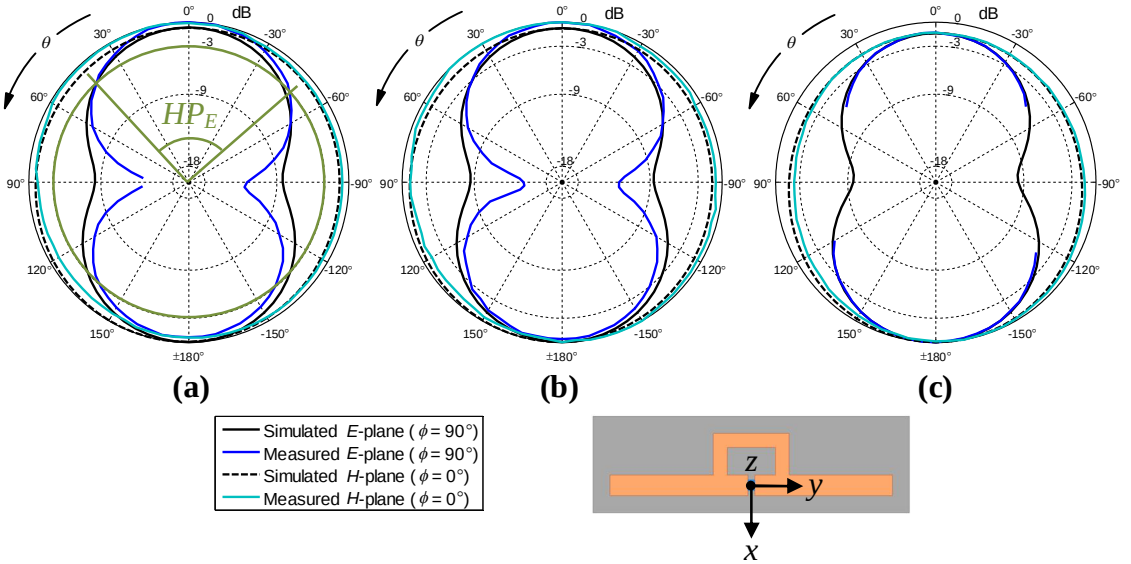

FIG. 4.9 Simulated and measured normalised realised gain for etched tag 2 sample 2 at **(a)** 840 MHz, **(b)** 860 MHz, and **(c)** 960 MHz. The simulated and measured results agree to some extent. The -3 dB *E*-plane beamwidths are used to approximate the tag antenna directivity, as shown in (a).

The impedance measurement and simulation results are presented in Fig. 4.10. The measured antenna resistance and reactance show acceptable agreement with the simulated results. The relatively large fluctuations encountered in the measured resistance curves suggest that non-perfect calibration is obtained, since the fluctuations are appearing in the same manner along the measured curves for both samples when measured with each fixture. In this case, the antenna resistance is very small and the

fluctuations in the measured resistances have a large impact on the calculated transmission coefficient, which explains the relatively large differences between the measured and the simulated transmission coefficient at single frequency points. However, the measured and simulated transmission coefficients are maximised at the same frequency, and all result indicate that poor matching is achieved.

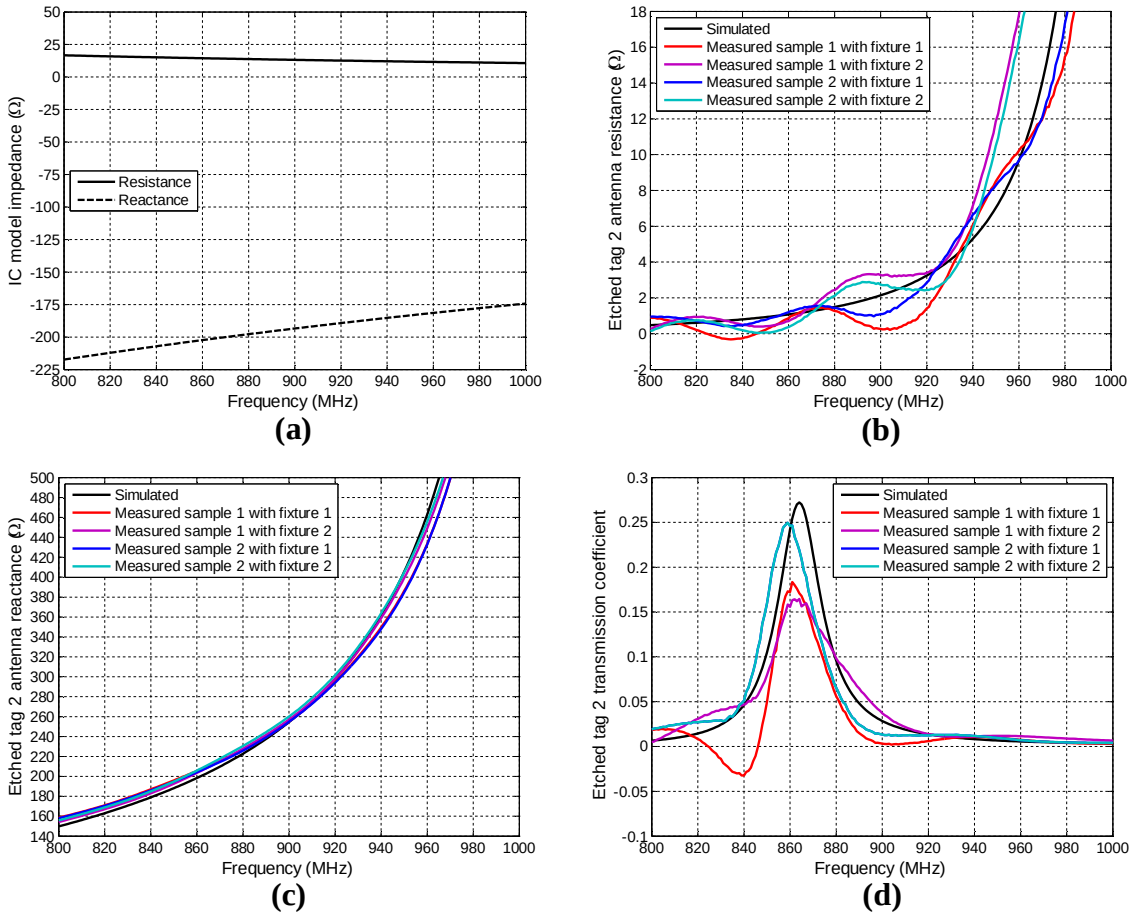

FIG. 4.10 (a) Simulated impedance of the IC model, **(b)** simulated and measured etched tag 2 antenna resistance, and **(c)** reactance. **(d)** Calculated etched tag 2 transmission coefficient from the results presented in (a)–(c). The simulated and measured results agree to some extent. The transmission coefficient results are use to determine the radiation efficiency of the tag antenna.

The results for etched tag 2 samples at the discrete frequency points are gathered in Table 4.2 in the similar manner as for etched tag 1 samples. The estimated radiation efficiency is obtained using the approximated directivity in (3.17). All radiation efficiency results are calculated from (3.14).

The directivity is simulated to 1.4–1.5, which is in agreement with the approximated directivities for the measurement result. However, as discussed above, the large differences between the simulated and measured principal plane power pattern shapes especially at 960 MHz indicate that the directivities of the simulated and measured tag antennas must differ. Hence, it is difficult to conclude whether the directivity approximation is applicable in this case or not.

TABLE. 4.2 Simulation and measurement results for etched tag 2.

	Etched tag 2 sample 1			Etched tag 2 sample 2			Unit
Quantity	840	850	960	840	860	960	MHz
Simulated							
Realised gain	-14.1556	-10.5133	-22.7097	-14.1556	-6.8050	-22.7097	dBi
Directivity	1.4907	1.4876	1.4035	1.4907	1.4837	1.4035	–
H-plane half power beamwidth	2π	2π	2π	2π	2π	2π	rad
E-plane half power beamwidth	1.6723	1.6643	1.5992	1.6723	1.6567	1.5992	rad
Directivity, approximated	1.4538	1.4573	1.4866	1.4538	1.4606	1.4866	–
Transmission coefficient	0.0463	0.1050	0.0056	0.0463	0.2420	0.0056	–
Radiation efficiency	55.63	56.90	67.80	55.63	58.12	67.80	%
Radiation efficiency, estimated	57.06	58.07	64.36	57.06	59.04	64.36	%
Measured							
Realised gain	-12.1860	-10.8400	-22.7010	-14.0560	-11.0900	-22.8350	dBi
H-plane half power beamwidth	2π	2π	2π	2π	2π	2π	rad
E-plane half power beamwidth	1.5547	1.5336	1.5555	1.5770	1.5229	1.5590	rad
Directivity, approximated	1.5078	1.5181	1.5074	1.4971	1.5234	1.5057	–
Transmission coefficient							
Fixture 1	-0.0323	0.0500	0.0075	0.0512	0.2461	0.0071	–
Fixture 2	0.0465	0.0798	0.0115	0.0465	0.1557	0.0115	–
Radiation efficiency, estimated							
Fixture 1	-124.12	108.57	47.49	51.27	20.75	48.70	%
Fixture 2	86.22	68.03	30.97	56.45	32.80	30.07	%

The erroneously negative measured radiation efficiency of etched tag 2 sample 1 at 840 MHz is due to the negatively calculated antenna resistance from the measured *S*-parameters, which result in a negative transmission coefficient. Compared to etched tag 1 results, the measured radiation efficiencies are quite different depending on which fixture is used. This is due to the fact that the encountered relatively large fluctuations in the measure antenna resistance affect significantly the measured transmission coefficient. As can be seen from Table 4.2, the differences in the measured transmission coefficients are relatively large depending on the used fixture. To summarise, the radiation efficiency suggested by the measurement method for etched tag 2 is ambiguous, which is mainly explained by uncertainties in the antenna measurement method. In addition, the measured principal plane power patterns suggest that the used directivity approximation contribute to significant errors.

4.2 Radiation efficiency evaluation of sewed antennas

In this section the radiation efficiency measurement method is utilised to directly measure the radiation efficiency of two sewed tag antenna designs. These antenna structures are challenging to model, and hence the measured radiation efficiency gives valuable information about how the sewed pattern affects the tag antenna losses. The results obtained with the current simulation model for sewed tags are presented together with the measurement results. It should however be noted that the measured radiation is independent of tag antenna simulation results. Also in case of the sewed tags, the NXP chip sensitivity is valid within 840–960 MHz. The radiation efficiency is evaluated and verified at the outer frequency points from this frequency band. The third frequency point is chosen to 900 MHz, which is the centre frequency within the considered frequency band.

4.2.1 Sewed tag 1 design

According to the sewed tag simulation model, the sewed tag 1 design has a radiation efficiency of at maximum 45% and a directivity of 1.5–1.6 within the frequency range of 840–960 MHz, see Fig. 4.11.

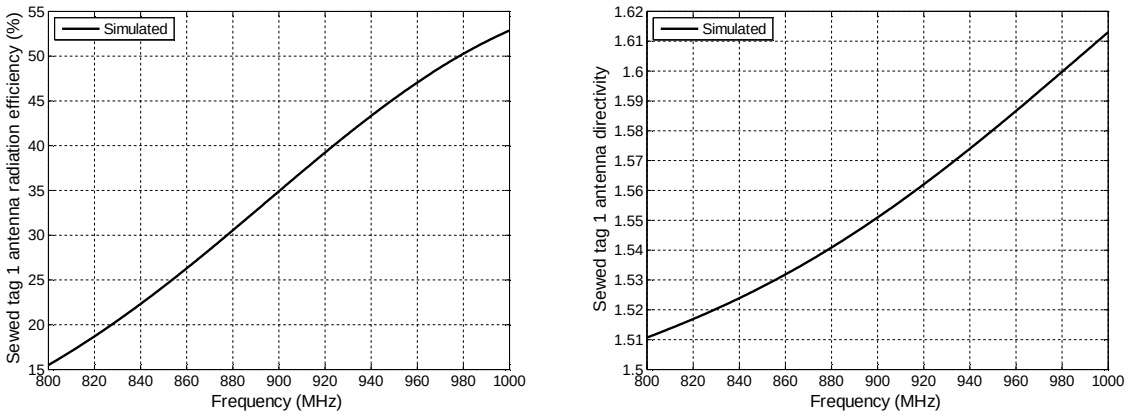

(a) **(b)**

FIG. 4.11 Simulated **(a)** radiation efficiency and **(b)** directivity of sewed tag 1 antenna. The simulations propose moderate tag antenna radiation efficiency.

The measured and simulated results for realised gain and range are shown in Fig. 4.12. The tags have good read range performance, achieving almost a peak read of 7 m. The two tag samples operate in similar manner, and the simulation model predicts with good accuracy the fabricated and the assembled tag measured realised gain and read range. In addition, the measured power patterns are dipole-like and agree with the simulated patterns very well, see Figs. 4.13 and 4.14.

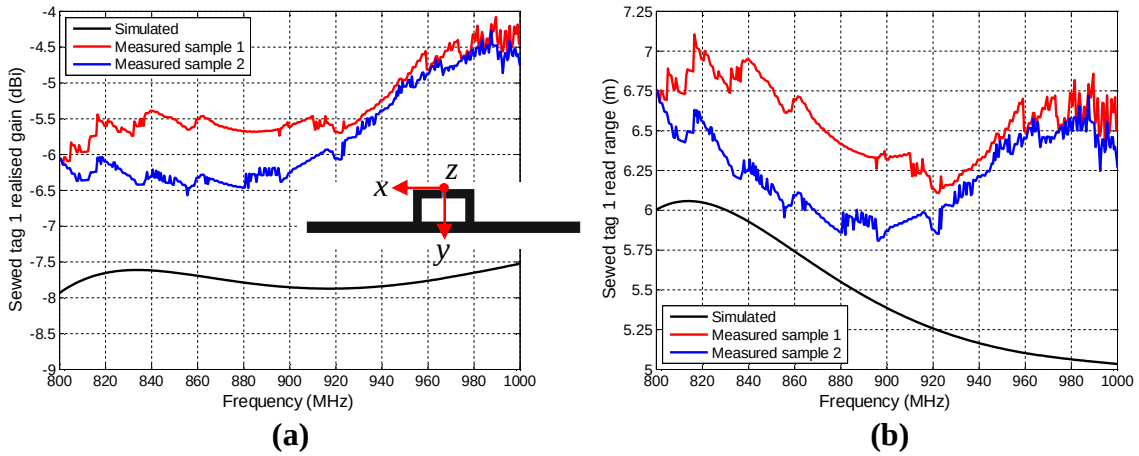

FIG. 4.12 Simulated and measured **(a)** realised gain and **(b)** read range of sewed tag 1 samples. The results are recorded from *z* direction. The fabricated samples show slightly better performance that that proposed by the simulation model. There are only small differences between the two samples.

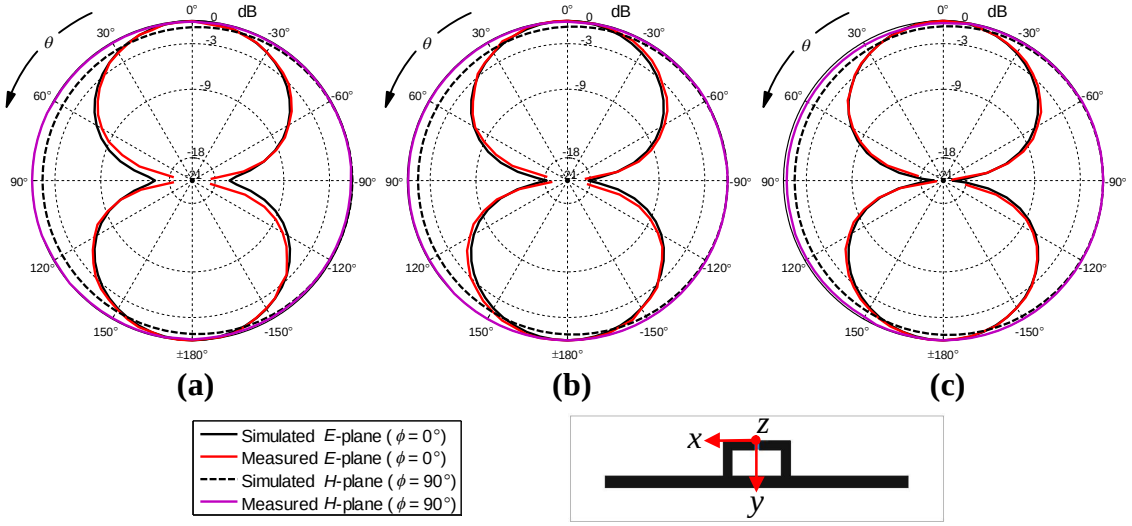

FIG. 4.13 Simulated and measured normalised realised gain for sewed tag 1 sample 1 at **(a)** 840 MHz, **(b)** 900 MHz, and **(c)** 960 MHz. The simulated and measured results agree well.

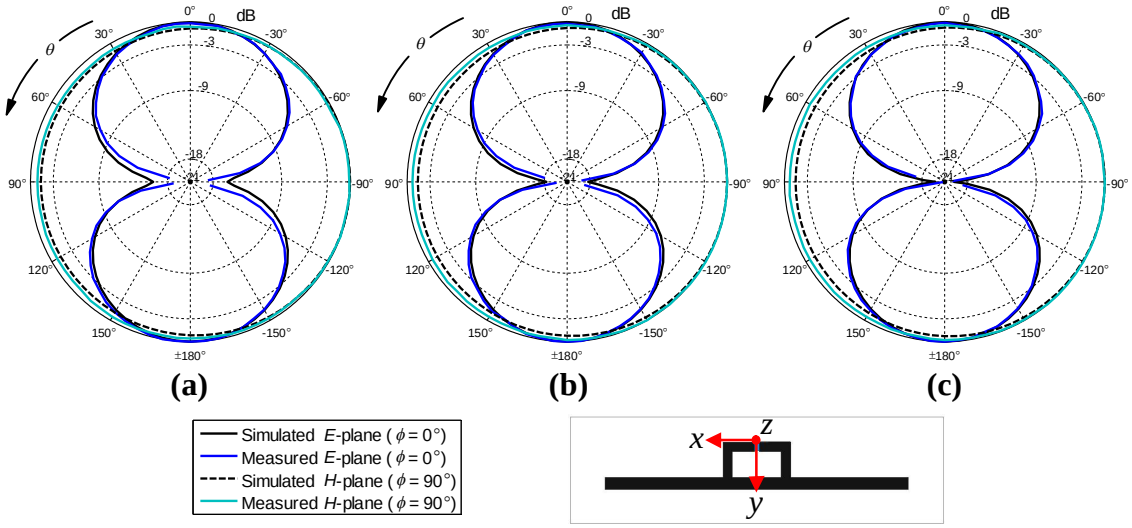

FIG. 4.14 Simulated and measured normalised realised gain for sewed tag 1 sample 2 at **(a)** 840 MHz, **(b)** 900 MHz, and **(c)** 960 MHz. The simulated and measured results agree well.

The impedance measurement and simulated results are presented in Fig. 4.15. The measured antenna impedance deviates significantly from the proposed simulation model. In addition, large differences are encountered between the measurement results for the two different samples. However, the measured impedance is not dependent of the used fixture, and the differences between the impedances of the two antenna samples are hence most probably due to fabrication differences. Moreover, the conductive thread is not easily solderable and when the fixture tips are soldered to the antenna structure. During soldering parts of the threads are slightly burned. The conductive epoxy can furthermore not be cleaned from the threads after the chip has been detached from the antenna. These factors contribute to uncertainties in the measured antenna impedance. However, the two sewed samples show similar frequency behaviour, indicating that measured impedances are reliable to some extent.

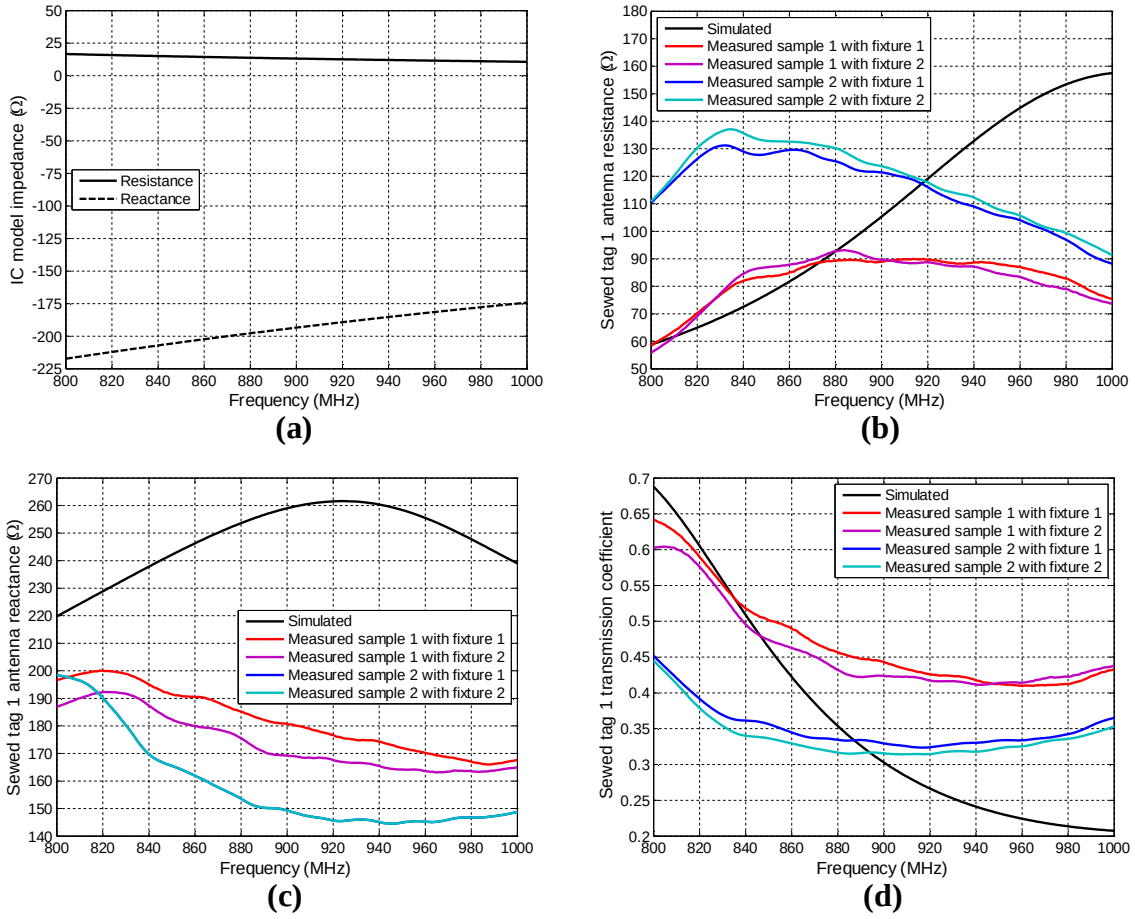

FIG. 4.15 (a) Simulated impedance of the IC model, **(b)** simulated and measured sewed tag 1 antenna resistance, and **(c)** reactance. **(d)** Calculated sewed tag 1 transmission coefficient from the results presented in (a)–(c). There are significant differences between the measured and simulated values. The transmission coefficient results are use to determine the radiation efficiency of the tag antenna.

The measured transmission coefficients are better than predicted by the simulation model, and the measured results suggest that the matching is barely changed over the frequency range of 840–960 MHz. Furthermore, the results in Fig. 4.12 show that the

realised gain is also rather constant, resulting in that the sewed tag antenna gain remains constant over the considered frequency range. In addition, the measured power pattern shapes are barely changed in Figs. 4.13 and 4.14. As the radiation efficiency is defined as the ratio of antenna gain to antenna directivity, and both these quantities are measured to be constant over the considered frequency range, the measured radiation efficiency remain rather constant independent of the frequency. This can be seen from Table 4.3, in which the results for sewed tag 1 samples are gathered.

TABLE. 4.3 Simulation and measurement results for sewed tag 1.

	Sewed tag 1 sample 1			Sewed tag 1 sample 2			Unit
Quantity	840	900	960	840	900	960	MHz
Simulated							
Realised gain	-7.6183	-7.8528	-7.7620	-7.6183	-7.8528	-7.7620	dBi
Directivity	1.5239	1.5509	1.5866	1.5239	1.5509	1.5866	–
H-plane half power beamwidth	2π	2π	2π	2π	2π	2π	rad
E-plane half power beamwidth	1.4607	1.4281	1.3990	1.4607	1.4281	1.3990	rad
Directivity, approximated	1.5555	1.5732	1.5895	1.5555	1.5732	1.5895	–
Transmission coefficient	0.5088	0.3029	0.2243	0.5088	0.3029	0.2243	–
Radiation efficiency	22.32	34.90	47.04	22.32	34.90	47.04	%
Radiation efficiency, estimated	21.87	34.41	46.96	21.87	34.41	46.96	%
Measured							
Realised gain	-5.3900	-5.6120	-4.8190	-6.3090	-6.2540	-4.8710	dBi
H-plane half power beamwidth	2π	2π	2π	2π	2π	2π	rad
E-plane half power beamwidth	1.4693	1.4769	1.4431	1.4578	1.4157	1.4239	rad
Directivity, approximated	1.5510	1.5470	1.5650	1.5571	1.5801	1.5755	–
Transmission coefficient							
Fixture 1	0.5180	0.4430	0.4096	0.3613	0.3295	0.3337	–
Fixture 2	0.4955	0.4238	0.4143	0.3402	0.3156	0.3253	–
Radiation efficiency, estimated							
Fixture 1	35.98	40.08	51.43	41.58	45.51	61.96	%
Fixture 2	37.61	41.89	50.85	44.16	47.51	63.56	%

The radiation efficiency of sewed tag 1 sample 1 and sample 2 are measured to approximately 40–50% and 40–60%, respectively, with use of the proposed radiation efficiency measurement method. The sewed tag 1 is concluded to have moderate radiation efficiency.

4.2.2 Sewed tag 2 design

According to the sewed tag 2 simulation model, the sewed tag antenna 2 design has higher radiation efficiency and directivity than sewed tag 1 antenna design, see Fig 4.16.

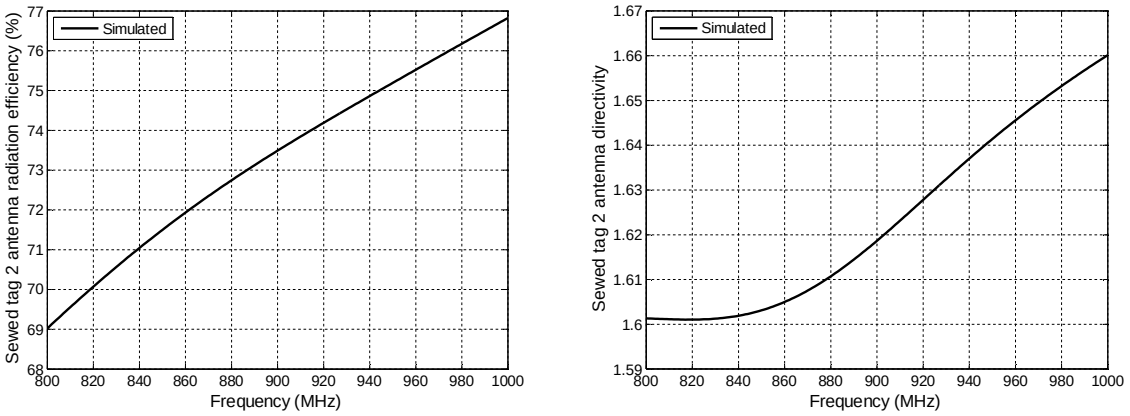

FIG. 4.16 Simulated **(a)** radiation efficiency and **(b)** directivity of sewed tag 2 antenna. The simulations propose good tag antenna radiation efficiency.

The measured and simulated results for realised gain and range are shown in Fig. 4.17. The two tag samples operate in almost identical manner, and the simulation model predicts with good accuracy the fabricated and the assembled tag measured realised gain and read range. In addition, the measured power patterns are dipole-like and agree with the simulated patterns very well, see Figs. 4.17 and 4.18.

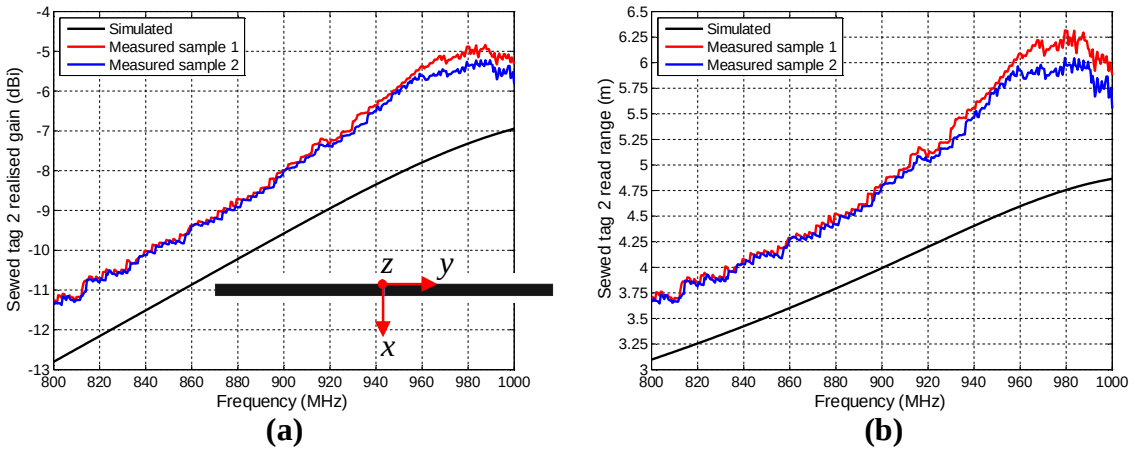

FIG. 4.17 Simulated and measured **(a)** realised gain and **(b)** read range of sewed tag 2 samples. The results are recorded from *z* direction. The simulation model predicts well the tag performance. The two samples have identical performance.

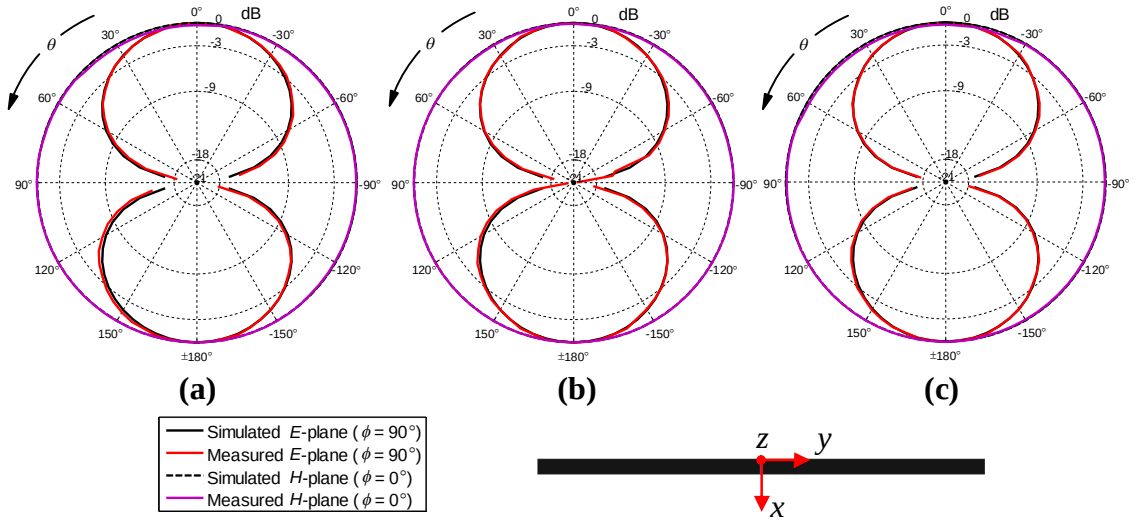

FIG. 4.18 Simulated and measured normalised realised gain for sewed tag 2 sample 1 at **(a)** 840 MHz, **(b)** 900 MHz, and **(c)** 960 MHz. The simulated and measured results agree well.

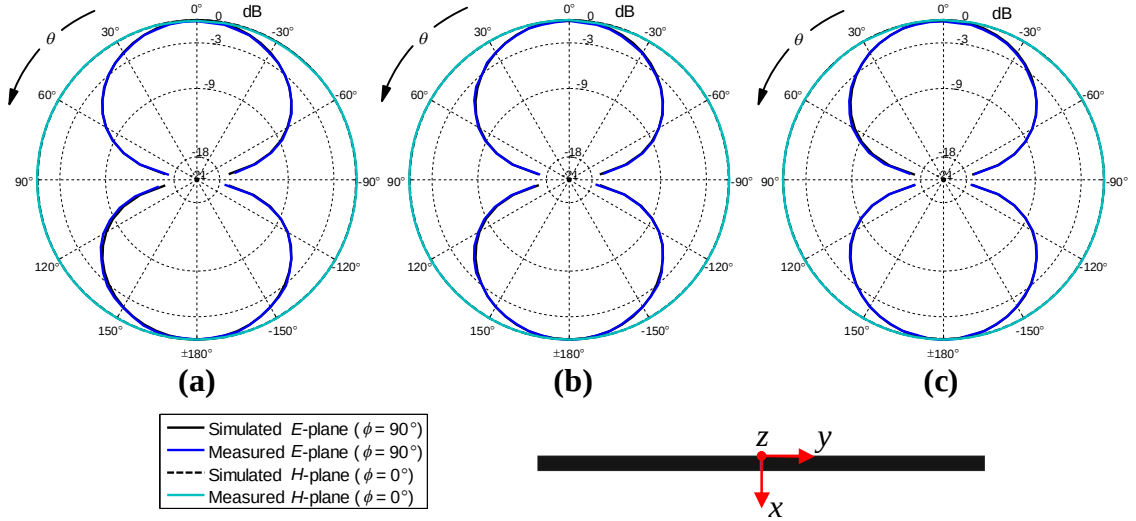

FIG. 4.19 Simulated and measured normalised realised gain for sewed tag 2 sample 2 at **(a)** 840 MHz, **(b)** 900 MHz, and **(c)** 960 MHz. The simulated and measured results agree well.

The impedance measurement and simulation results are presented in Fig. 4.20. The measured antenna impedance deviate from the proposed simulation model, but the same frequency behaviour is observed. Differences are encountered between the measurement results for the two different samples. However, the measured impedance is not dependent of the used fixture, and the differences between the impedances of the two antenna samples are due to fabrication differences, soldering of the fixture to the antenna feed, and most probably due to the presence of the fixture. However, the two sewed samples show similar frequency behaviour, indicating that measured impedances are reliable to some extent.

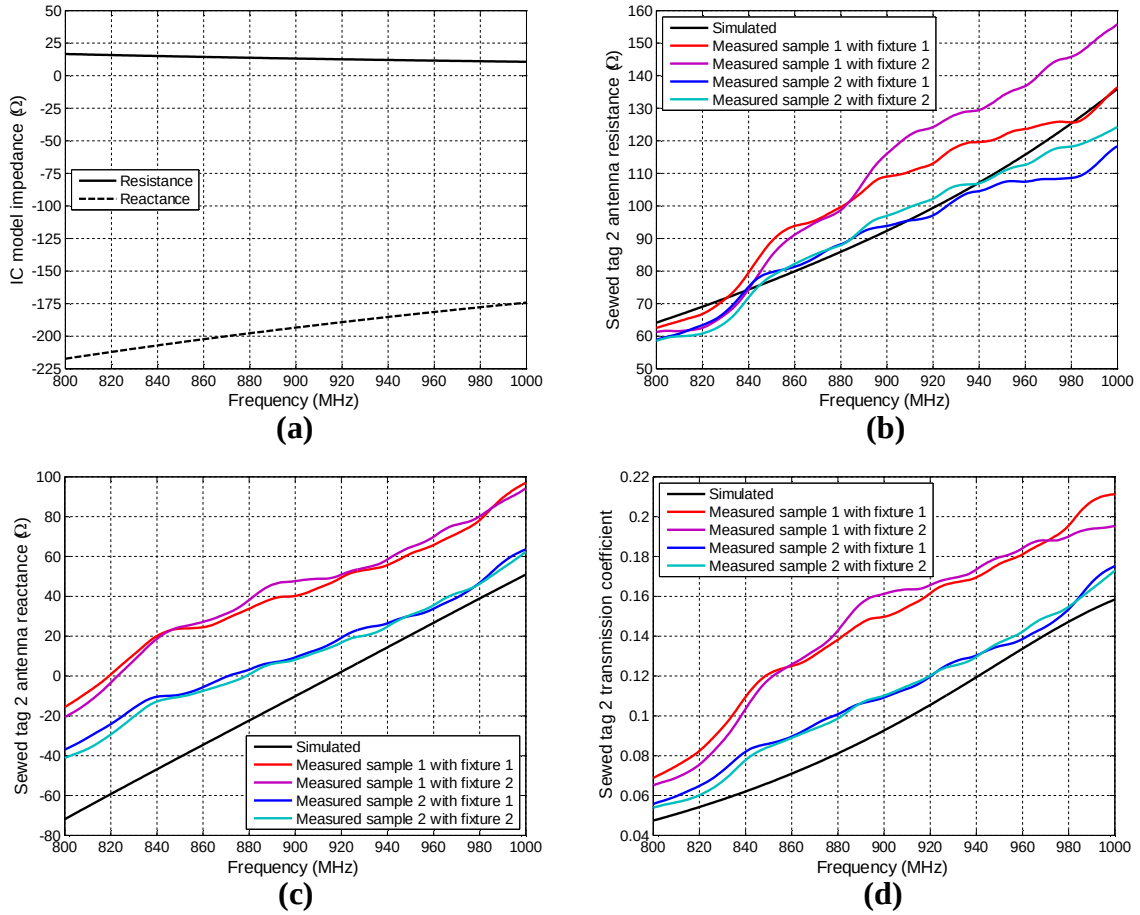

FIG. 4.20 (a) Simulated impedance of the IC model, **(b)** simulated and measured sewed tag 2 antenna resistance, and **(c)** reactance. **(d)** Calculated sewed tag 2 transmission coefficient from the results presented in (a)–(c). There are notable differences between the measured and simulated values. The transmission coefficient results are use to determine the radiation efficiency of the tag antenna.

The results for sewed tag 2 design are gathered in Table 4.4. Comparing tables 4.3 and 4.4, it can be concluded that sewed tag 2 has higher radiation efficiency than sewed tag 1. According to [6], the direction of current flow has to be considered in the whole antenna structure, and a sewing pattern having conductive threads along the current direction has to be chosen in the design of embroidered antennas. The sewed tag 2 is horizontally sewed, which promotes the current flow in the straight dipole antenna design. Sewed tag 1 is sewed vertically, and the thread direction is perpendicular to the current flow. This could be one explanation to why the losses introduced by the sewed tag 1 antenna pattern are higher than for sewed tag 2 antenna pattern. Moreover, sewed tag 2 has a more dense stitch pattern than sewed tag 1, which could also help in lowering the antenna structure losses.

TABLE. 4.4 Simulation and measurement results for sewed tag 2.

	Sewed tag 2 sample 1			Sewed tag 2 sample 2			Unit
Quantity	840	900	960	840	900	960	MHz
Simulated							
Realised gain	-11.5121	-9.5780	-7.7950	-11.5121	-9.5780	-7.7950	dBi
Directivity	1.6019	1.6187	1.6456	1.6019	1.6187	1.6456	–
H-plane half power beamwidth	2π	2π	2π	2π	2π	2π	rad
E-plane half power beamwidth	1.3966	1.3754	1.3529	1.3966	1.3754	1.3529	rad
Directivity, approximated	1.5908	1.6032	1.6163	1.5908	1.6032	1.6163	–
Transmission coefficient	0.0620	0.0926	0.1337	0.0620	0.0926	0.1337	–
Radiation efficiency	71.04	73.49	75.52	71.04	73.49	75.52	%
Radiation efficiency, estimated	71.58	74.23	76.89	71.58	74.23	76.89	%
Measured							
Realised gain	-10.0180	-7.9870	-5.3780	-10.1180	-7.9960	-5.6160	dBi
H-plane half power beamwidth	2π	2π	2π	2π	2π	2π	rad
E-plane half power beamwidth	1.4147	1.4051	1.3479	1.3984	1.3592	1.3445	rad
Directivity, approximated	1.5793	1.5860	1.6193	1.5898	1.6126	1.6214	–
Transmission coefficient							
Fixture 1	0.1095	0.1496	0.1810	0.0820	0.1092	0.1386	–
Fixture 2	0.1035	0.1613	0.1841	0.0778	0.1101	0.1423	–
Radiation efficiency, estimated							
Fixture 1	57.59	66.70	99.00	74.65	90.08	122.11	%
Fixture 2	60.92	62.14	97.23	78.68	89.35	118.93	%

The radiation efficiency of sewed tag 2 sample 1 and sample 2 are measured to approximately 60–100% and 80–100%, respectively, with use of the proposed radiation efficiency measurement method. The sewed tag 2 design is concluded to have good radiation efficiency.

5 CONCLUSION

In this work, a novel radiation efficiency measurement method is developed and verified for passive Ultra High Frequency (UHF) Radiofrequency Identification (RFID) tag antennas. As the dipole antenna is widely used in RFID tag antenna design, the method is developed for antennas of dipole type. The measurement method is applicable for both balanced and unbalanced dipole antennas, and for symmetrical or asymmetrical antenna designs. The tag performance is the key factor affecting the quality of the passive RFID system. The chip sensitivity, the matching of the tag antenna and the chip impedances, and the antenna structure losses are main factors contributing to the tag quality. The proposed radiation efficiency measurement method provides an important mean for characterising complex tag antenna structure losses in free space independently of simulation models. Furthermore, the radiation efficiency measurement method is potentially developable for measurements of the tag antenna in its application environment and for different types of tag antennas. Compared to the existent Wheeler cap radiation efficiency measurement method, the presented measurement method does not require the use of a shielded cap. This is a major advantage when considering the measurement of radiation efficiency in the tag antenna specific application environment. In such cases impractically large caps may have to be fabricated.

The measurement method is based on that the radiation efficiency is calculated from measurements of three quantities: the tag realised gain, the tag antenna directivity, and the tag power transmission coefficient. The tag realised gain and principal plane power patterns are measurable with accurate UHF RFID measurement equipment. Due to the difficulty of measuring the tag antenna directivity, this quantity is approximated from the half-power beamwidths in the two principal plane power patterns. The chip differential impedance and sensitivity are determined and verified in previous research work, and the scattering parameter (*S*-parameter) method in applied to measure the antenna differential impedance. The power transmission coefficient is calculated based on the measured chip and antenna impedances. A vector network analyser (VNA) and a fixture are required for the antenna impedance measurement.

As all the measurement techniques, also the proposed measurement method has drawbacks, restrictions, and assumptions. The tag realised gain and power patterns are measurable with good accuracy as long as the tag is measured in the far-field. Therefore, the directivity approximation is the major factor contributing to uncertainties associated with the measurements conducted with the UHF RFID measurement equipment. The directivity approximation is applicable with good accuracy for antennas whose radiation pattern resembles the ideal dipole pattern shape. If the radiation pattern

is severely distorted, the directivity approximation developed for ideal dipole antennas contribute to unexpected uncertainties and the obtained radiation efficiency measurement results should be considered with caution. The measurement method requires measurement of the tag maximum realised gain and the approximation requires exact information about the principal plane radiation patterns. The alignment errors of the tag and the reader result in that the measured quantities are measured from slightly erroneous angles and hence the alignment errors contribute to measurement uncertainties. Moreover, the output power of the UHF RFID measurement equipment has finite accuracy, which also affects the measurement accuracy. The chip sensitivity is needed to calculate the tag realised gain. Hence, uncertainties in chip sensitivity contribute to errors in the final radiation efficiency.

The power transmission coefficient obtained from the measured antenna and the IC impedances is most prone to errors. Even though the chip impedance is measured and verified in previous research work, it inevitably contributes to uncertainties in the measured power transmission coefficient. However, previous work indicates that the chip model is accurate. The major factor affecting the measured power transmission coefficient accuracy is the antenna impedance measurement. Non-perfect measurement system calibration, the presence of the fixture, and the effects of the soldering process contribute to measurement uncertainties. Particularly, the port extensions involved in the calibration procedure are prone to uncertainties. In general, the antenna inductance is rather high for matching purposes to the highly capacitive chip impedance. Hence the fluctuations encountered in the measured reactance due to non-perfect calibration are relatively small, indicating that the reactance is not significantly affected by small calibration imperfections. However, the antenna resistance tend to be rather low, in order of few ohms, in order to match to the chip resistance. In this case the fluctuations become relatively large and contribute to significant errors in the measured antenna resistance. Moreover, it is crucial for the antenna impedance measurement that the fixture tips can properly be soldered to the antenna structure.

It is difficult to determine experimentally the accuracy of the radiation efficiency method, particularly in an absolute sense. This is part due to the difficulty encountered in separating the errors that arise from the directivity approximation from those associated with the accuracy of the experimental technique. Errors contributed by the directivity approximation cannot be removed by making more accurate measurements. Despite that the encountered measurement uncertainties and errors limit the measurement accuracy, reasonable accuracy is achieved and the proposed radiation efficiency measurement method provides valuable information about tag structure losses. This way, losses introduced by antenna structure can be separated from those originating from mismatches between the tag antenna and the chip impedances. New antenna material structures require proper modelling before they can efficiently be used in antenna design and optimisation. The measurement of radiation efficiency is an important step in the characterisation of complex tag antenna material structures, which augment the future development of new and powerful tag antenna structure solutions.

REFERENCES

[1] AIM, Association for Automatic Identification and Mobility, AIDC Technology. http://www.aimglobal.org/technologies/whatisaidc.asp. Accessed 6 September 2012.

[2] D. M. Dobkin, “The RF in RFID, Passive UHF RFID in Practise.” Elsevier Inc., United States of America, 2008.

[3] E. Koski, K. Koski, T. Björninen, A. A. Babar, L. Sydänheimo, and L. Ukkonen, “Fabrication of Embroidered UHF RFID Tags,” IEEE International Symposium on Antennas and Propagation, 2 p., 8–14 July 2012, Chicago, United States of America.

[4] K. Koski, E. Koski, T. Björninen, A. A. Babar, L. Ukkonen , and L. Sydänheimo, “Practical Read Range Evaluation of Wearable Embroidered UHF RFID Tag,” IEEE International Symposium on Antennas and Propagation, 2 p., 8–14 July 2012, Chicago, United States of America.

[5] E. Moradi, T. Björninen, L. Ukkonen, and Y. Rahmat-Samii, “Characterization of Embroidered Dipole-Type RFID Tag Antennas,” IEEE International Conference on RFID-Technology and Applications, 6 p., 5–7 November 2012, Nice, France.

[6] E. Moradi, T. Björninen, L. Ukkonen, and Y. Rahmat-Samii, “Effect of Sewing Pattern on the Performance of Embroidered Dipole-Type RFID Tag Antennas,” IEEE Antennas and Wireless Propagation Letters. Submitted.

[7] D. M. Pozar, “Microwave Engineering,” 3rd ed. John Wiley & Sons Inc., United States of America, 2005.

[8] W. L. Stutzman and G. A. Thiele, “Antenna Theory and Design,” 2nd ed. John Wiley & Sons Inc., United States of America, 1998.

[9] D. K. Cheng, “Field and Wave Electromagnetics,” 2nd ed. Addison-Wesley Publishing Company, Inc., United States of America, 1992.

[10] C. A. Balanis, “Antenna Theory, Analysis and Design,” 3rd ed. John Wiley & Sons Inc., United States of America, 2005.

[11] K. Finkenzeller, “RFID Handbook, Fundamentals and Applications in Contactless Smart Cards and Identification,” 2nd ed. John Wiley & Sons Inc., England, 2003.

[12] P. Pursula, “Analysis and Design of UHF and Millimetre Wave Radio Frequency Identification,” Dissertation Thesis, VTT Publications 701, Espoo 2008. http://www.vtt.fi/inf/pdf/publications/2008/P701.pdf. Accessed 6 September 2012.

[13] P. V. Nikitin and K. V. S. Rao, “Theory and Measurement of Backscattering from RFID Tags,” IEEE Antenna and Propagation Magazine, vol. 48, no. 6, pp. 212–218, December 2006.

[14] K. Koski, E. Koski, J. Virtanen, T. Björninen, L. Sydänheimo, L. Ukkonen, and A. Z. Elsherbeni, “Inkjet-Printed Passive UHF RFID Tags: Review and Performance Evaluation,” The International Journal of Advanced Manufacturing Technology, vol. 62, no. 1, pp. 167–182, August 2012.

[15] H. Stockman, “Communication by Means of Reflected Power,” Proceedings of the Institute of Radio Engineers, vol. 36, no. 10, pp. 1196–1204, October 1948.

[16] EPCTM Radio-Frequency Identity Protocols Class-1 Generation-2 UHF RFID Protocol for Communications at 860 MHz – 960 MHz, Version 1.1.0, December 2005. http://www.gs1.org/gsmp/kc/epcglobal/uhfc1g2/uhfc1g2_1_1_0-standard-20071017.pdf. Accessed 6 September 2012.

[17] L. Ukkonen, and L. Sydänheimo, “Threshold Power-Based Radiation Pattern Measurement of Passive UHF RFID Tags,” PIERS Online, vol. 6, no. 6, pp. 523–526, 2010.

[18] C. Occhiuzzi, S. Cippitelli, and G. Marrocco, “Modelling, Design and Experimental of Wearable RFID Sensor Tag,” IEEE Transactions on Antennas and Propagation, vol. 58, no. 8, pp. 2490–2498, August 2010.

[19] G. Marocco, “RFID Antennas for the UHF Remote Monitoring of Human Subjects,” IEEE Transactions on Antennas and Propagation, vol. 55, no. 6, pp. 1862–1870, June 2007.

[20] T. Kellomäki, and L. Ukkonen, “Design Approaches for Bodyworn RFID Tags,” 3rd International Symposium on Applied Science in Biomedical Communication, pp. 1–5, 7–10 November 2010, Rome, Italy. U

[21] L. Zhang, Z. Wang, D. Psychoudakis, and J. L. Volakis, “E-Fiber Electronics for Body-Worn Devices,” 6th European Conference on Antennas and Propagation, pp. 760–761, 26–30 March 2012, Prague, Czech Republic.

[22] Y. Bayram, Z. Yijun, S. S. Bong, X. Shimei, Z. Jian, N. A. Kotov, and J. L. Volakis, “E-Textile Conductors and Polymer Composites for Conformal Lightweight Antennas,” IEEE Transactions on Antennas and Propagation, vol. 58, no. 8, pp. 2732–2736, August 2010.

[23] J. Virtanen, T. Björninen, L. Ukkonen, and L. Sydänheimo, “Passive UHF Inkjet-Printed Narrow-Line RFID Tags,” IEEE Antennas and Wireless Propagation Letters, vol. 9, pp. 440–443, May 2010.

[24] E. Koski, K. Koski, L. Ukkonen, L. Sydänheimo, J. Virtanen, T. Björninen, and A. Z. Elsherbeni, “Performance of Inkjet-Printed Narrow-Line Passive UHF RFID Tags on Different Objects,” IEEE International Symposium on Antennas and Propagation, pp. 537–540, 3–8 July 2011, Spokane, Washington, USA.

[25] J. Zhang, S. Pivnenko, and O. Breinbjerg, “A Modified Wheeler Cap Method for Radiation Measurement of Balanced Electrically Small Antennas,” Proceedings of the Fourth European Conference on Antennas and Propagation, pp. 1−5, 12−16 April 2010, Barcelona, Spain.

[26] G. S. Smith, “An Analysis on the Wheeler Method for Measuring the Radiating Efficiency of Antennas,” IEEE Transactions on Antennas and Propagation, vol. 25, no. 4, pp. 552–556, July 1977.

[27] E. H. Newman, P. Bohley, and C. H. Walter, “Two Methods for the Measurement of Antenna Efficiency,” IEEE Transaction on Antennas and Propagation, vol. 23, no. 4, pp. 457–461, July 1975.

[28] H. A. Wheeler, “The Radiansphere Around a Small Antenna,” Proceedings of the Institute of Radio Engineers, vol. 47, no. 8, pp. 1325–1331, August 1959.

[29] R. H. Johnston, and J. G. McRory, “An Improved Small Antenna Radiation Efficiency Measurement Method,” IEEE Antennas and Propagation Magazine, vol. 40, no. 5, pp. 40–48, October 1998.

[30] C. Mendes, and C. Peixeiro, “Theoretical and Experimental Validation of a Generalized Wheeler Cap Method,” The Second European Conference on Antennas and Propagation, pp. 1–6, 11–16 November 2007, Edinburgh, United Kingdom.

[31] T. Björninen, L. Sydänheimo, and L. Ukkonen, “Development and Validation of an Equivalent Circuit Model for UHF RFID IC Based on Wireless Tag Measurements,” Proceedings of the Antenna Measurements Techniques Association Symposium, 6 p., 21–26 October 2012, Bellevue, Washington, USA.

[32] NXP Semiconductor, SL3S1203AC0 Product Data Sheet. http://www.nxp.com/documents/data_sheet/SL3S1203_1213.pdf. Accessed 29 May 2012.

[33] P. V. Nikitin, K. V. S. Rao, R. Martinez, and S. F. Lam, ”Sensitivity and Impedance Measurements of UHF RFID Chips”, IEEE Transactions on Microwave Theory and Techniques, vol. 57, no. 5, pp. 1297–1302, May 2009.

[34] G. Marocco, “The Art of UHF RFID Antenna Design: Impedance-Matching and Size-Reduction Techniques,” IEEE Antennas and Propagation Magazine, vol. 50, no. 1, pp. 66–79, February 2008.

[35] W. L. Stutzman, “Estimating Directivity and Gain of Antennas,” IEEE Antennas and Propagation Magazine, vol. 40, no. 4, pp. 7–11, August 1998.

[36] Voyantic Ltd., Tagformance Lite Product Overview. http://www.voyantic.com/. Accessed 29 May 2012.

[37] Tagformance Lite Measurement System, User Guide, Rev 3.8.x, 2011. http://voyantic.com/Tagformance%20Manual.pdf. Accessed 7 September 2012.

[38] P. Vizmuller, “RF Design Guide, Systems, Circuits, and Equations.” Artech House Inc., United States of America, 1995.

[39] L. Konstroffer, “Finding the Reflection Coefficient of a Differential One-Port Device,” Defence Electronics, RF Semiconductor, January 1999. http://www.rfdh.com/ez/system/db/lib_jnl/upload/3013/%5BRFD9901%5D_Finding_the_reflection_coefficient_of_a_differential_one-port_device.pdf. Accessed 7 September 2012.

[40] H. Zhu, Y. C. A. Ko, and T. T. Ye, “Impedance Measurement for Balanced UHF RFID Tag Antennas,” IEEE Radio and Wireless Symposium, pp. 128–131, 10–14 January 2010, New Orleans, Louisiana, USA.

[41] A. Ghiotto, T. P. Vuong, and K. Wu, “Chip and Antenna Impedance Measurement for the Design of Passive UHF RFID Tag,” IEEE Proceedings of the 40th European Microwave Conference, pp. 1086–1089, 28–30 September 2010, Paris, France.

[42] X. Qing, C. K. Goh, and Z. N. Chen, “Measurement of UHF RFID Tag Antenna Impedance,” IEEE International Workshop on Antenna Technology, pp. 1–4, 2–4 March 2009, Santa Monica, California, USA.

[43] X. Qing, C. K. Goh, and Z. N. Chen, “Impedance Characterization of RFID Tag Antennas and Application in Tag Co-Design,” IEEE Transactions on Microwave Theory and Techniques, vol. 57, no. 5, pp. 1268–1274, May 2009.

[44] Agilent Technologies, In Fixture-Measurement Using Vector Network Analysers, Application Note. http://cp.literature.agilent.com/litweb/pdf/5968-5329E.pdf. Accessed 30 May 2012.

[45] Agilent Technologies, Agilent De-Embedding and Embedding S-parameter Networks Using a Vector Network Analyzer, Application Note 1364-1. http://cp.literature.agilent.com/litweb/pdf/5980-2784EN.pdf. Accessed 30 May 2012.

[46] D. Fei, “The Research of Port Extension and De-Embedding Based on Vector Network Analyzer,” International Conference on Electronic Measurement & Instruments, vol. 2, pp. 344–347, 16–19 August 2011, Chengdu, China.

[47] R. Meys, and F. Janssens, “Measuring the Impedance of Balanced Antennas by an *S*-Parameter Method,” IEEE Antennas and Propagation Magazine, vol. 40, no. 6, pp. 62–65, December 1998.

[48] TE Connectivity, 1-1478903-0 SMA Plug, SMA, Straight, RG402 Datasheet. http://uk.farnell.com/. Accessed 11 June 2012.

[49] M. H. Lin, and C. W. Chiu, “Human-body Effects on the Design of Card-type UHF RFID Tag Antennas,” IEEE International Symposium on Antennas and Propagation Society, pp. 521–524, 3–8 July 2011, Spokane, Washington, USA.